Kavindra R. Jain · N. C. Chauhan

Dental Image Analysis for Disease Diagnosis

Springer

Dental Image Analysis for Disease Diagnosis

Kavindra R. Jain • N. C. Chauhan

Dental Image Analysis for Disease Diagnosis

Springer

Kavindra R. Jain
Department of Electronics
and Communication
G H Patel College of Engineering
and Technology
Anand, Gujarat, India

N. C. Chauhan
Department of Information Technology
A.D. Patel Institute of Technology
Anand, Gujarat, India

ISBN 978-3-030-14135-6 ISBN 978-3-030-14136-3 (eBook)
https://doi.org/10.1007/978-3-030-14136-3

Library of Congress Control Number: 2019934370

This Springer imprint is published by the registered company Springer Nature Switzerland AG
The registered company address is: Gewerbestrasse 11, 6330 Cham, Switzerland

Preface

Image processing has become a critical component in contemporary science and technology. It is an interdisciplinary subject that draws from synergistic developments involving: medical imaging, machine vision, agriculture, food industry, astronomy, computer vision, geology and many other fields.

The rapid progress in computerized medical image reconstruction and associated developments in analysis methods and computer-aided diagnosis have propelled medical imaging into one of the most important subfields in scientific imaging. This book examines medical applications and uses real medical images and situations to clarify and consolidate concepts and to build intuition, insight and understanding. This book gives an overview and the fundamentals for important clinical imaging modalities in use is and provides insight on how the images are produced and acquired.

This book is written for upper level undergraduate or first-year graduate students with a background in biomedical engineering, computer science, radiologic sciences or physics. The material is designed for readers who will become 'end users' of digital image processing in the biomedical sciences, it emphasizes the conceptual framework and the effective use of image processing tools and uses mathematics as a tool, minimizing the advanced mathematical development of other textbooks.

Discussions of the major medical imaging modalities enable students to understand the diagnostic tasks for which images are needed and the typical distortions and artifacts associated with each modality. This knowledge then motivates the presentation of the techniques needed to reverse distortions, minimize artifacts and enhance important features. Students will understand why they are undertaking particular operations, and the practical activities would enable them to see in real time how operations affect real images. Image processing is a hands-on course, and the best way to learn is by doing it. Theory and practice are linked, each reinforcing the other.

I would like to express my sincere gratitude to Shakti Orthopedic, Anand, for providing radiographs of patients with their consent. Throughout the course work of my research, Dr. Ronak Panchal constantly supported me for the research and helped me beyond any doubt in medical field. He introduced me to the field of dentistry with

a distinguished approach for a noble cause. I would be ever indebted for his righteous and ever enthusiastic approach in my research work and his patience, motivation, enthusiasm, immense knowledge and constant support, inculcating within me the productive and result-oriented ideas.

I owe my deepest gratitude to a very special person of my personal life who contributed in making this work possible. Millions of thanks go to my beloved wife Niky for her eternal support, encouragement and love during these years of my research. It's my fortune to gratefully acknowledge her for understanding my goals and aspirations. She was always beside me during the happy and hard moments to push me and motivate me. A journey is easier when you travel together. Interdependence is certainly more valuable than independence. This book is the result of my parents and in-laws who were always there when I really needed them. Thank you doesn't seem sufficient, but it is said that with regards, appreciation and respect to them for their unconditional love and support during my journey of research work, I would be ever indebted to them.

My special words of thanks to the one who always guided me in the inevitable ups and downs by reminding me the true priorities of life. I doubt that I will be ever able to convey my appreciation fully, but I owe him my eternal gratitude. His blessings, constant support and strength helped me a lot to work for hours together tirelessly. Words always fall short when I thank my almighty 'Shree Kashtbhanjan Hanuman Ji' for providing me platform to work upon for the society and my alma matter. Thank you God for showering your blessings on me forever.

Anand, India

Kavindra R. Jain
N. C. Chauhan

Contents

About the Authors

Kavindra R. Jain received a Ph.D. in Electronics and Communication Engineering from RK University, Rajkot, Gujarat, India, in 2018. He has an M.E. degree in Communication Engineering from G H Patel College of Engineering and Technology, Sardar Patel University, Vallabh Vidyanagar, Gujarat, India, in 2009 and B. Tech. degree in Electronics and Instrumentation Engineering from Guru Teg Bahadur Khalsa Institute of Engineering and Technology, Punjab Technical University, Malout, Punjab, India, in 2006. Dr. Jain has published and presented more than 45 research papers in various high-impact factor international journals and various international and national conferences. He is life member of ISTE. His areas of interests are Computer Vision, Data Mining, Medical Imaging and Image Processing.

N. C. Chauhan received a Ph.D. in Electronics and Communication Engineering from IIT Roorkee, Uttar Pradesh, India, in 2010. He has an M.E. degree in Computer Science Engineering from Birla Vishwakarma Mahavidyalaya, Sardar Patel University, Vallabh Vidyanagar, Gujarat, India, in 2005 and B.Tech. degree from the same college in 2001. Dr. Chauhan has published a book on computational microwave and millimetre wave design problems, and has published and presented 48 research papers in various high-impact factor international journals and international and national conferences. He is life member of ISTE and IE and an institutional member of CSI.

Chapter 1
Introduction

1.1 Overview

Medical imaging is an important and growing field of research in the healthcare domain. The advancements of technology in medical imaging are a step towards the effective healthcare and patient friendly gadgets. With the advancement in technologies, the possibilities of early detection of diseases and its precision levels are increasing which provides more time to patients as well as medical practitioners so that better treatment can be availed at an early stage. The pre-diagnostics analytical support of any disease provides the medical practitioners a broader scope to treat the patient in a more precise direction. Digital radiography has been available in dentistry for more than 25 years, and its use by dental practitioners is steadily increasing. In dental practices, postprocessed image of digital dental radiographs is most commonly used [1]. To enhance image quality and increase the accuracy of interpretation digital acquisition of radiographs followed by their computational processing is performed [2]. Using techniques of image processing, dental radiographic images can be easily processed in a desired way, thus helping practitioners in further diagnosis.

Dental radiograph is a type of image displaying teeth structure and their organisation in mouth. Radiographs are formed by electromagnetic radiation, just like visible light. The radiation is of higher energy and can penetrate the body to form an image on film [3]. Structures that are dense (such as silver fillings or metal restoration) will block most of the photons and will appear white on the developed film. Structures containing air will be black on film, while teeth, tissue and fluid will appear as shades of grey. Dental radiographs help to find problems with teeth, mouth and jaw. Dental radiograph pictures can show cavities, hidden dental structures (such as wisdom teeth), and bone loss that cannot be seen during a visual examination. They are very useful in detecting the early stages of decay between teeth [4].

K. R. Jain, N. C. Chauhan, *Dental Image Analysis for Disease Diagnosis*,
https://doi.org/10.1007/978-3-030-14136-3_1

There are four types of radiographs [3]:

- Bitewing
- Periapical
- Palatal (or occlusal)
- Panoramic

The *bitewing* type of radiograph is when the patient bites on a paper tab and shows the crown portions of the top and bottom teeth together as shown in Fig. 1.1a.

The *periapical* type of radiograph shows one or two complete teeth from crown to root as shown in Fig. 1.1b.

Bitewing and the periapical radiographs are important as they are widely used even in small clinics for disease diagnoses. The dentist manipulates the indicator cone behind the teeth in the area where diagnosis is required [5].

The indicator cone is operated from outside with the position and orientation of the film adjusted inside the mouth to get an exact projection. The *bitewing* type of radiograph shows the upper and lower back teeth and how the teeth touch each other

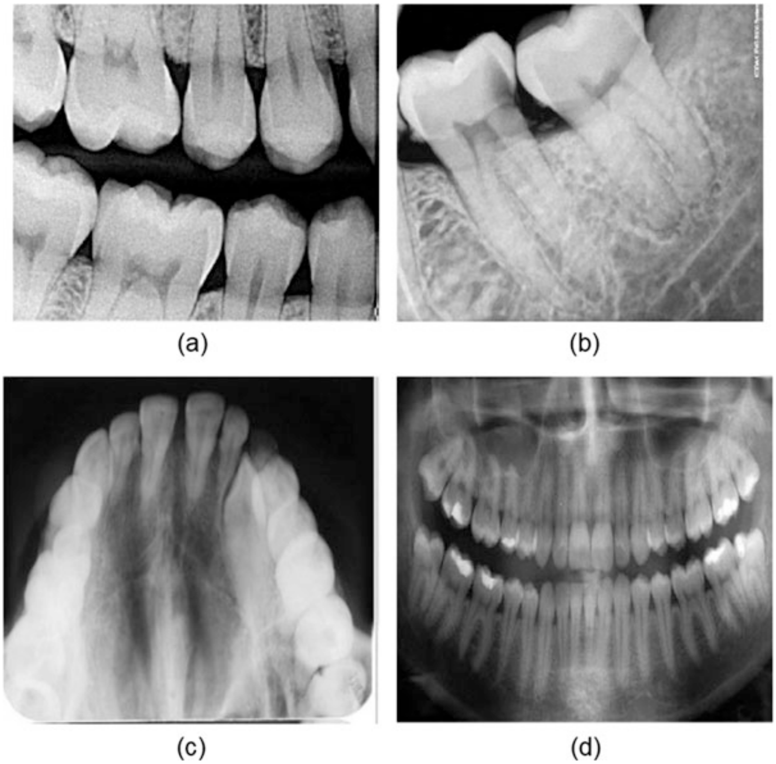

Fig. 1.1 Various types of dental radiographs {Courtesy: Dr Ronak Panchal}. (**a**) Bitewing dental radiograph. (**b**) Periapical dental radiograph. (**c**) Occlusal dental radiograph. (**d**) Panoramic dental radiograph

in a single view [6]. These radiographs are used to check for decay between the teeth and how well the upper and lower teeth line up. They also show bone loss when severe gum disease or a dental infection is present. The planes of the detector and the cone are aligned parallel in bitewing radiographs. This arrangement makes bitewing radiographs give an exact view of the internal structure of the teeth.

The *palatal* (also called occlusal) type of radiograph captures all the upper and lower teeth in one shot while the film rests on the biting surface of the teeth as shown in Fig. 1.1c.

A *panoramic* type of radiograph requires a special machine that rotates around the head. The radiograph captures the entire jaws and teeth in one shot. These radiographs do not help in finding cavities. It is used for dental implants, checking for impacted wisdom teeth, and detecting jaw problems. These radiographs show problems such as *impacted teeth*, *bone abnormalities*, *cysts*, *solid growths (tumours), infections* and *fractures*. With the development of digital imaging technology, digital radiograph machines are becoming popular in dental clinics [7, 8].

Digital dental radiographs have several advantages:

- Compared to traditional radiographs, only half the dosage of radiation is needed for obtaining a dental radiograph of comparable quality.
- Digital dental radiographs do not require time for film development, so dentists need to wait for only a few seconds before the acquired image is displayed.
- Dentists can take another image instantly if the acquired image is not of good quality, so in general digital dental radiographs in a patient's record have better image quality than conventional dental radiographs.
- Digital radiographs are easier to store and process, while conventional radiographs need to be digitised for image processing.
- Digital dental radiographs are environment friendly since they do not generate chemical wastes from film processing.

There are also disadvantages associated with the use of digital systems. The initial cost can be high depending on the system used, the number of detectors purchased, etc. Mastering competency in using the software can take time depending on the level of computer literacy of team members.

1.2 Problem Statement

Any disease of the hard tissues of the teeth caused due to micro-organisms found in plaque is termed as dental caries. Dental caries are broadly classified as enamel, dentinal and pulpal caries.

The first type is the *enamel caries*, which is preceded by the formation of a microbial dental plaque. The second type is *dentinal caries* which starts with the natural spread of dental tubules. The third one is termed as *pulpal caries* that corresponds to the root caries or root surface caries.

Primary diagnosis comprises all visible tooth surfaces using a proper illumination system, a dental mirror and an explorer. Dental radiographs provide a broader look on caries especially between teeth far before it is visible to naked eye. Larger caries can be easily detected and diagnosed, and are apparent to naked eyes, but smaller lesions cannot be easily detected. Precise detection along with visual inspection by practitioners is quite frequently essential in such cases. Caries can move from enamel to dentin, but the exterior surface of a tooth may be site intact. Such caries are termed as hidden caries, and at initial stages radiograph is the only approach to identify them despite the fact that they are minimally perforated [9]. The advent of radiograph in the field of dentistry would help the medical practitioners as well as patients in diagnosis, detection and assessing a condition's effect on other teeth. This could not have been possible with traditional radiographs as patients would respond only at severe stages of pain. *The main aim of this research work is to perform detection/segmentation of dental caries from digital dental radiographs by applying individual and combination of semi-automatic and automatic computationally intelligent methods along with image processing techniques. One of the goals is also to demonstrate the identification of dental caries for a range of dental diseases such as cyst.* The detection of affected caries (region of interest) as an outcome after applying the proposed methods can help practitioners in further diagnosis and treatment.

1.3 Objectives

The sole purpose of this research work is a joint venture of engineering skills and medical background in an area that is of great interest to the medical healthcare community. Computer vision has spread its wings into our daily life in a wide manner, specifically for diagnosis and detection purposes in healthcare. The second reason for showing an interest in this domain of specialisation is that there has already been extensive research for tooth extraction or segmentation for identification purposes in cybercrimes, but unfortunately less work has been done in this area of specialisation when it comes to a joint venture of skills in medical science and engineering background for diagnosis and further treatment of caries. Few objectives which prompted further research in this domain are enlisted below:

- *To study the state of the art in the field of dental image analysis.*
- *To study various preprocessing and postprocessing techniques for analysis of dental radiographs.*
- *To study and implement various image segmentation techniques and use them for identification of various dental caries.*
- *To perform necessary analysis of dental radiographs for the detection of region of interest for dental problems such as cyst, erthyroplakia and leucoplakia.*

- *To have a comparative analysis of methods used for extraction of region of interest.*

This work would be helpful for medical practitioners as an add-on approach for further identification and analysis.

1.4 Suggested Approach

The suggested approach initially was to implement the basic image processing techniques and to select the region of interest for further processing. The selected region of interest would be enhanced and segmented based on the requirement and decision by practitioners. As the research further progressed it was observed and concluded that the process of proper selection in first stage itself is a major task. To address this challenging problem Euler–Lagrange algorithm was selected for segmentation of the given image using active contour modelling. Later, due to weaknesses of this model with respect to the needs of the particular application a model that depicts the structure of true images, in which force inhomogeneity is credited to a part of an image, was designed. Enhancement, segmentation and extraction process were further incorporated in the suggested method for the ease of understanding for patients as well as practitioners. Later on, classification based on clustering technique were applied for decision-making based on disease and further helping practitioners in treating patients. The whole idea is to provide an add-on approach to doctors for early diagnosis and treatment of patients to avoid major surgeries and complications.

1.5 Database Summary

There are a total of 1087 dental and oral mucosa images in the database with various types of dental structure, number of teeth per image and size of mouth. We have collected these database images from two dental practitioners, Dr Ronak Panchal (Anand, Gujarat, India) and Dr Dhrumin Patel (Bharuch, Gujarat, India), for our research work. The detailed summary of the types and size of images per dental diseases is given in Table 1.1. The results of this research are also shared with both the practitioners for the purpose of their authentication in addition to the statistical measures used in the thesis.

A few more database images of periapical dental X-ray are taken from a web lab. A total of 120 images of size 512*748 are obtained from which 61 images are with cavity and 59 without cavity.

Table 1.1 Dataset summary of dental images

Type of dental disease	Number of images	Image type	Image size	Source
Idiopathic resorption	131	RVG	512*512	Dr Ronak Panchal A Dental practitioner Shakti Orthopaedic, Anand, Gujarat
Abscess; Cyst	112			
Dental implants	129			
Endodontic treatment or filling	241			
Impacted third molar	110			
Erythroplakia	177	JPEG	1024*1024	Dr Dhrumin Patel A Dental practitioner A Tooth Clinic, Navsari, Gujarat
Leucoplakia	67			

1.6 Organisation of Book

This book is organised as follows:

Chapter 1 provides an introduction of the overall problem. It comprises joint ventured knowledge of medical science along with engineering background in dentistry. It also highlights the problem statement, detailed objectives of the work, and a brief overview of the suggested approach.

Chapter 2 serves twofold purpose. It provides domain study of dentistry and dental radiographs, as well as state-of-the-art review of the related work in the literature. The initial stage of this chapter includes concepts of tooth, dentistry and their associated research problems. The rest of this chapter summarises the state of art review on image enhancement and segmentation techniques as performed on dental radiographs or radiographs in general. It also provides a review of methods of feature extraction and classification on radiograph images. The chapter is concluded by providing a brief summary of the state-of-the-art review and information about the chosen databases.

Chapter 3 presents the method of tooth enhancement and segmentation from dental radiographs using basic image processing morphological operations. Preprocessing of a dental radiograph and removal of noise from the given image constitute a primary task of this unit. Later on, teeth are segmented and extracted for detection of dental caries using a morphological image processing technique. The results are compared using statistical measures and later presented.

Chapter 4 presents and demonstrates the role of active contour models for segmenting region of interest (ROI) from dental radiographs—the extraction of ROI and its analysis plays a key role in diagnosis and treatment of dental problems. In this module a semi-automatic approach for segmentation and extraction is suggested. Using an active contour model a modified approach is suggested which provides a specified ROI with some assumed parametric conditions.

Chapter 5 presents the use of a novel multiphase level set method for automatic segmentation of dental radiographs—the challenging task is to select an ROI which does not have a false contouring as compared to ground truth. In this module Euler–Lagrange method with multiphase level method is incorporated to identify ROI. The extracted caries are further evaluated using morphometric operations and statistical data so obtained are tabulated.

Chapter 6 presents and demonstrates role of computational clustering techniques for segmentation of teeth and dental caries. This chapter majorly focuses on clustering techniques such as fuzzy C-means, K-means and kernel fuzzy C-means for segmentation and extraction of caries and their further processing.

Chapter 7 concludes the overall work presented in the thesis. It also outlines further directions that can be explored and investigated in this domain.

Chapter 2
Domain Study and Literature Review

2.1 Domain Study

2.1.1 Dental Anatomy and Tooth Structure

Dental anatomy is a field of anatomy dedicated to the study of human tooth structures. The development, appearance and classification of teeth fall within its purview. Tooth formation begins before birth, and teeth's eventual morphology is detected during this time.

Most of the teeth have distinguishing features as shown in Fig. 2.1. There are 16 permanent teeth available in both maxilla and mandible jaw [3]. Figure 2.2 refers to a healthy tooth cut in half lengthways showing the layers of the tooth and its internal structure, as well as how the tooth relates to the gum and surrounding jaw bone.

The *crown* is the part of the tooth that is visible above the *gum (gingiva)* and is covered with enamel which protects the underlying dentine [3].

The *neck* is the region of the tooth that is at the gum line, between the root and the crown.

The *root* is the region of the tooth that is below the gum. Some teeth have only one root (e.g. incisors and canine ("eye") teeth), whereas molars and premolars have four roots per tooth.

The *enamel* is the hardest substance in the human body, harder even than bone. It gains its hardness from tightly packed rows of calcium and phosphorus crystals within a protein matrix structure.

Dentine is slightly softer than enamel, with a structure more like bone. It is elastic and compressible in contrast to the brittle nature of enamel. It is sensitive and contains tiny tubules throughout its structure that connect with the central nerve of the tooth within the pulp. It is a "live" tissue.

The *pulp* forms the central chamber of the tooth. The pulp is made of soft tissue and contains *blood vessels* to supply nutrients to the tooth, and *nerves* to enable the

K. R. Jain, N. C. Chauhan, *Dental Image Analysis for Disease Diagnosis*,
https://doi.org/10.1007/978-3-030-14136-3_2

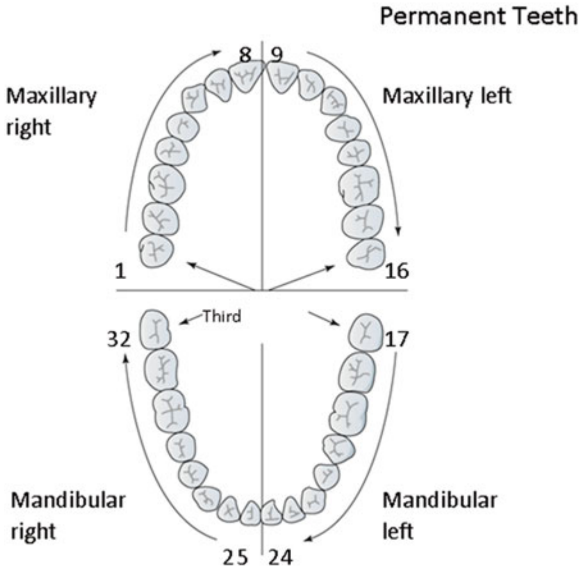

Fig. 2.1 Dental anatomy

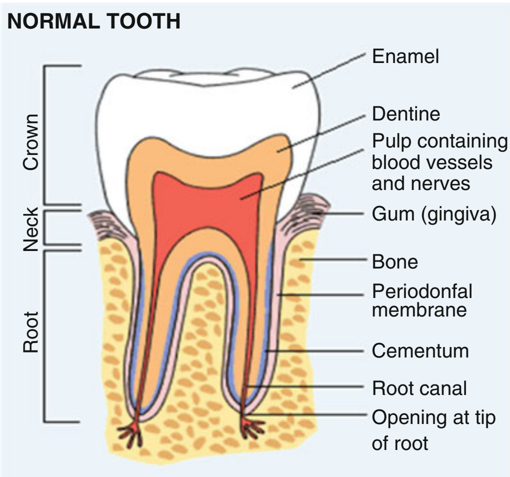

Fig. 2.2 Tooth structure

tooth to sense heat and cold. It also contains small lymph vessels which carry white blood cells to the tooth to help fight bacteria.

Dental plaque is a tooth disease caused by the complex interactions of starch and sugar supplied via food. This plaque produces acids leading to decay of minerals in enamel region. This is a simple case of decay of protein level in tooth which if untreated leads to formation of deep cavities with bacterial infection in pulp areas. These cavities or bacterial infection further leads to infection in gingival tissues.

2.1.2 Digital Dental Radiographs

The radiograph's influence in the medical field and society at large has affected in a vast form. The adaption of radiograph (X-ray of body parts) in our day to day life is increasing rapidly. Mammogram, orthopaedic treatment, dental analysis and luggage verification are few daily routine activities nowadays. More details about types of dental radiographs, their usage and advantages have been already discussed in Sect. 1.1.

2.1.3 Stomatology

Stomatology consists of diagnosis, treatment and prevention of caries affected tooth from rest part of the dental structure. It is broadly divided in four categories.

- *Therapeutic stomatology*: In this category the dental decay and further complications are dealt.
- *Periodontic stomatology*: It consists of diseases associated with periapical dental radiograph. It includes the tissues and oral cavity mucous membrane diseases.
- *Orthopedic stomatology*: Anomalies of jaws and irregularities of single tooth or a group of teeth inclusive of their diagnosis treatment and prevention is associated with it. Removable dentures, crowns and bridges fall under the stomatology of orthopaedic category.
- *Surgical stomatology*: It defines the surgical treatment of inferior alveolar nerve and third molar impaction of tooth in upper and lower jaw.

2.1.4 Associated Dental Problems

In the present world of dentistry, few software incorporating analytical knowledge of dental problems are available in the market for medical practitioners. These software assist practitioners in order to diagnose various dental problems and on the basis of which practitioners proceed further for their treatment. During formulation of our research problem, we interacted with a few dental practitioners and jointly identified a set of common dental problems being practiced by them to work upon during our research task. These dental problems are mainly associated with caries and dental growth. At first it is necessary to understand these problems in medical terms followed by their diagnosis using engineering skills. These dental problems are classified in six categories namely idiopathic resorption, identification of abscess and cyst, dental implants, endodontic treatment (RCT/Capping) and impacted third molar. Each of these dental problems is discussed further in the following subsections.

2.1.4.1 Idiopathic Resorption

In dentistry, *root resorption* is the breakdown or destruction, and subsequent loss, of the root structure of a tooth. This is caused by living body cells attacking part of the tooth. When the damage extends to the whole tooth, it is called *tooth resorption*. Severe root resorption is very difficult to treat and often requires the extraction of teeth.

Deciduous root resorption is a natural process which allows for exfoliation of the primary teeth to make way for the secondary teeth [10].

Root resorption of secondary teeth can occur as a result of pressure on the root surface. This can be from trauma, ectopic teeth erupting in the path of the root, inflammation, excessive occlusal loading, aggressive tumours and growths. Idiopathic resorption is broadly classified in two categories, internal and external resorption.

Internal (Central) Idiopathic Resorption It results in localised increase in the size of the pulp due to idiopathic pulpal hyperplasia. When the internal resorption occurs in a crown, the expanding pulp chamber perforates the dentin and involves the enamel, giving the enamel a pinkish discolouration as shown in Fig. 2.3(a), (b). Figure 2.3(c–e) shows the internal idiopathic resorpted radiographs of patients.

External (Peripheral) Idiopathic Resorption It can occur on any surface of a crown or root of a tooth. The crown of an erupted tooth cannot undergo external idiopathic resorption because its enamel surface is not surrounded by viable tissue (bone) However, external resorption can occur on the crown of an embedded tooth. If external resorption occurs on the root of a tooth, the resorptive process is followed by bone filling-in process of the excavated space. If the process of root resorption continues, it may result in the exfoliation of the crown or a spontaneous fracture of the root as shown in Fig. 2.4(a–e).

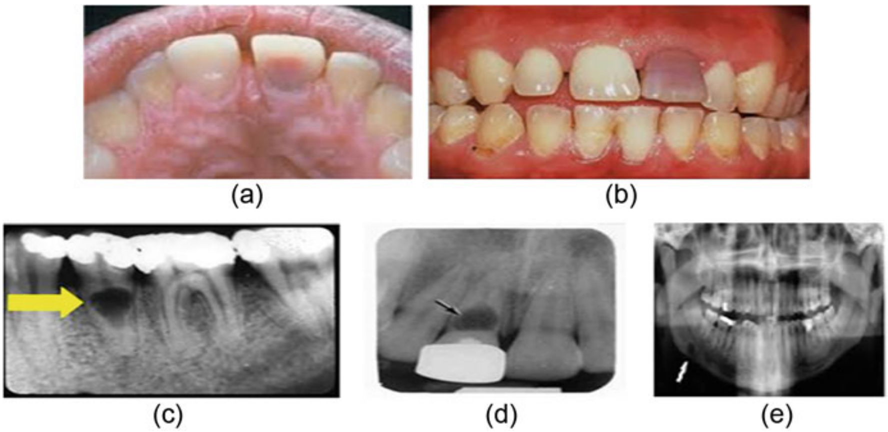

Fig. 2.3 Internal periapical dental radiograph. (**a**) and (**b**) are actual images representing periapical view of dental radiograph, while (**c**), (**d**) and (**e**) indicate their identification in dental radiographs by domain experts {Courtesy: Dr Ronak Panchal}

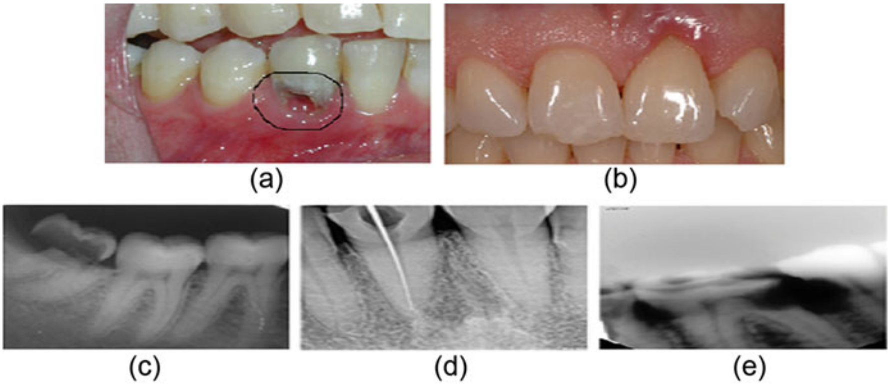

Fig. 2.4 External periapical dental radiograph. (**a**) and (**b**) are periapical view of exfoliation of the crown or a spontaneous fracture of the root, while (**c**), (**d**) and (**e**) are dental X-rays indicating external resorption {Courtesy: Dr Ronak Panchal}

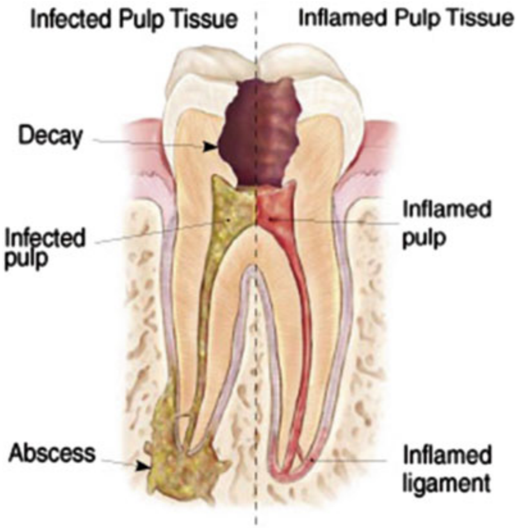

Fig. 2.5 Abscess representation in tooth {Courtesy: Dr Ronak Panchal}

2.1.4.2 Abscess and Cyst

A tooth abscess is a complication of tooth decay. It is shown in Fig. 2.5. It may also result from trauma to the tooth, such as when a tooth is broken or chipped. Openings in the tooth enamel allow bacteria to infect the centre of the tooth (the pulp). Infection may spread out from the root of the tooth and to the bones supporting the tooth [11].

Fig. 2.6 X-rays of patient representing abscess {Courtesy: Dr Ronak Panchal}

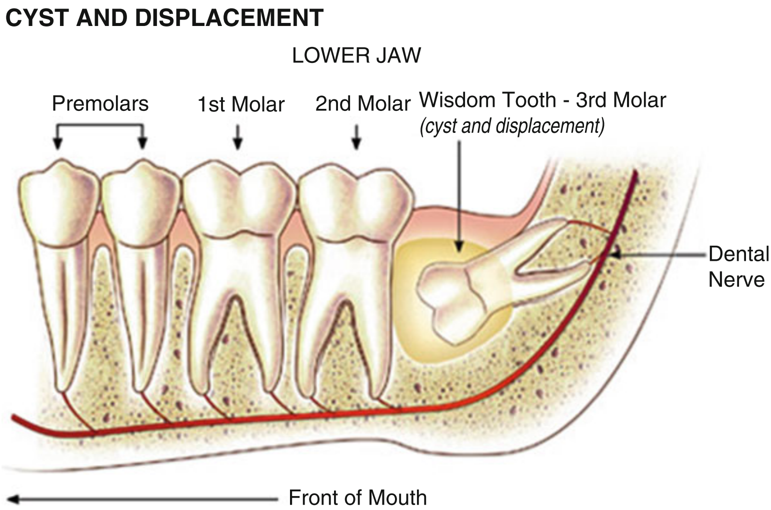

Fig. 2.7 Representation of cyst in tooth {Courtesy: Dr Ronak Panchal}

Infection results in the collection of pus (dead tissue, live and dead bacteria, and white blood cells) and swelling of the tissues within the tooth. This causes a painful toothache. If the pulp of the tooth dies, the toothache may stop, unless an abscess develops. This is especially true if the infection remains active and continues to spread and destroy tissue. The dental radiograph representing Abscess is shown in Fig. 2.6.

The *periapical cyst* (also termed as *radicular cyst* and, to a lesser extent, *dental cyst*) is the most common odontogenic cyst. It is caused by pulpal necrosis secondary to dental caries or trauma. The cyst lining is derived from the cell rests of Malassez. Usually, the periapical cyst is asymptomatic, but a secondary infection can cause pain. On radiographs, it appears a radiolucency (dark area) around the apex of a tooth's root [3].

Radicular cyst is the most common odontogenic cystic lesion of inflammatory origin. It is shown in Fig. 2.7. The dental radiograph representing cyst is shown in Fig. 2.8(a) and patient suffering from cyst is shown in Fig. 2.8(b).

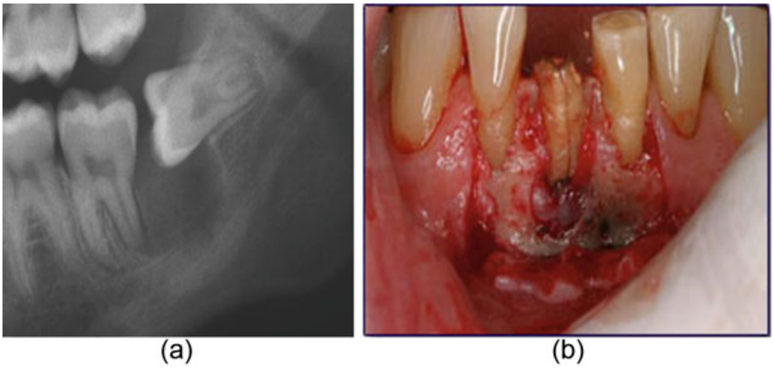

Fig. 2.8 Dental radiograph & patient representing cyst {Courtesy: Dr Ronak Panchal}

2.1.4.3 Dental Implants

A *dental implant* is a “root” device, usually made of titanium, used in dentistry to support restorations that resemble a tooth or group of teeth to replace missing teeth. The bone of the jaw accepts and Osseo integrates with the titanium post. Osseo integration refers to the fusion of the implant surface with the surrounding bone. Dental implants will fuse with bone; however, they lack the periodontal ligament, so they will feel slightly different from natural teeth during chewing [10]. The models representing IAN and third molar are shown in Fig. 2.9(a–d).

2.1.4.4 Endodontic Treatment (RCT/Filling)

Endodontic therapy or root canal therapy (RCT), colloquially root canal, is a sequence of treatment for the pulp of a tooth which results in the elimination of infection and protection of the decontaminated tooth from future microbial invasion. This set of procedures is commonly referred to as a “root canal”.

Endodontic therapy involves the removal of these structures, the subsequent shaping, cleaning and decontamination of the holes with tiny files and irrigating solutions, and the obturation (filling) of the decontaminated canals with an inert filling such as gutta percha and typically a eugenol-based cement. After endodontic surgery the tooth will be “dead”, and if an infection is spread at the apex, root end surgery is required. Although the procedure is relatively painless when done properly, the root canal remains a stereotypically fearsome dental operation. The model representing the RCT and fungal growth is shown in Fig. 2.10 [10].

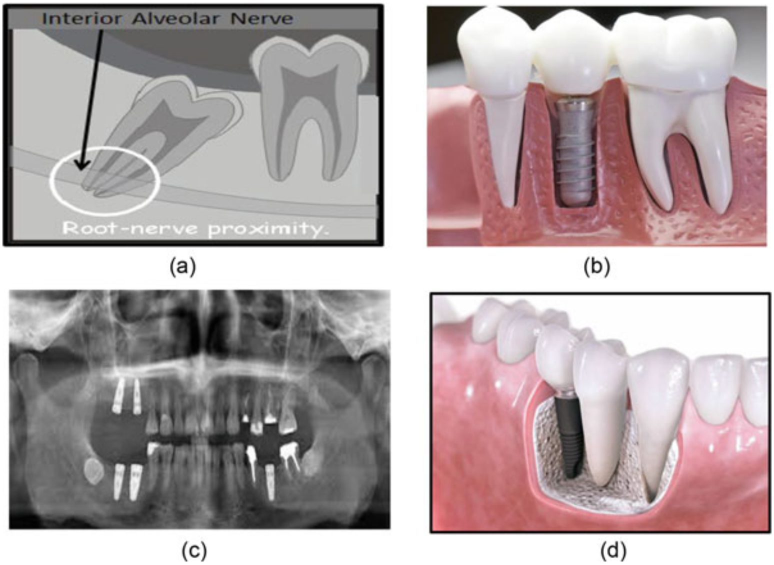

Fig. 2.9 Models and X-ray of patient representing dental implants. (**a**), (**b**) and (**d**) represent the models of IAN and third molar, and (**c**) represents the dental radiograph of third molar implantation. {Courtesy: Dr Ronak Panchal}

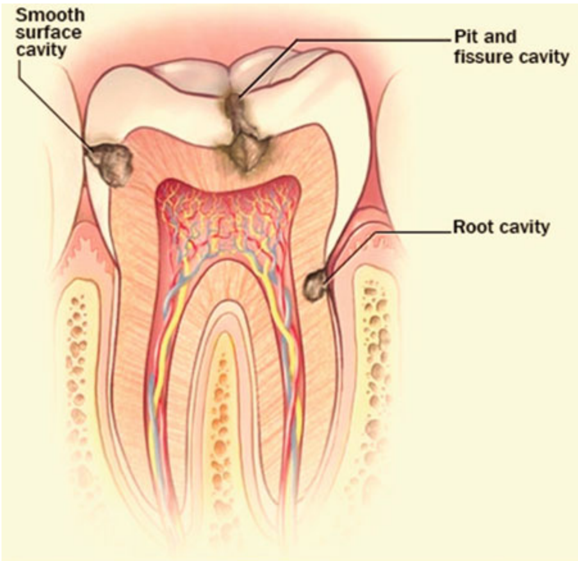

Fig. 2.10 Model representing decayed tooth for RCT/filling {Courtesy: Dr Ronak Panchal}

2.1.4.5 Impacted Third Molar

A *wisdom tooth*, in humans, is any of the usual four *third* molars. Wisdom teeth usually appear between the ages of 16 and 25. Most adults have four wisdom teeth, but it is possible to have fewer or more, in which case the extras are called supernumerary teeth. Wisdom teeth commonly affect other teeth as they develop, becoming impacted or "coming in sideways". They are often extracted when this occurs [12]. Impacted wisdom teeth (i.e. those that have failed to erupt through the gum line) fall into one of several categories:

Horizontal impaction (3%) is the least common form, which occurs when the tooth is angled fully 90° sideways, growing into the roots of the second molar as shown in Fig. 2.11(a).

Mesioangular impaction is the most common form (44%), and means the tooth is angled forward, towards the front of the mouth as shown in Fig. 2.11(b).

Vertical impaction (38%) occurs when the formed tooth does not erupt fully through the gum line as shown in Fig. 2.11(c).

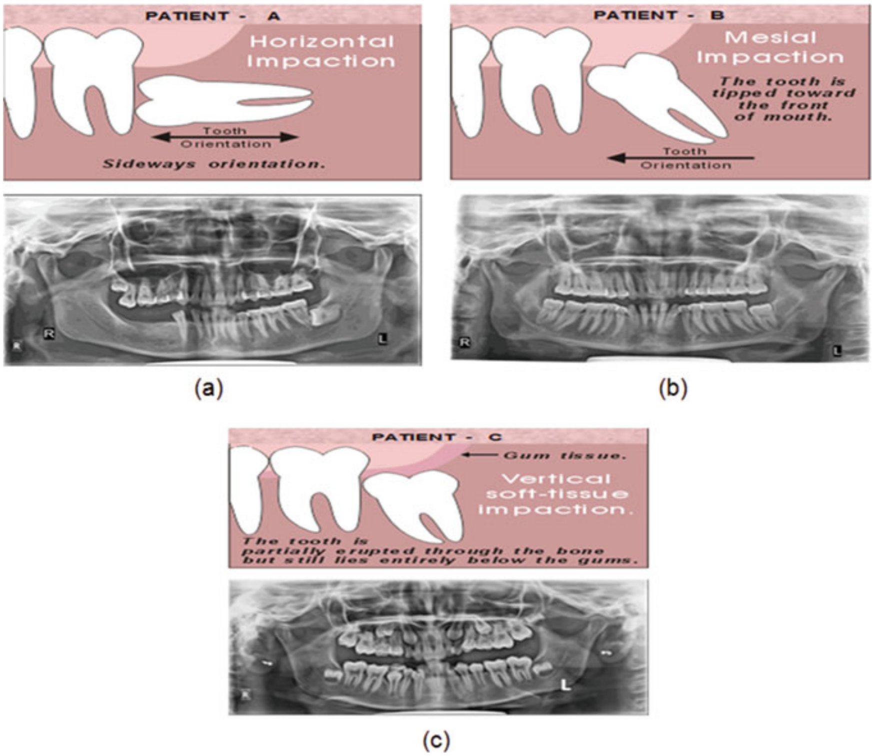

Fig. 2.11 Types of impacted third molar {Courtesy: Dr Ronak Panchal}. (**a**) Horizontal impaction. (**b**) Mesial impaction. (**c**) Vertical soft tissue impaction

Typically mesioangular impactions are the most difficult to extract in the maxilla (upper jaw) and easiest to extract in the mandible (lower jaw), while distoangular impactions are the easiest to extract in the maxilla and most difficult to extract in the mandible. Mostly, a fully erupted upper wisdom tooth requires bone removal if the tooth does not yield easily to forceps or elevators. Failure to remove distal or buccal bone while removing one of these (tooth) can cause the entire maxillary tuberosity to be fractured off, thereby tearing out the floor of the maxillary sinus [12].

Based on the aforesaid research problems, a state-of-the-art review of literature in dental image analysis domain for detection and diagnosis of caries is presented in the next two sections. The review is broadly divided into two categories. The first category of literature review reflects image enhancement techniques on digital dental radiographs. The second category of survey was done for the research work being carried out to extract the affected areas, that is, caries using image segmentation and feature extraction from digital dental radiographs. This review comprised various automatic and semi-automatic region growing methods for diagnosis of caries in digital dental radiographs.

2.2 A Review on Image Enhancement in Dental Radiographs

Bardia Yousefi et al. in 2012 enhanced the visibility of digital dental X-ray using wavelet image fusion and Bayesian classifier. With the help of these two techniques location of teeth and canals was identified. Their proposed process as shown in Fig. 2.12 was applied on 30 radiographs of 30 different patients. The size of structuring elements was 1×4 and that of MO filter was 3×3. Their results so obtained are displayed in Fig. 2.13. The pitfall of the research, as summarised by the author, is that the number of teeth having same intensity as that of background cannot be detected. Along with it the amount of intensity in a few canals affects the accuracy of classification. Moreover, the classification error increases because of the presence of fine particles in dental X-ray images [2].

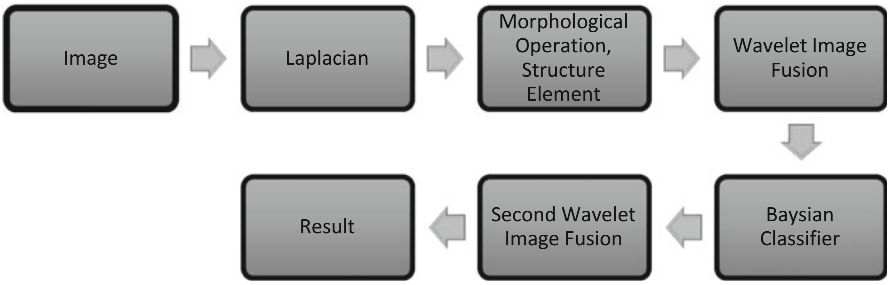

Fig. 2.12 Block diagram of the process followed [2]

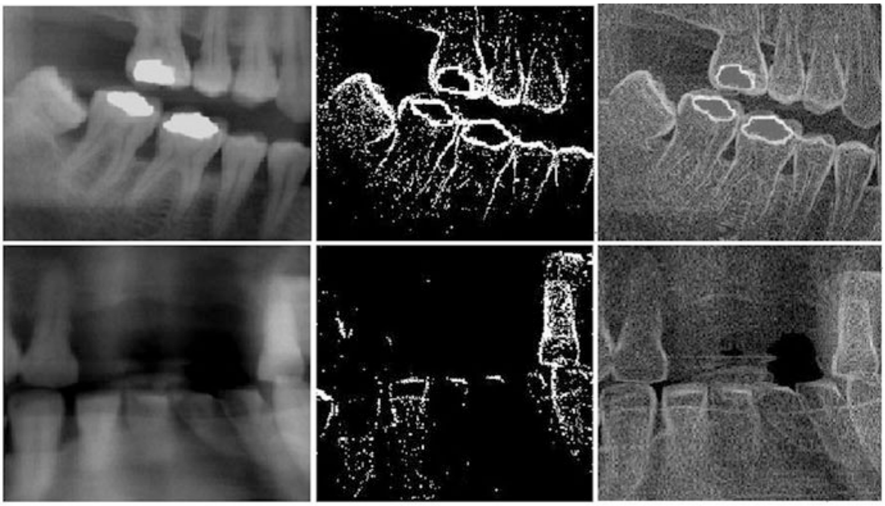

Fig. 2.13 RCT application using Bayesian classifier and wavelet fusion [2]

Classification of dental caries is important for the diagnosis and treatment planning of the dental disease, which has been affecting a very large population throughout the globe. Oprea et al. mentioned a detailed study and investigations about the nature of the dental disease [5]. Their proposed method examines the extent to which the caries lesion is present and then classifies the type of caries present in the dental radiograph.

The radiographic image is first captured using an appropriate X-ray imaging device, connected to the image analysis system. The image is captured along a line parallel to the long axis of the tooth. The dental X-ray image (Fig. 2.14(a)) is initially segmented into individual tooth (Fig. 2.14(b), (c)) which is followed by binarization of the tooth pattern (Fig. 2.14(d)). The edge detection of the segmented tooth yields the outline of the dental cavity. By determining the number of caries affected pixels, the region area may be extracted (Fig. 2.14(f), (g)). If there exists only one black region and there is an adjacent white border, that is, black caries region is adjacent to the white border enclosing the tooth, then the caries is classified as pulpal. If on the other hand there exists two or more number of black regions and the width of the black region is less than 2 mm then it is enamel caries. It may be pointed out here that the thickness of enamel around the tooth is approximately 2 mm. Alternately, if it is more than 2 mm it means that it is dentinal caries.

Ahmed et al. proposed comparative study of compound enhancement algorithms on dental radiograph images [13]. The ten abnormal images so chosen were noisy, blur edges and lower in contrast. The images underwent enhancement techniques like Sharp Adaptive Histogram Equalisation (SAHE), Sharp Median Adaptive Histogram Equalisation (SMAHE) and Sharp Contrast Adaptive Histogram Equalisation (SCLAHE). The main objective was to detect periapical radiolucency and widened periodontal ligament space along with loss of lamina dura. The

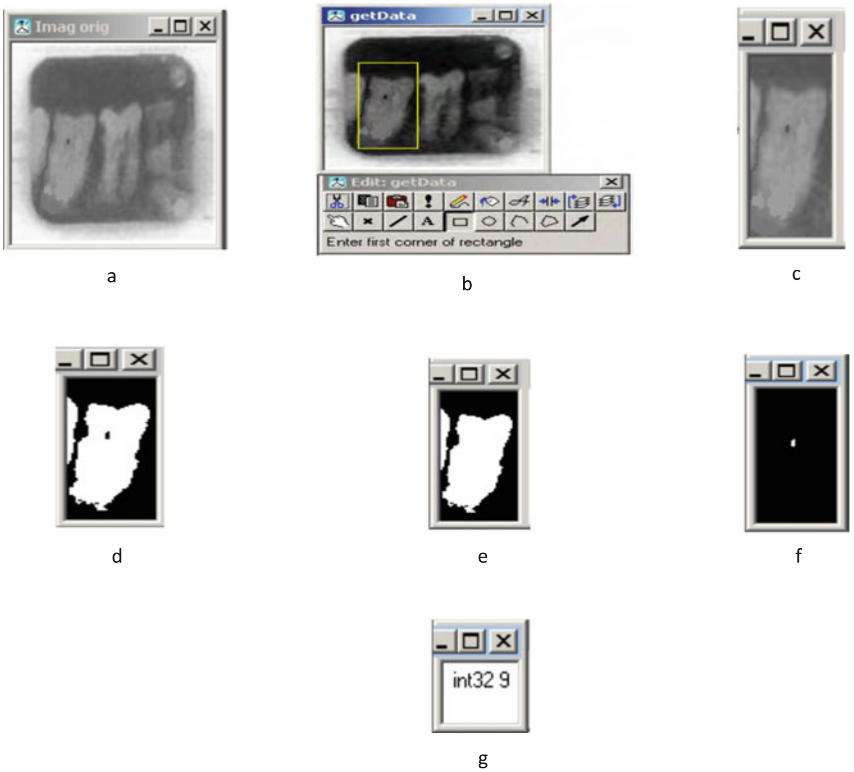

Fig. 2.14 Image processing for dental X-ray image analysis [5]. (**a**) Dental X-ray image. (**b**) Selected tooth (tooth with caries). (**c**) Segmented tooth with caries. (**d**) Binarization of the tooth. (**e**) Tooth pattern without caries. (**f**) Caries pattern. (**g**) Number (9) of caries affected pixels

important parameters so analysed were image quality perception, pathological perception and detected pathologies. SCLAHE was found to be the most useful technique among these.

In 2007, Stefan et al. presented state-of-the-art X-ray screening systems using image enhancement functions like colour inversion edge enhancement, organic only, metal only, etc. [14]. These functions were applied to various aviation security, cabin baggage screening (CBS) & hold baggage screening (HBS). Various filters used for the purpose of testing were grey scale, luminance high, luminance low, luminance negative, metal only, metal stripping, organic only, original, organic stripping and super enhancement. A total of 443 scanners of airport were scanned in 6 months. The most important part of the experiment was to decide which filter to be used when if the sequence is wrong the system gets alarmed. There were times when some of the IEF functions were not used but that does not mean that those functions are to be neglected or discarded as they may be useful for some other conditions. At the end switching between filters was still under consideration. Moreover, the results were too variable to decide which filter is appropriate for a particular application.

2.3 Review on Image Segmentation and Feature Extraction in Dental Radiographs

2.3.1 Segmentation and Extraction Using Basic Image Processing Properties

Said et al. presented an idea of dental X-ray image segmentation [15]. In this paper the authors presented an overview about an automated dental identification system for missing and unidentified persons. This dental identification system can be used by both law enforcement and security agencies in both forensic and biometric identification. These techniques address the problem of identifying each individual tooth and how the contours of each tooth are extracted. The authors used periapical and bitewing views of PM dental X-ray images on which grey-scale stretching transformation was used for enhancement (Fig. 2.15).

The second step is to perform segmentation using morphological filtering in which they used both the top-hat and the bottom-hat filters on the original image. The horizontal line separating the upper jaw, lower jaw and vertical edges is processed using 2D wavelet kernels. Further they are used to project vertical and horizontal boundaries of individual tooth. Boundaries of each region were matched with the horizontal and vertical boundaries in the AM dental radiograph image [15] (Fig. 2.16).

Unfortunately, there were few PM databases which were not enhanced using morphological filtering not enhanced using morphological filtering as shown in Fig. 2.17. Hence, wavelet based multiresolution property of segmentation was used to detect the boundaries.

A dental biometric system published in 2012 could be used in forensic science [16]. In this system, proposed AM radiograph matching with PM radiograph to

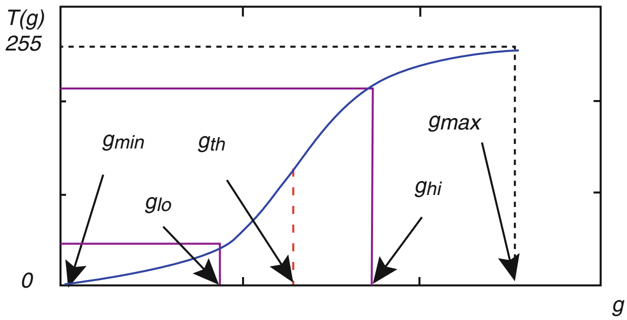

Fig. 2.15 Grey-scale contrast stretching transformation [15]

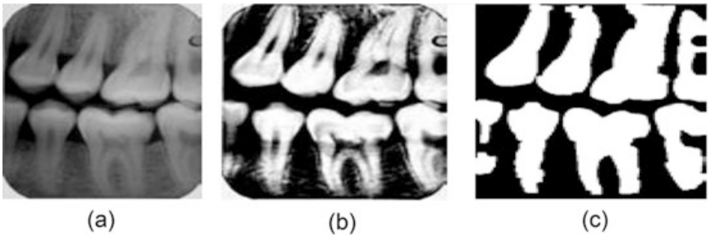

Fig. 2.16 Teeth segmentation [15]. (**a**) Original image. (**b**) Result of top-hat enhancement. (**c**) Morphological operation

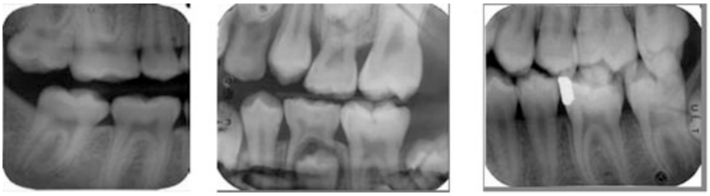

Fig. 2.17 Wavelet based segmented image [15]

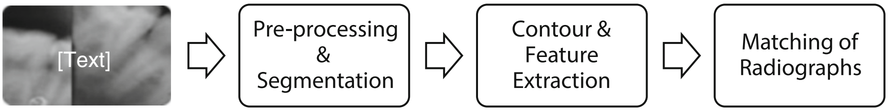

Fig. 2.18 Block diagram of dental identification system [16]

identify unidentified individual. Dental biometrics consists of four steps as: preprocessing of dental radiograph, segmentation, feature extraction and matching of AM and PM radiograph. Segmentation is a method used for feature extraction like shape and size of tooth. These features are used in matching of two radiographs and based on this matching, individuals can be identified. In this paper segmentation is used to extract single tooth and also for the dental work extraction.

The block diagram of their proposed method is shown in Fig. 2.18. The radiographs are firstly preprocessed, and unwanted background present with teeth is later on filtered out. Histogram equalisation is used for getting uniform histogram. Segmentation is performed by using edge detection tools. The authors used morphological and image cropping operation for single tooth extraction. Thresholding gives best result for dental extraction. Matching is a last stage of dental biometric system which finds out difference between two dental radiographs. Differentiation between two radiographs is found out based on properties like area of tooth or dental work, mode, median, skewness and kurtosis. Skewness, kurtosis and mean are the histogram features. Matching based on distance is posed in the future work of this approach. Distance between teeth can be calculated using that method.

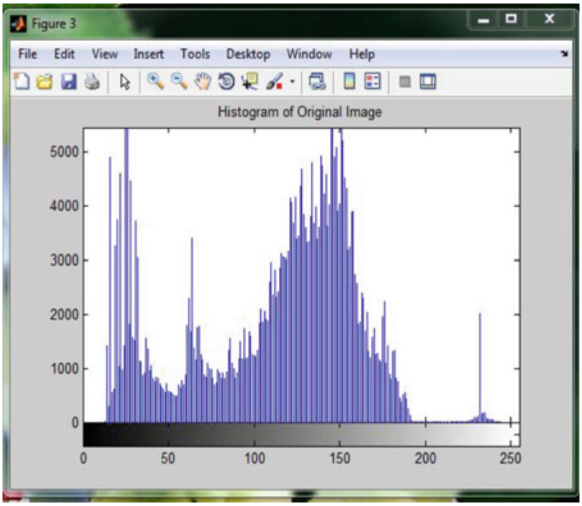

Fig. 2.19 Histogram of original image [16]

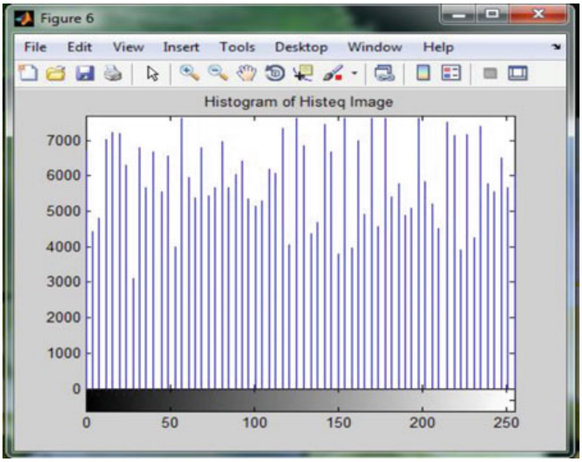

Fig. 2.20 Histogram of histogram equalised image [16]

So in the event of missing tooth it can give perfect analysis of query image. The histograms and extracted portions are shown in Figs. 2.19, 2.20, and 2.21.

Special feature extraction of teeth from X-ray teeth films using image processing was proposed by Kiattisin et al. [17]. In this study teeth pictures were scanned and adjusted by a scanner and a computer, respectively. These X-rays were further converted to a binary code and decoded to the direction code (chain code). The chain code of image was compared with statistical chain code.

Figure 2.22 shows two samples of teeth films for comparisons. Figure 2.23 shows the effects of comparing two teeth films in the case of no chain code in which total comparisons are nine times per one match. However, Fig. 2.24 shows

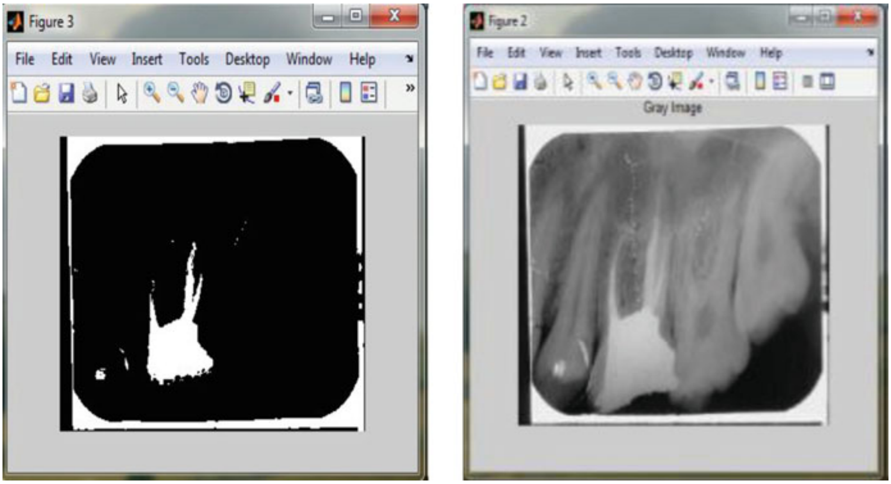

Fig. 2.21 DW extracted [16]

H1	H2	I1
1	2	3

I1	I2	H3
3	4	5

Fig. 2.22 Two samples of teeth films for comparisons [17]

1*3	1*4	1*5
2*3	2*4	2*5
3*3	3*4	3*5

Fig. 2.23 Comparing teeth films in case of no chain code [17]

H1*H3	H2*H3	I1*I1	I1*I2

Fig. 2.24 Comparing teeth films in case of decoded chain code [17]

the results of comparing two teeth films in the case of using a decoded chain code. It can reduce the total comparisons from nine times to four times because H and I patterns from the first teeth film can directly match to H and I, respectively, from the second teeth film.

The percentage of the same chain code is approximately 90% (i.e. matching same patterns) for the comparison of one root to one root (seven times) and two roots to two roots (seven times) while the percentage of the same chain code is reduced at

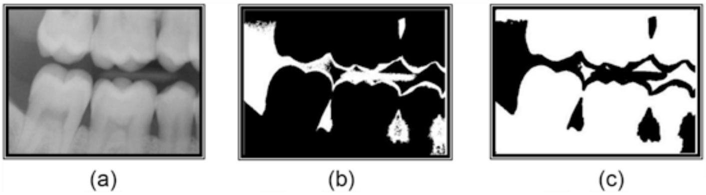

Fig. 2.25 Extraction of individual tooth using CBIR [18]. (**a**) Dental image. (**b**) Region grown image. (**c**) Eroded image

relatively below 50% (i.e. matching different patterns) for comparison of one root to two roots (two times).

In 2012, Desai et al. proposed a simple and novel CBIR technique to extract individual tooth [18]. In this method, region growing algorithm is applied on dental image as shown in Fig. 2.25a. Median filter is used to remove impulse noise. After extracting individual tooth, different features like tooth area, major axis length and minor axis length are extracted.

Feature vector is developed by combining all three features for all teeth of a dental image and database is created of different dental radiographs. Matching between AM and PM dental radiographs is done by finding distance vectors between their feature vectors.

Based on the minimum value of distance vector, conclusion is derived that which dental image is better match with database [18]. The results of suggested method are shown in Fig. 2.25(b), (c).

Omanovic published an exhaustive matching of dental X-rays for human forensic identification [19]. In this paper the degree of similarity/overlap between two radiographs is obtained by weighted sum of squared differences (SSD) cost function. The method was tested on a database of 571 radiographs belonging to 41 distinct individuals. A total of 150 identification scenarios were taken then each single ROI was run for comparing and matching with the dental X-ray images.

The authors proposed a computer-aided framework for matching of dental radiographs based on a sum of squared differences cost criterion. In their proposed framework, the operator would define the ROI by roughly circling the tooth of interest on a given post-mortem radiograph. Hence, even untrained staff would be able to participate in the identification efforts by roughly circles the tooth area. The system itself then matches the selected region to radiographs found in the ante mortem database as shown in Fig. 2.26. For all possible shifts, the best brightness and contrast adjustment and rotation were computed, and the parameters that yielded the lowest cost are recorded along with the associated cost (match score). The radiographs in the database were then ranked according to the cost, with the lowest cost indicating the best match as shown in Fig. 2.27. Their work can be extended on multiple ROIs as well as on different dental images [19].

Lailee investigated the fundamental problems in image segmentation using traditional segmentation techniques and proposed an improved technique for

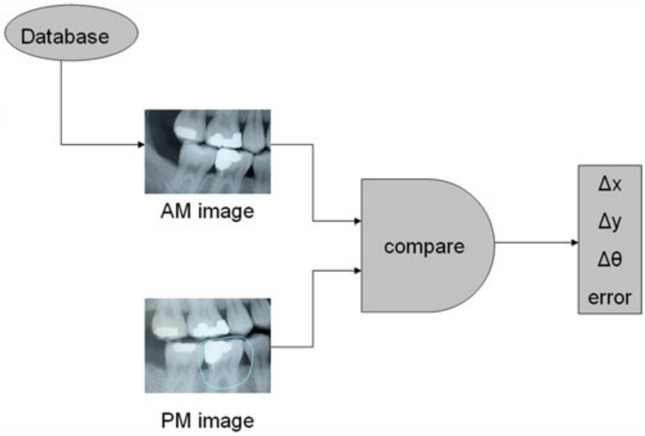

Fig. 2.26 Illustration of the identification test run [19]

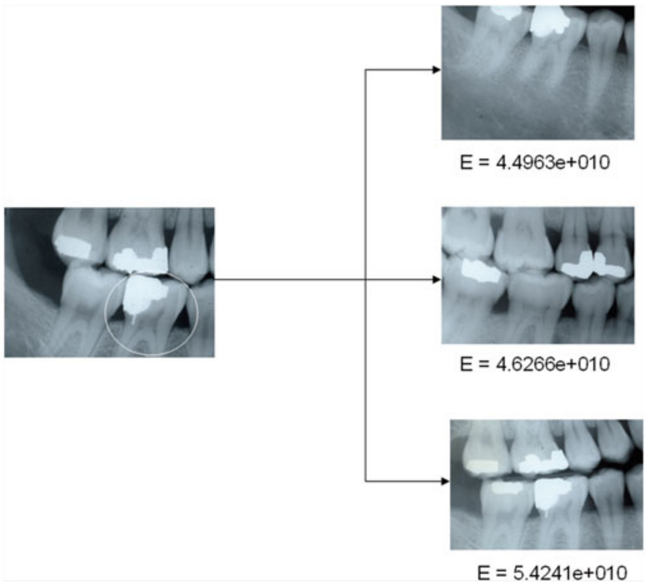

Fig. 2.27 A query image and the top three radiographs in the database ranked by the associated cost [19]

segmenting images captured under natural environment [20]. Due to non-uniform illumination it is difficult to produce a significant threshold value along with lack of difference in reflection. Since different illumination may produce different colour intensity of the object surface and thus lead to inaccurate segmented images. The widely used traditional method for Thresholding is Ostu and fuzzy C-means respectively. In it the authors have added an extra step after thresholding with Ostu method by converting the grey-scale image into binary and then integrating the modified threshold algorithm with an inversion technique. The results were analysed based on rand index function.

In 2005, a system for human identification from X-ray dental radiographs was prepared by Nomir [21]. Their proposed system retrieves the best matches from an ante mortem (AM) database. The system automatically segments dental X-ray images into individual teeth and extracts the contour of each tooth. Features are extracted from each tooth and are used for retrieval. They developed a new method for teeth separation based on integral projection. They also developed a new method for representing and matching teeth contours using signature vectors obtained at salient points on the contours of the teeth. During retrieval, the AM radiographs that have signatures closer to the PM are found and presented to the user. Matching scores are generated based on the distance between the signature vectors of AM and PM teeth.

They introduced iterative and adaptive thresholding. Thereafter horizontal and vertical integral projection is used for separating the jaws as well as individual tooth. The important steps of the segmentation algorithm are shown in Fig. 2.28.

This technique was not successful in matching images due to poor quality of images and shape of teeth could have changed with time as PM images were taken after a long time AM images were captured.

Teeth segmentation from dental radiographic films is an essential step for achieving highly automated post mortem identification. A mathematical morphology approach to the problem of teeth segmentation was presented Said et al. [15]. A grey-scale contrast stretching transformation to improve the performance of teeth segmentation is used. The proposed approach is shown in Fig. 2.29.

Closing top hat transformation is used to remove noise. After reducing the noise effect, the authors used threshold operation to separate the desired teeth from the background and the remaining noise. Thresholding produces a binary image that simplifies the image analysis. A group of pixels of the threshold image based on their connectivity and labels it to identify the different connected components.

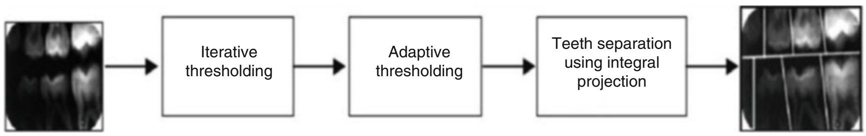

Fig. 2.28 Steps of a segmentation algorithm [21]

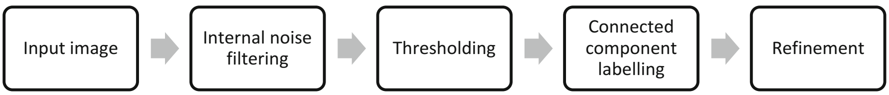

Fig. 2.29 Main stages of a segmentation algorithm [15]

The dimension of the neighbourhood, choice of edge detector and weights assigned to each pixel of the neighbourhood greatly influence the local image statistics and hence contrast. Tiwari et al. published an article centring on the issue of edge detection based upon the derivative approach [22]. The Laplacian mask evokes strong response to stray noise pixels. So, better utilisation of the Laplacian is to precede it by convoluting the image by a digital mask having a Gaussian function distribution to smoothen the image profile. Then apply the Laplacian mask on the smoothed image. The edges were found by differentiating a profile and finding where the differentiated image changes sign, corresponding to a maximum (or minimum) of the original profile.

2.3.2 Image Segmentation and Extraction Using Active Contour Modelling

To analyse any tongue image it is required to remove all these noise, like teeth and lips, and we need only the tongue area. In 2009, Xue-Ming et al. working in the same domain of research published an article in an international forum on information technology and applications for image segmentation technique in tongue diagnosis [23]. Many methods of tongue image segmentation have been proposed, but the former out of several ways is less adaptive, cannot be better to segment Tongue. The Snake method is one of these effective extraction method of the objectives outline based on the high-level information. The advantage of this method is that the final outcome of the process is a complete curve so we can get exact tongue image segmentation. The defects of traditional dynamic contour are: (1) Smaller convergence domain, Only dynamic contour of the initial outline of the goal line from the edge of division within a small area can be very good convergence (2) Exist re-entrant corner in the target cannot be converged. Because of these the traditional methods are less automatic and cannot be completely out of people's participation and also not suitable for large sample and clinical applications.

So to overcome these problems in this paper the author proposed a double Snakes model which is based on the traditional model of Snake and in the use of the tongue segmentation. The first step is to use median filter to remove noise image. The second step is transforms the image colour space to HIS colour space, and after that dual snake's algorithm is applied on that which obtains the accurate and complete tongue image. Experimental result of their proposed method is shown in Fig. 2.30 from which we can say that compared with the old segmentation methods such as threshold segmentation, region growing, watershed and snake method. The double snakes have a lower request on the initialisation of outline, and more accurate results of the segmentation.

Zhong et al. presented a novel method to segment the tongue image automatically with the mouth location method and active appearance model (AAM) [24]. In this method with the help of a particular feature of the mouth, dark hole's position

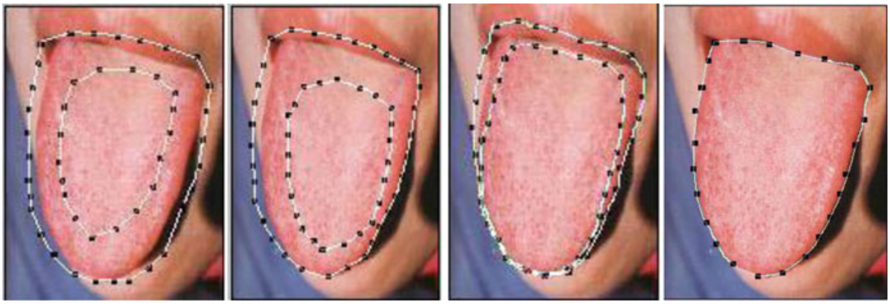

Fig. 2.30 Tongue segmentation process using double snakes [23]

Fig. 2.31 Original image and the binary one with threshold 50 [24]

Fig. 2.32 Image identifying the black hole and the other one predict the approximate area of tongue [24]

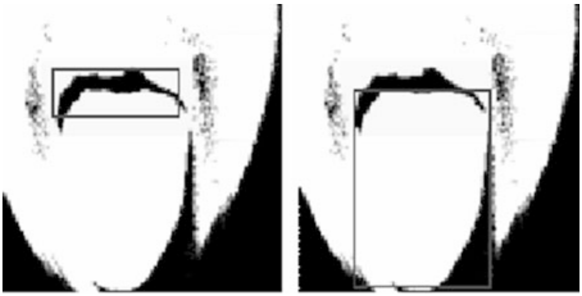

and the approximate area of the tongue were located and later extracted. After completing this preprocess the AAM is applied to segment the tongue from the image completely, which uses texture and shape of an object. Active Shape Model (ASM)uses only the shape information while AAM uses the shape and texture simultaneously. Unfortunately, some images may fail to locate the mouth hole, due to the blurred image and the closed mouth. In this paper a multi-initial displacement method is used to resolve the problem.

In Fig. 2.31 the original image is first of all converted to the binary image for the threshold 50. After that identification process of black hole is held and also prediction of approximation of tongue area is calculated which is shown in Fig. 2.32.

Here they assume the tongue length is 1.8 times than the mouth width, tongue width is 1.2 times than the mouth width. Finally AAM could be generated by combining a model of shape variations with a model of the texture variations in a shape normalised frame. So for that a set of labelled images for training is being used, where key landmark points are marked on each example object manually. Building a tongue model requires tongue images marked with points at key positions to outline the main features. Figure 2.33 (right) demonstrates the triangle meshes of the tongue for generating normalised shape image for the same.

Li et al. presented an automatic initialisation by the feature of tongue in the HSV space and compared different algorithms [25]. An improved level set method is implemented in tongue segmentation. Initialisation of tongue contour process is shown in Fig. 2.34. In this method first of all the original image (Fig. 2.34(a)) is

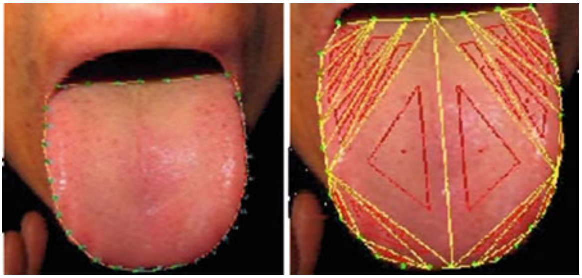

Fig. 2.33 Tongue image with 32 key landmarks (left) and the one with triangulated meshes (right) [24]

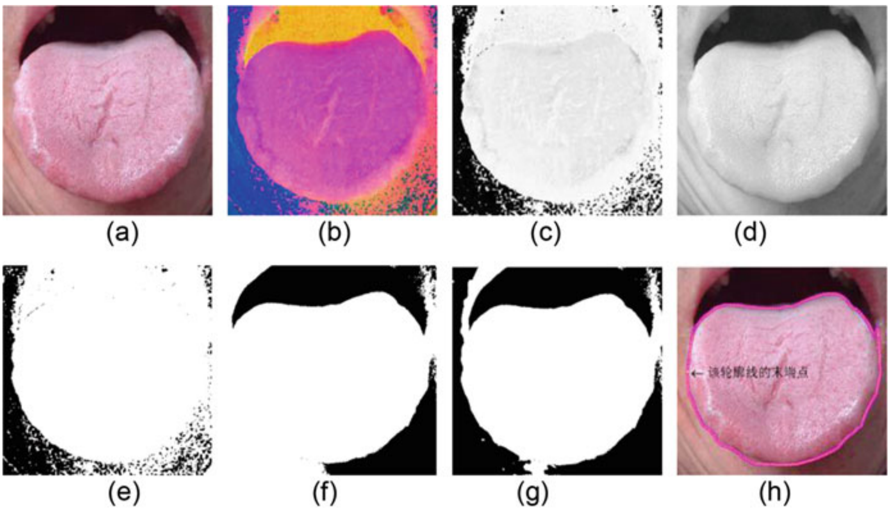

Fig. 2.34 Initialisation of the Active Contour [25]

transformed from the RGB space to the HSV space (Fig. 2.34(b)) and component H (Fig. 2.34(c)) is conversed into the binary image (Fig. 2.34(e)) and component V (Fig. 2.34(d)) is conversed into the binary image (Fig. 2.34(f)). After that we can get the initial contour curve of tongue. As is showed in Fig. 2.34(c–h), the smaller the value of H, the redder the tongue is. Therefore, H of the region of tongue is very small. We can see that the contour of root part of tongue can be attained according to Fig. 2.34(f). We can get Fig. 2.34(g) by the simple fusion of Fig. 2.34(e), (f). At last, we can get the initial contour (see Fig. 2.34(h)) of tongue by Fig. 2.34(a).

While applying their method to the 400 clinical tongue images, the correct segmentation rate reaches 98% according to the judgements obtained by experts in traditional Chinese medicine. Mainly, there are two problems arising in automated tongue image segmentation in tongue diagnosis system of traditional Chinese medicine firstly there are lots of pathological details on the surface of tongue, and secondly the shapes of tongue bodies are quite different. Wang provided a broader scope of research through his paper and presented a new approach for tongue segmentation, which introduces knowledge-based initial position detection and a colour gradient into the GVF snake [26]. They decompose the whole process of tongue segmentation into three steps.

- The boundary of tongue body is roughly detected by making use of characteristics of tongue body.
- The colour gradient of tongue image is calculated and homogenous region is set.
- Finally, the colour GVF snake is applied to extract tongue body.

Their proposed algorithm adequately considers colour property of tongue image and can avoid the primary problems of applying traditional snake. In this paper a new approach for tongue segmentation, which introduces knowledge-based initial position detection and a colour gradient into the GVF snake is presented. They also use the knowledge based rough tongue body boundary detection to solve the problem of noise sensitivity and computational complexity. Their segmentation results of two examples with widely different tongue shapes are shown in Fig. 2.35 which demonstrates the performance of their method. Original images are depicted in the first two columns. The main three steps for image segmentation in proposed algorithm are shown in Figure in the next two columns. In the first step, boundary of tongue body is roughly detected by making use of the characteristics of tongue body. In the second step, the colour gradient of tongue image is calculated and homogeneous region is set. Finally, the colour GVF snake is applied to extract tongue body. Experimental results on clinical tongue images demonstrate much potential to computerised tongue diagnosis of their approach.

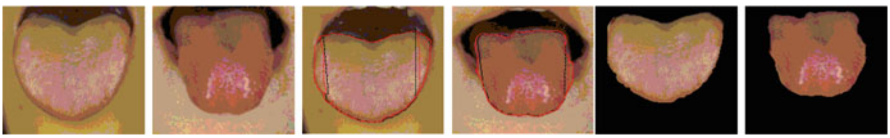

Fig. 2.35 Experimental step wise results on clinical tongue [26]

The experiments results of above Fig. 2.35 show robustness and accuracy of the algorithm. Experimental results on clinical tongue images demonstrate much potential to computerised tongue diagnosis of this approach.

2.3.3 Image Segmentation and Extraction Using Level Set Method and Machine Learning

In 2012, Rad et al. presented a method for automatic segmentation and feature extraction for dental X-ray images [27]. Their method is implemented using traditional image processing techniques which help in extracting boundary and contours, by using clustering k-mean method for segmentation, after image enhancement. Furthermore, they extracted some features of dental X-ray images using texture statistics techniques by grey-level co-occurrence matrix as shown in Figs. 2.36 and 2.37.

Their experimental technique is improved version of segmentation; however, it still needs further improvements. With the help of extracted data one can obtain the teeth measurements. These data are used for automatic dental systems as well as human identification. They further expected to separate the jaw to find the teeth so that better solution can distinguish each tooth using segmentation.

Rad et al. presented a method for segmentation and feature extraction of dental X-ray images using level-set method for segmentation after image enhancement and illustrate contour for teeth to complete the segmentation step [28]. They posed image segmentation problem as one of the most difficult tasks in image processing and it plays an important role in most subsequent image analysis, especially in pattern recognition and image matching as represented in Fig. 2.38.

To illustrate the segmentation of dental X-ray images using level set algorithm by distinguishing background, teeth and gum. To use these features they obtained a vector of features from each dental X-ray image. The segmented teeth represented with contour around each tooth, after segmentation of teeth image they extracted some textural features such as contrast, correlation, entropy, energy and homogeneity from grey-level co-occurrence matrices. The experimental results show that it is a promising technique for segmentation.

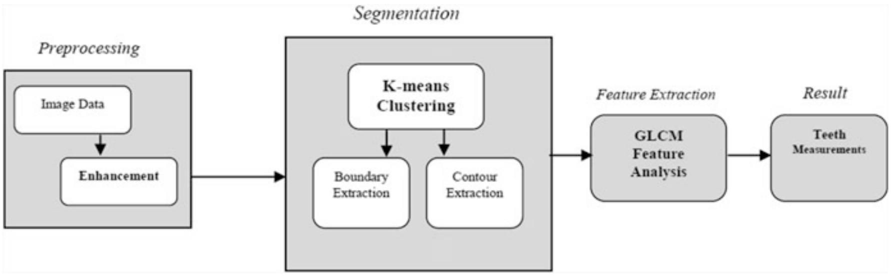

Fig. 2.36 Conventional dental X-ray image analysis system [27]

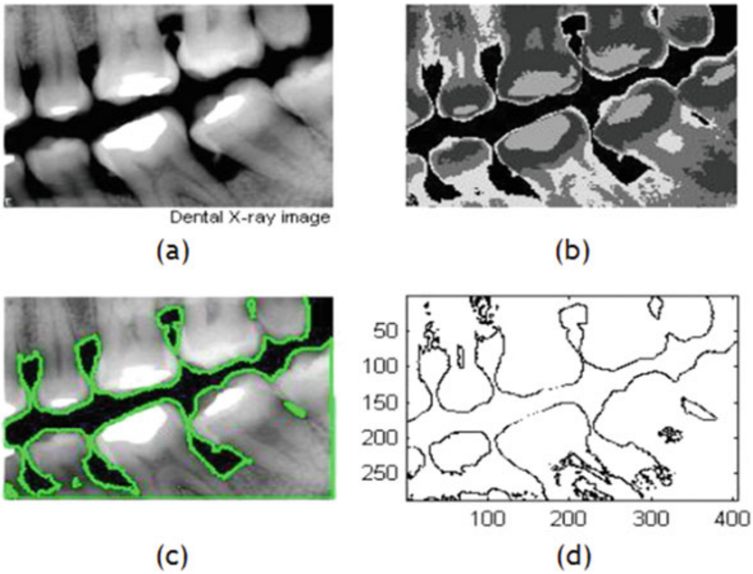

Fig. 2.37 Step wise results of proposed algorithm [27]. (**a**) Enhanced X-ray image. (**b**) Result of k-mean algorithm. (**c**) Segmented teeth with correspondence boundary around teeth. (**d**) Contour of teeth image

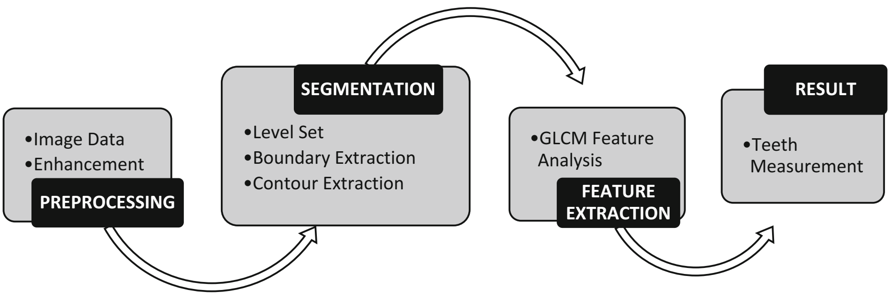

Fig. 2.38 Conventional dental X-ray image analysis system [28]

Po-Weli Huang in his paper highlighted that tooth isolation is a very important preprocessing step for both computer-aided dental diagnosis and automatic dental identification systems [29]. The accuracy of tooth isolation will directly affect the accuracy of feature extraction and thereby the final results of both types of systems.

The dataset comprises of 60 bitewing images for tooth isolation experiments. Among all the images of upper jaw, the total number of teeth is 252 and the number of missing teeth is 3, whereas among all images of lower jaw, the total number of teeth is 233, and the number of missing teeth is 4. They used all images from Taichung General Veteran Hospital, Taiwan.

Technique Used: (1) Nomir and Abdel-Mottaleb and (2) authors' method (horizontal separation, vertical isolation, over-segmentation, under-segmentation, missing tooth detection).

This paper presents a very effective and fully automatic tooth isolation method for bitewing dental X-ray images. The upper–lower jaw separation mechanism by author's method is based on grey-scale integral projection to avoid possible information loss and incorporates with angle adjustment to handle skewed images. In single tooth isolation, they proposed an adaptive windowing scheme for locating gap valleys to improve the accuracy.

(1) *Nomir and Abdel-Mottaleb*: They presented a tooth isolation method for a thresholded binary image. Their method can be described from the following three steps: iterative thresholding, separation between the upper and the lower jaws, and isolation of each individual tooth [30]. In other words, the tooth and its adjacent tooth-missing region are segmented together as one ROI, instead of two ROIs, of which one contains a tooth and the other contains a tooth-missing region. Such isolation result causes teeth numbering problem. Observing the vertical integral projection of the image, they find that the projection curve of the missing tooth region is rather flat and the values are low, while the curve of teeth region goes up and down like a hill.

Since dental radiographs always suffer from problems like noise, low contrast and uneven exposure, images are enhanced before performing tooth isolation. Figure 2.39 shows the isolation result of the image before and after applying missing-teeth detection. Notice that the tooth-missing region has been successfully detected and that two isolation lines have been added to each end of the tooth-missing region.

Their experimental results demonstrated that method achieves accuracy rates of 95.63% for the upper jaw images and 98.71% for the lower jaw images from a test database of 60 dental radiographs, respectively, which is higher than that of Nomir and Abdel-Mottaleb's method.

In 2013, Lira proposed a segmentation approach based on mathematical morphology [31]. The feature extraction stage is steered by a shape model based on principal component analysis (PCA). The panoramic X-ray shows the dentist a patient's nasal area, sinuses, jaw joints, teeth and surrounding bone (Fig. 2.40).

Along of the main axes the authors determine two measures: crown-body (CB) and root (R) lengths. The former is obtained through the distance from the

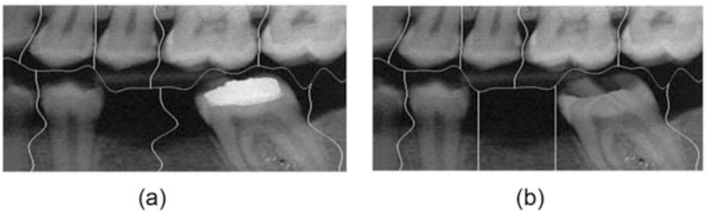

Fig. 2.39 Results without and with missing-teeth detection in (**a**) and (**b**) respectively [29]

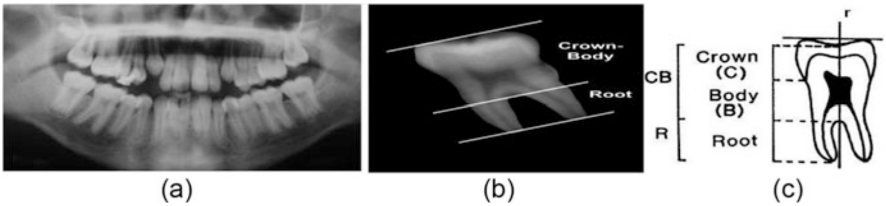

Fig. 2.40 Teeth segmentation and feature extraction from panoramic image. (**a**) A typical panoramic X-ray. (**b**) The scheme for crown-body (CB) and root (R) measurements. (**c**) Experimental result of an image [31]

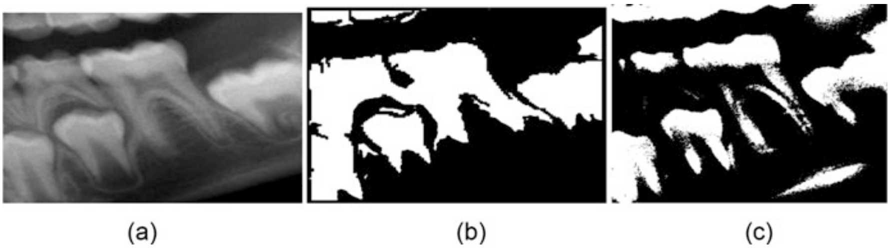

Fig. 2.41 Overlapping problem and suggested solution. (**a**) Original image. (**b**) Quad-tree segmentation (**c**) Zonal mask segmentation [31]

deepest pit to the furcation. The latter is the distance from the furcation to the root apex. Finally, we compute the ratio CB/R. The setting of parameters was done through experimentation. The best results were obtained width = 10:0 (for any i), $w = 6{:}0$ and $k = 2{:}5$, delta $t = 0{:}3$ and the number of iterations of the snake scheme of section were 120. The quad-tree threshold is $T = 12{:}0$. These parameters are used to set up the algorithms, such as snake model and quad-tree thresholding, the Otsu's thresholding result. The quad-tree and the generated mask are pictured respectively. Lastly XOR between the quad-tree mask and the Otsu's result is done (Fig. 2.41).

In 2015, Alsmadi developed a novel, fully automatic and effective method for jaw lesions in panoramic X-ray image segmentation [32]. The hybrid fuzzy C-means and Neutrosophic approach is used for segmenting jaw image and detecting the jaw lesion region in panoramic X-ray images which may help in diagnosing jaw lesions. Comparing the proposed approach with the Hybrid Firefly Algorithm with the fuzzy C-means, and the Artificial Bee Colony with the fuzzy C-means algorithm, the proposed approach produces the most identical lesion region to the manual delineation by the oral pathologist and shows better performance. This work utilises a new clustering approach (NFCM) that groups and clusters jaw's X-ray image pixels into background region and lesion region. Neutrosophy is the high noise reduction without image boundary blurring; thus, the result of segmentation is highly improved after the reduction in noise. So noise is iteratively reduced and the lesion region is strengthened or untouched as shown in flow chart of Fig. 2.42.

This work explores a novel neutrosophy application by combining fuzzy C-means with the domain components of neutrosophy. Area error metrics are used

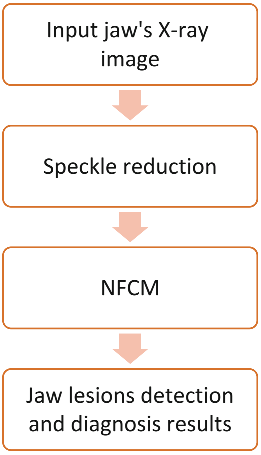

Fig. 2.42 Flow chart of algorithm [32]

to assess the performance and efficiency of their proposed approach from different aspects. Specificity, sensitivity and similarity analyses are conducted to assess the robustness of the proposed approach. It is clear that the proposed method (NFCM) has better performance as compared with the FCM, FAFCM and ABCFCM as shown in Fig. 2.43. It detects the lesion region more accurately. The future work of this research is to develop a classifier that can distinguish malignant and benign lesions of jaw in panorama images based on suitable and appropriate features extracted from the segmentation results.

Dental X-ray image segmentation (DXIS) is an indispensable process in practical dentistry for diagnosis of periodontitis diseases from an X-ray image. In 2016, Son et al. presented that performance of a clustering algorithm is enhanced when additional information provided by users is attached to inputs of the algorithm [33]. In this paper, the authors propose a new cooperative scheme that applies semi-supervised fuzzy clustering algorithms to DXIS. Clustering methods could be integrated with another type of algorithms to improve the performance, they considered the integration of the Otsu method, Fuzzy C-means (FCM) and the eSFCM. Specifically, the Otsu method is used to remove the Background area from an X-ray dental image. Then, the FCM algorithm is chosen to remove the Dental Structure area from the results of the previous steps. Finally, semi-supervised entropy regularised fuzzy clustering algorithm (eSFCM) is opted to clarify and improve the results based on the optimal result from the previous clustering method, a cooperative framework—eSFCM–Otsu in a flow chart manner. A given dental X-ray image with some user-defined parameters such as the number of clusters (C), the fuzzifier (m), the Otsu threshold [34] (T) and the stopping threshold (ε) is inputted in the framework.

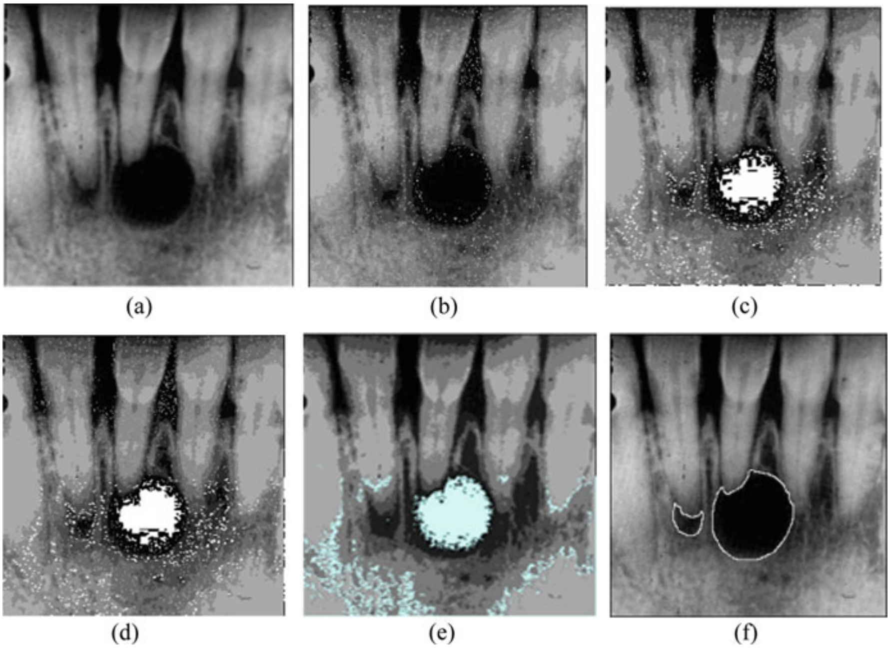

Fig. 2.43 Comparative results of periapical cyst identification. (**a**) Is the original abnormal real jaw's panoramic X-ray images (periapical–lateral and residual cyst), (**b**) segmented result acquired by FCM, (**c**) segmented result acquired by the ABCFCM, (**d**) segmented result acquired by the FAFCM, (**e**) segmented result acquired by the NFCM and (**f**) manual delineation by Oral Pathologist, respectively [32]

The findings of this paper is that eSFCM–Otsu has better performance than the relevant methods such as fuzzy C-means, Otsu, and other semi-supervised fuzzy clustering algorithms, namely SSSFC and SSFCMBP for dental X-ray image segmentation problem as shown in experimental results of Fig. 2.44.

2.4 Review Summary

- Many researchers make use of thresholding and morphological operations for feature extraction and segmentation. However efficient operations are still not included in the existing software majorly used by dental practitioners. Hence, the effective benefits of these methods are still not available to the end users.
- Some of the works have been reported for human identification, but very few researchers have applied and realised the methods for diagnostic purposes.
- Geometrical features for measurements like area, length and angle are not detected by all software even though they are considered the basic features specially for the diagnosis of intra oral diseases.

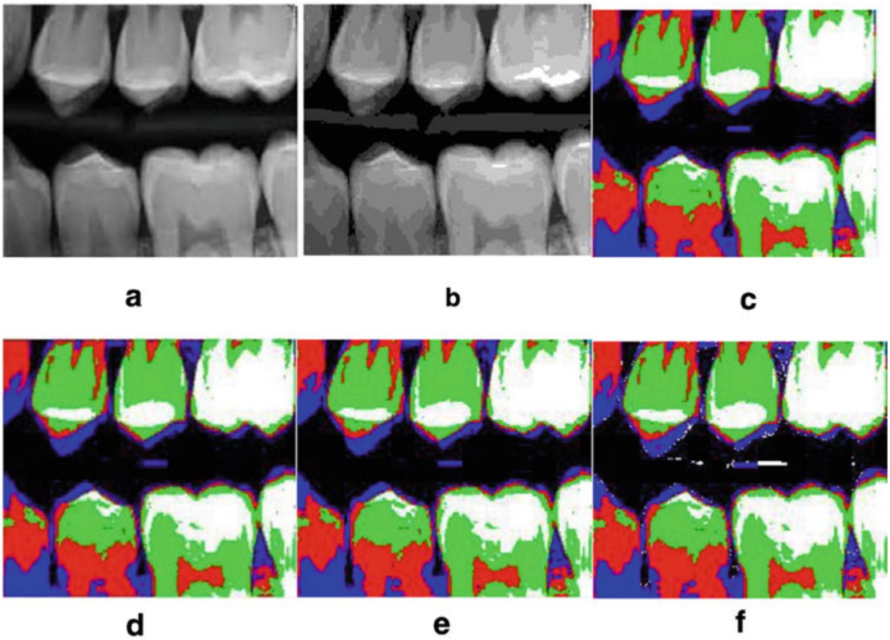

Fig. 2.44 Experimental results on various clustering methods. (**a**) Original image; (**b**) after taking Otsu; (**c**) results of clustering by FCM; (**d**) clustering by SSSFC; (**e**) clustering by eSFCM–Otsu; and (**f**) clustering by SSFCMBP [33]

- Interactive portions of X-ray selected for further processing specifically for the purpose of diagnosis is the need of the hour as it would help both doctor and patient to understand the problem and depth of disease.
- No software exploits the power of AI tools and techniques such as neural network and fuzzy C-means. The usage of such methods may help better in identifications and diagnosis of dental cavities.
- Exploration, development and use of different automated and semi-automated methods for the analysis of dental radiographs may lead to progress in the knowledge and usage of more such methods that can be used for identifications and diagnosis of some of dental diseases are discussed in Sect. 2.1. The overall contribution of this thesis attempts to make progress on these objectives which may finally contribute as an add-on help to dental practitioners and patients at large.

Chapter 3
Enhancement and Segmentation of Dental Radiographs Using Morphological Operations

3.1 Introduction

Digital image enhancement provides a vast array of choices for improving the visual quality of diagnostic images. The appropriate choice of such techniques has a great impact on imaging modality, task at hand and viewing condition. In clinical diagnosis, such techniques include image enhancement and analysis along with visualisation. In response to unique demands in medical/dental imaging, several innovative imaging methods have been, and are being developed for the first time. The adoption and innovation of these processes constantly offer researchers and medical practitioners a new approach for diagnostic imaging.

3.2 Image Enhancement and Segmentation of Dental Radiograph Using Morphological Operations

3.2.1 Image Acquisition

As a part of this research work, a total of 484 dental X-ray are collected by the courtesy of Dr Ronak Panchal. The database so provided is confidential and presented only after obtaining prior permission from doctors and patients.

Figure 3.1 shows some of the dental radiographs from the database provided by the dentist. On these databases various image preprocessing and postprocessing steps have been applied.

K. R. Jain, N. C. Chauhan, *Dental Image Analysis for Disease Diagnosis*,
https://doi.org/10.1007/978-3-030-14136-3_3

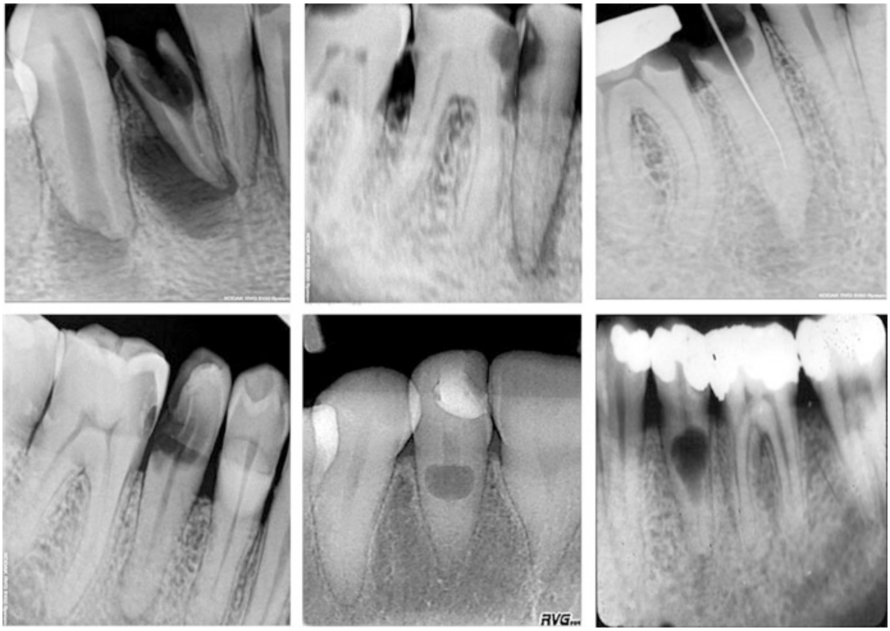

Fig. 3.1 Sample dental radiographs {Courtesy: Dr. Ronak Panchal}

3.2.2 *Preprocessing and Noise Removal*

3.2.2.1 Image Enhancement

Medical images are often deteriorated by noise due to various sources of interference and other phenomena that affect the measurement processes in imaging and data acquisition systems. The nature of the physiological system under investigation and the procedures used in imaging also diminish the contrast and the visibility of details. In all of the cases just mentioned, some improvement in the appearance and visual quality of the images, even if only subjective, may assist in their interpretation by a medical specialist. Image enhancement techniques are mathematical techniques that are aimed at realising improvement in the quality of a given image [35].

Greyscale Clipping

Greyscale clipping is a particular useful case of contrast enhancement, obtained from the general form of the piecewise linear greyscale transformation is described as in Eq. (3.1).

$$v = f(u) = \begin{cases} u \cdot tg\alpha, & 0 \le u \le a \\ (u-a) \cdot tg\beta + v_a & a \le u \le b \\ (u-b) \cdot tg\gamma + v_b & b \le u \le L_{\max} \end{cases} \tag{3.1}$$

The parameters a and b of the function are obtained by examining the linear histogram of the image. The parameters α, β and γ determine the contrast enhancement degree [36]. The input variable u is the grey level of the pixels in the input image U, whereas the output variable v is the corresponding grey level of a pixel in the processed (output) image V. For the parameters $\alpha = \gamma = 0$ the Equation becomes as follows:

$$v = f(u) = \begin{cases} 0, & 0 \le u \le a \\ u \cdot tg\alpha & a \le u \le b \\ L_{\max} & b \le u \le L_{\max} \end{cases} \tag{3.2}$$

Greyscale thresholding (also called image thresholding or Image Binarization) is a particular case of greyscale clipping, obtained when $a = b = t$, for t—a parameter called threshold, whose result is a binary image (having only two grey levels).

Histogram Equalisation Histogram equalisation is a method in image processing of contrast adjustment using the image's histogram. It increases the global contrast of many images, especially when the usable data of the image is represented by close contrast values. Through this adjustment, the intensities can be better distributed on the histogram. This allows for areas of lower local contrast to gain a higher contrast. Histogram equalisation accomplishes this by effectively spreading out the most frequent intensity values [37]. In Fig. 3.2 we can see an image and its histogram. The histogram shows us that the image contains only a fraction of the total range of grey levels. In this case there are 256 grey levels and the image has intensity values ranging from approximately 100–225 only. Therefore, this image is very light.

Adaptive Histogram Equalisation (AHE) It differs from ordinary histogram equalisation in the respect that the adaptive method computes several histograms, each corresponding to a distinct section of the image, and uses them to redistribute the lightness values of the image [38].

The below shown Figs. 3.3, 3.4, 3.5, 3.6, 3.7, 3.8, 3.9, 3.10, 3.11, and 3.12 describe the results of image enhancement of idiopathic resorption, abscess, cyst and endodontic treatment cases using three different methods—greyscale clipping, histogram equalisation and adaptive histogram equalisation. The method of greyscale clipping use various threshold values from 90 to 210.

The resultant images after applying various image enhancement methods can be evaluated and compared with reference to different metrics. In this work we use two metrics, namely mean squared error (MSE) and peak signal-to-noise ratio (PSNR) to evaluate and compare which enhancements are better for the task. These measures are explained further as below.

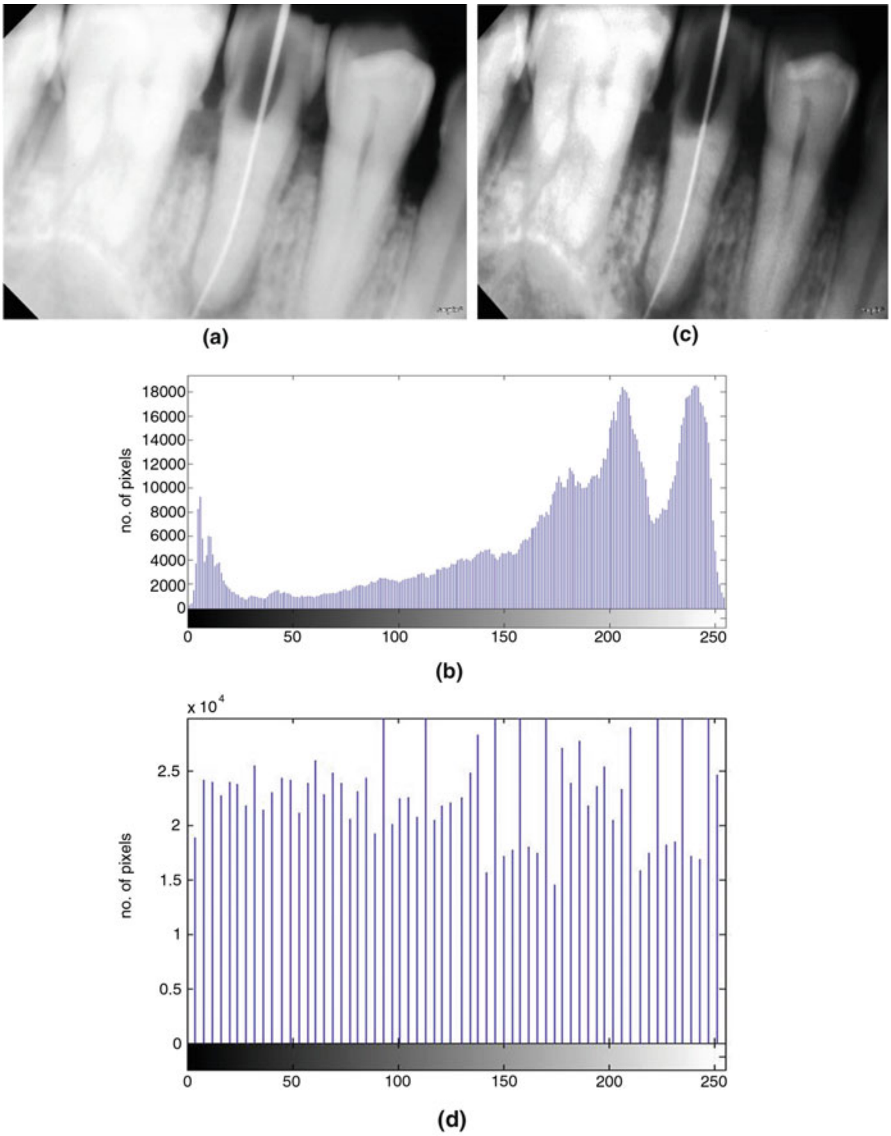

Fig. 3.2 Image enhancement using histogram equalisation. (**a**) Original image. (**b**) Histogram of original image. (**c**) Histogram equalised image. (**d**) Histogram of equalised image

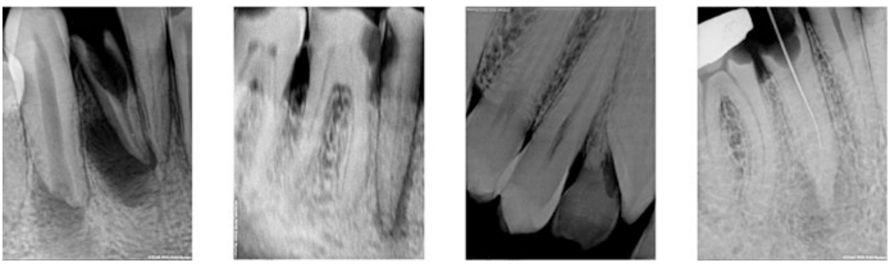

Fig. 3.3 Original radiograph samples

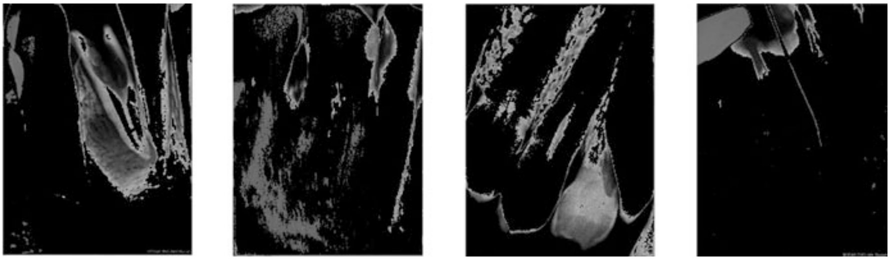

Fig. 3.4 Greyscale clipping of radiographs with threshold value as 90

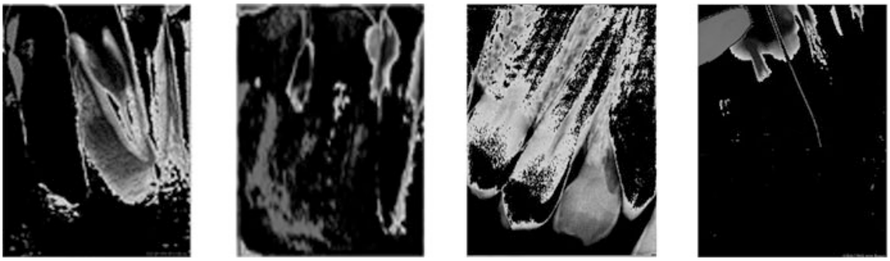

Fig. 3.5 Greyscale clipping of radiographs with threshold value as 110

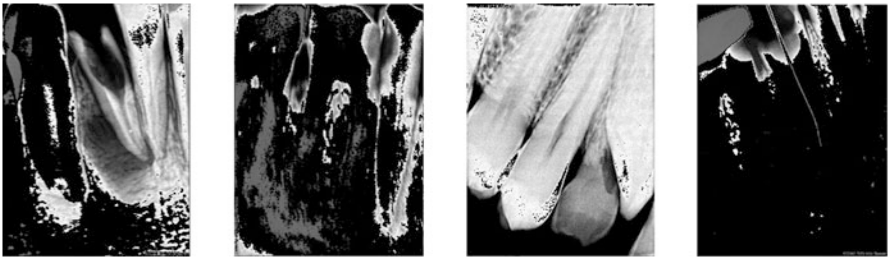

Fig. 3.6 Greyscale clipping of radiographs with threshold value as 130

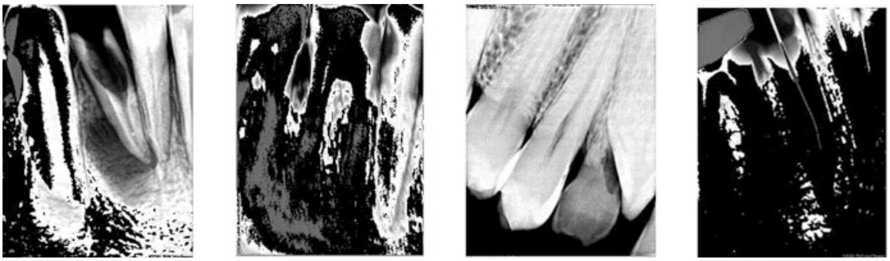

Fig. 3.7 Greyscale clipping of radiographs with threshold value as 150

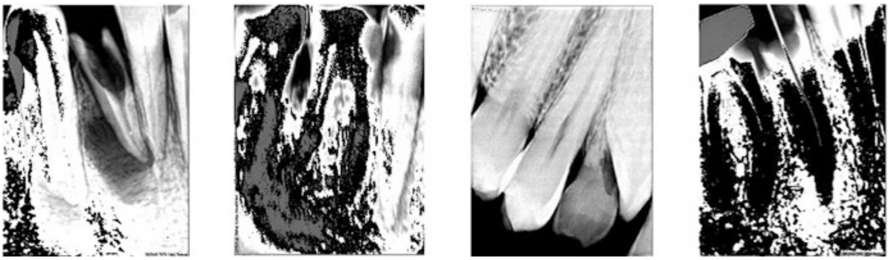

Fig. 3.8 Greyscale clipping of radiographs with threshold value as 170

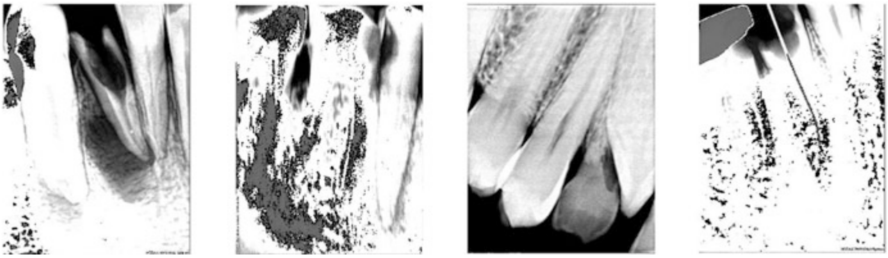

Fig. 3.9 Greyscale clipping of radiographs with threshold value as 190

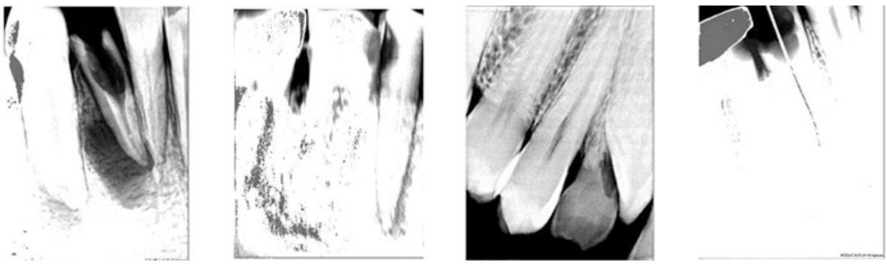

Fig. 3.10 Greyscale clipping of radiographs with threshold value as 210

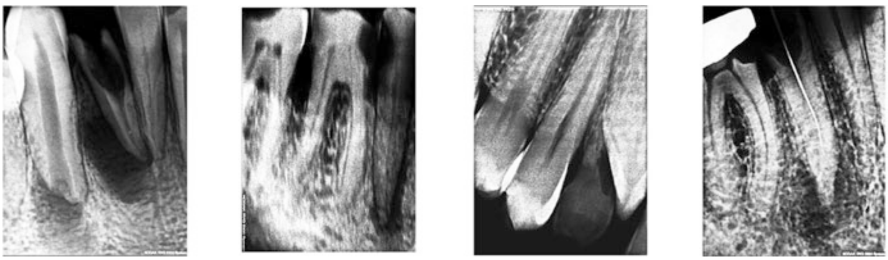

Fig. 3.11 Histogram equalised radiographs

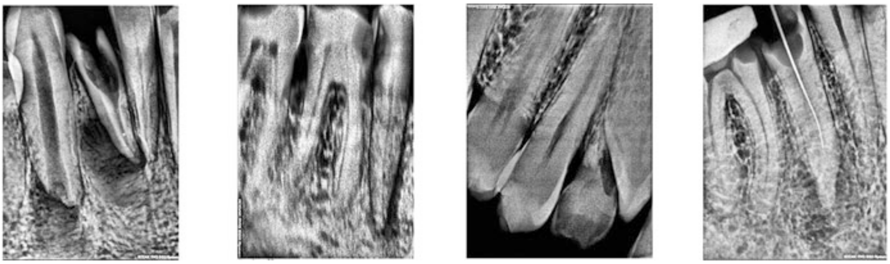

Fig. 3.12 Adaptive histogram equalisation on radiographs

In statistics, the mean squared error (MSE) of an estimator measures the average of the squares of the "*errors*", that is, the difference between the estimator and what is estimated.

$$\mathrm{MSE} = \frac{1}{M^{*}N}\sum_{i=0}^{M-1}\sum_{j=0}^{N-1}\left(f(i,j) - g(i,j)\right)^{2} \tag{3.3}$$

Here, f and g are matrices that represent the images being compared. The two summations are performed for the dimensions "i" and "j." Therefore, $f\,(i,\,j)$ represents the value of pixel $(i,\,j)$ of image f.

The most commonly used image similarity index measure is peak signal-to-noise ratio (PSNR) for two images where one is original and the other is resultant image that can be calculated using the Eq. (3.4). It gives the measure of invisibility of caries in the original signal. The PSNR is defined as:

$$\mathrm{PSNR} = 10^{*}\log_{10}\left(\frac{\mathrm{MAX}^{2}}{\mathrm{MSE}}\right) \tag{3.4}$$

Here, MAX is the maximum possible pixel value of the image. When the pixels are represented using 8 bits per sample, this is 255.

$$\mathrm{PSNR} = 10^{*}\log_{10}\left(\frac{255^{*}255}{\mathrm{MSE}}\right) \tag{3.5}$$

Figures 3.13 and 3.14 represent the bar graphs of MSE and PSNR values respectively after applying all three image enhancement techniques for 14 sample radiograph images of the data set. These graphs suggest that in most of the images adaptive histogram equalisation provides lower and higher values of MSE and PSNR respectively as compared to other enhancement techniques in the case of digital dental radiographs. These enhanced dental radiographs are further segmented using morphological operations.

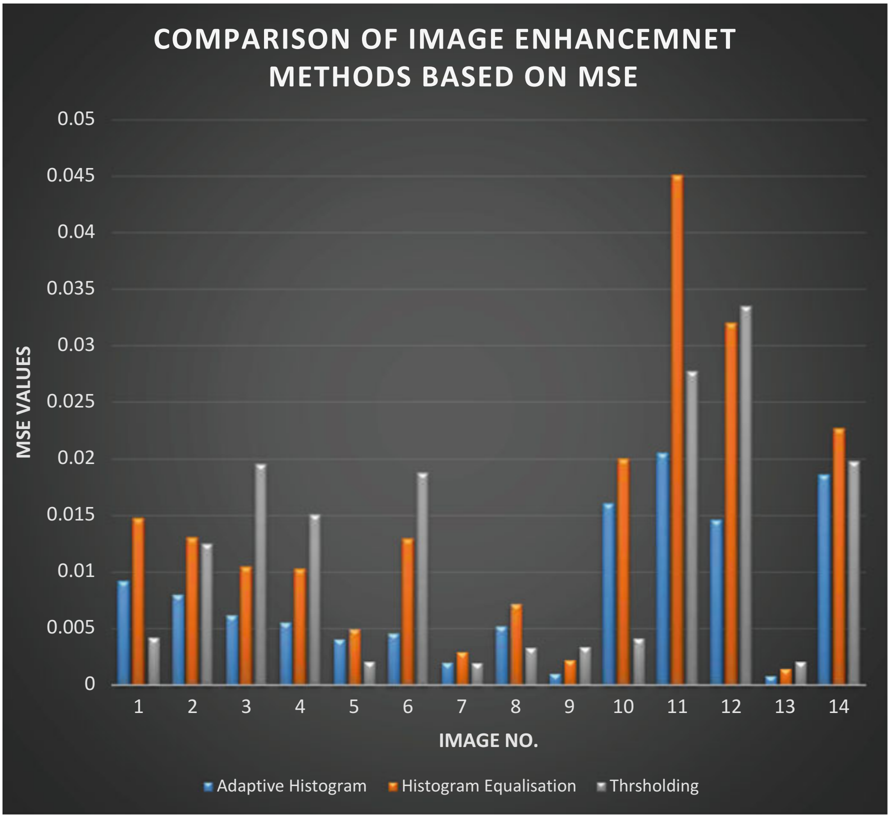

Fig. 3.13 MSE based comparison of image enhancement methods

3.2.2.2 Image Segmentation

Separation of structures of interest from the background and from each other, is an essential analysis function for which numerous algorithms have been developed in the field of image processing. In medical imaging, automated delineation of different image components is used for analysing anatomical structure, tissue types, cavity and pathological regions.

Morphological Operations

Mathematical morphology is one of the tools for extracting image components useful in the representation and description of region shape, such as boundaries, skeletons and convex hulls [39] (Fig. 3.15).

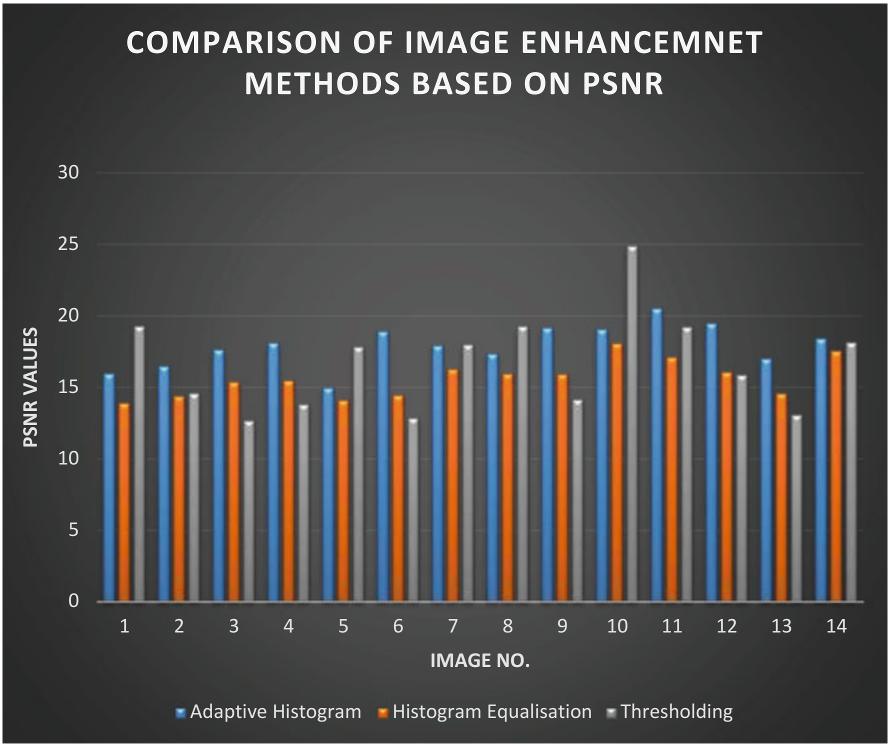

Fig. 3.14 PSNR based comparison of image enhancement methods

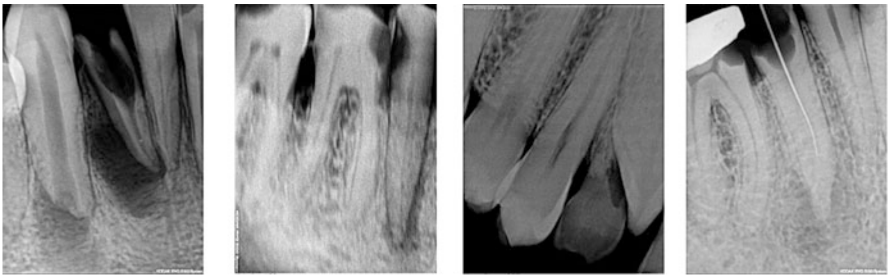

Fig. 3.15 Original radiograph samples

Erosion is an operator that works on a binary image to erode away the boundaries of foreground pixels (usually the white pixels). Thus areas of foreground pixels shrink in size, and "*holes*" within those areas become larger [40] as shown in Figs. 3.16 and 3.17.

Dilation on binary images is to enlarge the areas of foreground pixels (i.e. white pixels) at their borders. The areas of foreground pixels thus grow in size, while the background "*holes*" within them shrink as shown in Figs. 3.18 and 3.19.

Fig. 3.16 Radiograph samples after applying erosion

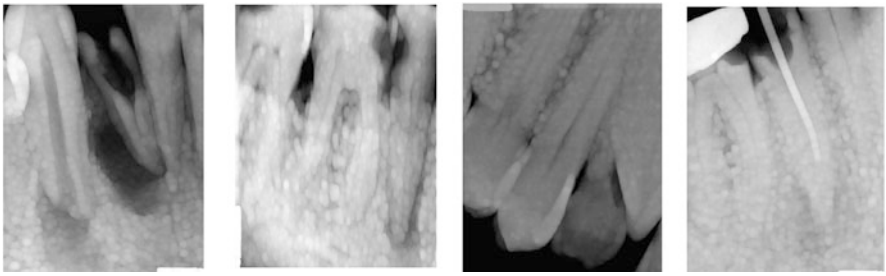

Fig. 3.17 Radiograph samples after applying opening

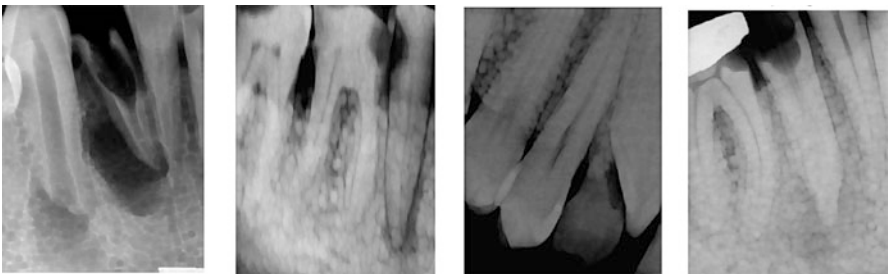

Fig. 3.18 Radiograph samples after applying dialation

Fig. 3.19 Radiograph samples after applying closing

Generalisation to Greyscale Images

The ideas above can be extended to greyscale images as well. In greyscale images, each pixel can have the value in a certain range (i.e. 0–255), with 0 representing black and 255 representing white.

Top-Hat and Bottom-Hat Transformations

Combining image subtraction with opening and closings results in top-hat and bottom-hat transformations. The *Top-Hat Transform* or peak detector is another composite operation: in which the image opened by the structuring element is subtracted from the original image.

The brightest spots on the original image are highlighted using this transformation. In mathematical morphology and digital image processing, *top-hat transform* is an operation that extracts small elements and details from given images. It is defined as shown in Eq. 3.6.

$$T_{\text{hat}}(f) = f - (f \circ b) \tag{3.6}$$

Reverse is the case for bottom hat transform where the dark spots on the original image are highlighted. It extracts large elements and major details from the given image. It is defined as shown in Eq. 3.7

$$B_{\text{hat}}(f) = (f \bullet b) - f \tag{3.7}$$

where f represents the image. The size, or width, of the elements that are extracted by the top-hat and bottom-hat transforms can be controlled by the choice of the structuring element b. An important use of top-hat bottom-hat transformation is in correcting the effects of non-uniform illumination [41] as illustrated in Fig. 3.20.

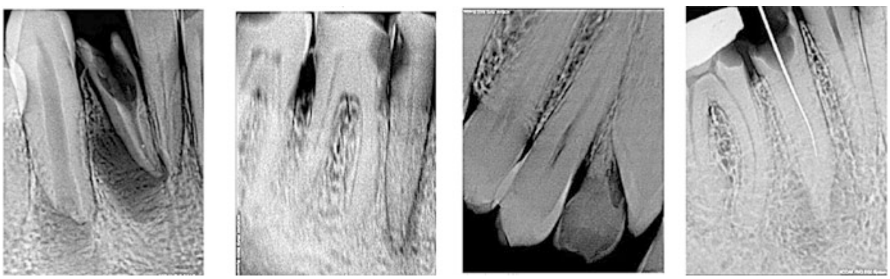

Fig. 3.20 Radiograph samples after applying top and bottom hat transform

3.2.2.3 Noise Removal

The image may be corrupted by random variations in intensity, variations in illumination, or poor contrast that must be dealt with in the early stages of vision processing. Some common types of noise which often corrupts by random variations in intensity values are *salt and pepper* noise, *impulse* noise and *Gaussian* noise.

Median Filter

The main problem with local averaging operations is that they tend to blur sharp discontinuities in intensity values in an image. An alternative approach is to replace each pixel value with the median of the grey values in the local neighbourhood. Filters using this technique are called *median filters* [42] as shown in Fig. 3.21.

3.2.3 Edge Detection

Edge detection refers to the process of identifying and locating sharp discontinuities in an image. The discontinuities are abrupt changes in pixel intensity which characterise boundaries of objects in a scene. Classical methods of edge detection involve convolving the image with an operator (a 2D filter), which is constructed to be sensitive to large gradients in the image while returning values of zero in uniform regions. There are many ways to perform edge detection. One of them which is commonly used is canny edge detection as shown in Fig. 3.22.

3.3 Proposed Method of Detection of Dental Caries

Images contain the greatest density of natural information of all ways of human communication and medical (dental) images are not exceptions of this assertion, at least when such information is dealt with morphological operations. The recent

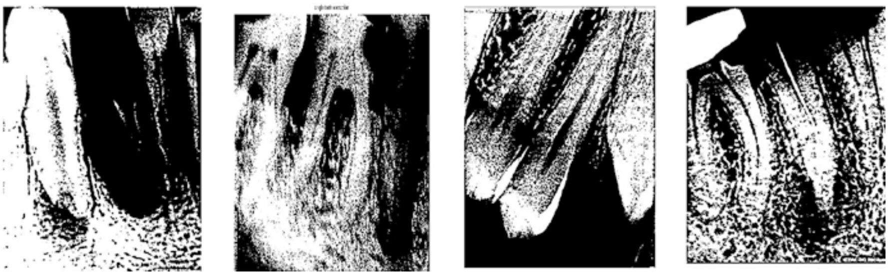

Fig. 3.21 Radiograph samples after applying median filetring

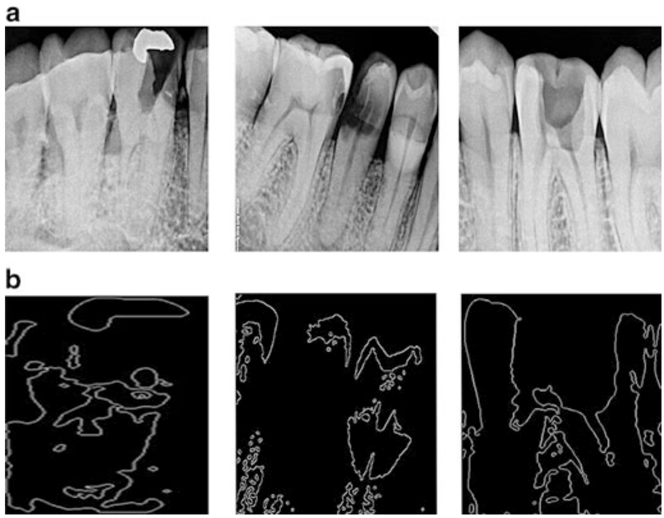

Fig. 3.22 (**a**) Original radiograph samples. (**b**) Radiograph samples after applying Canny edge detection

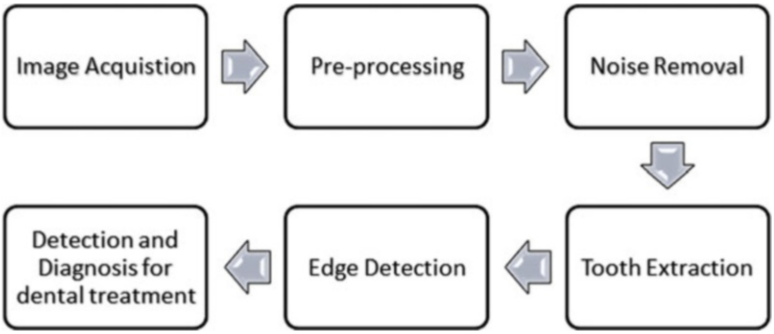

Fig. 3.23 Block diagram of the proposed method

advances in medical imaging have revolutionised the diagnostic accuracy of medical images. Based on the state of the review, the basic image processing techniques are helpful up to some extent in enhancing the dental radiograph for identification of dental caries. In our proposed work steps as shown in the generalised block diagram of Fig. 3.23 are followed. The steps of the proposed method for detection of dental caries using enhancement and morphological operations is shown in Algorithm 3.1.

Algorithm 3.1 Enhancement and Segmentation of Dental Radiograph Using Morphological Operations

Steps:

1. *Acquisition of dental radiograph comprising caries.*
2. *Apply adaptive histogram equalisation on the acquired dental radiograph.*
3. *On the histogram equalised image apply median filtering to remove the noise.*
4. *With the help of top-hat and bottom-hat transform segment the acquired radiograph.*
5. *Canny edge detection is applied on the segmented ROI.*
6. *Apply hysteresis operation on ROI and compare it with the original radiograph being provided by the practitioner for identification of affected caries area.*

3.4 Experiment and Results

Based on the edge detection we would be able to locate the caries or decay in the tooth. Figure 3.24 provides such information that would help medical practitioners to identify the region of interest for identification of various dental diseases. In the case of endodontic treatment or filling such information would be quite beneficial to make decisions for the medical practitioners. Figure 3.24a1–a15 represents the original radiographs from the dataset as provided by the practitioners (as shown in Table 1.1) for further processing. The second and third columns represent the resultant radiographs after canny edge detection and hysteresis operation on affected portions of radiographs as shown in Fig. 3.24b1–b15 and c1–c15, respectively. The practitioners may further proceed with treatment based on the identifications suggested. This is finalised by comparing the results of edge detections with that of ground truth images. The final identifications (treatment) considered/carried out (either filling or root canal treatment) by the practitioner for all of the images shown in Fig. 3.24 are mentioned in the last column.

3.5 Evaluation Measurements for Prediction of Endodontic Treatment Using the Proposed Approach

In this section, we focus on identifying performance of morphological operations in the prediction of the endodontic treatment. The evaluation measurements include accuracy (recognition rate), sensitivity (recall), specificity and precision. In order to perform evaluation of results using these metrics, the ground truth images are required. These ground truth images are obtained again with the help of dental practitioners. All dental radiographs obtained were marked by dental practitioners which then served as ground truth for our datasets.

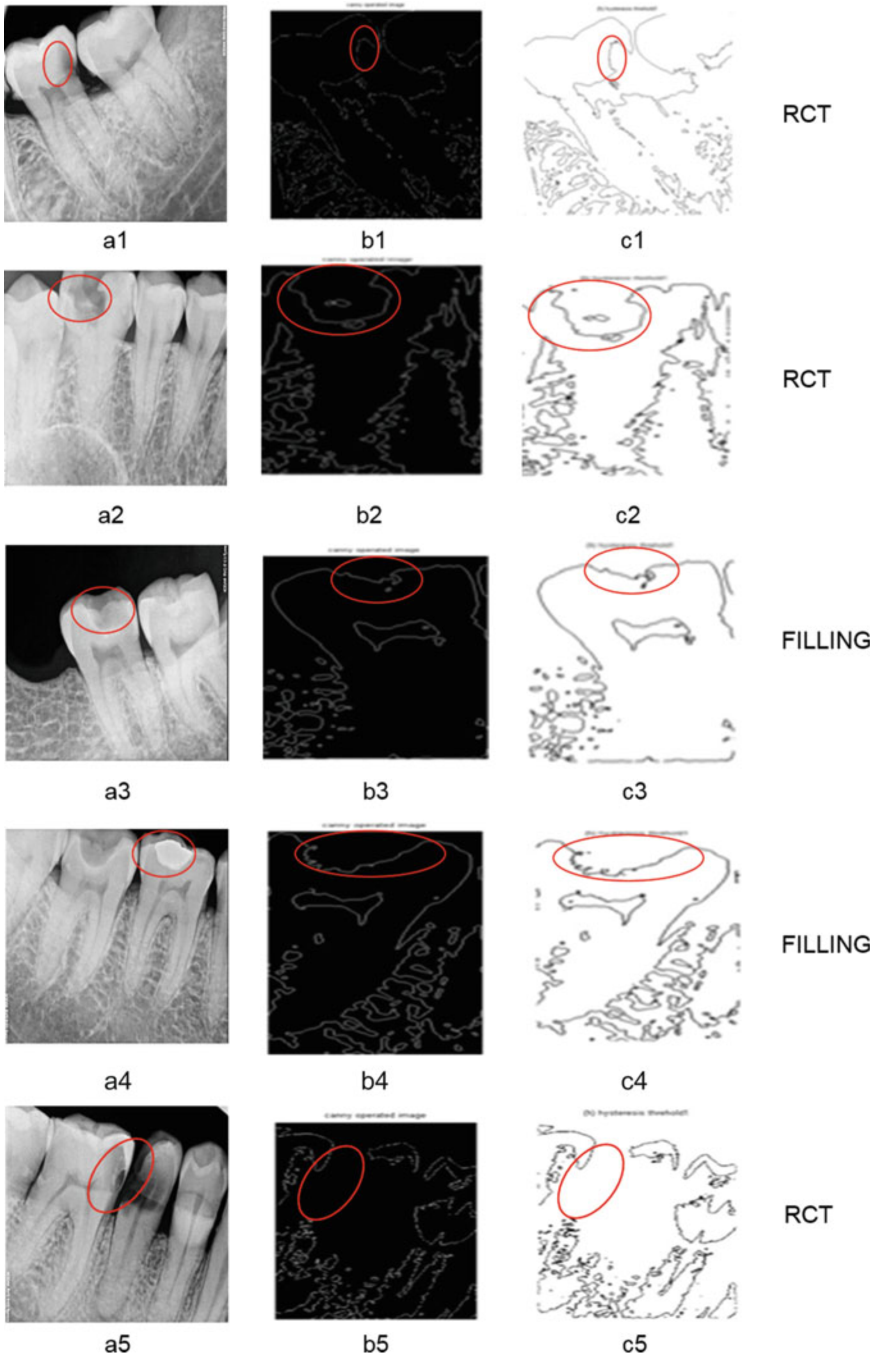

Fig. 3.24 Results of various detected dental caries obtained through edge detection

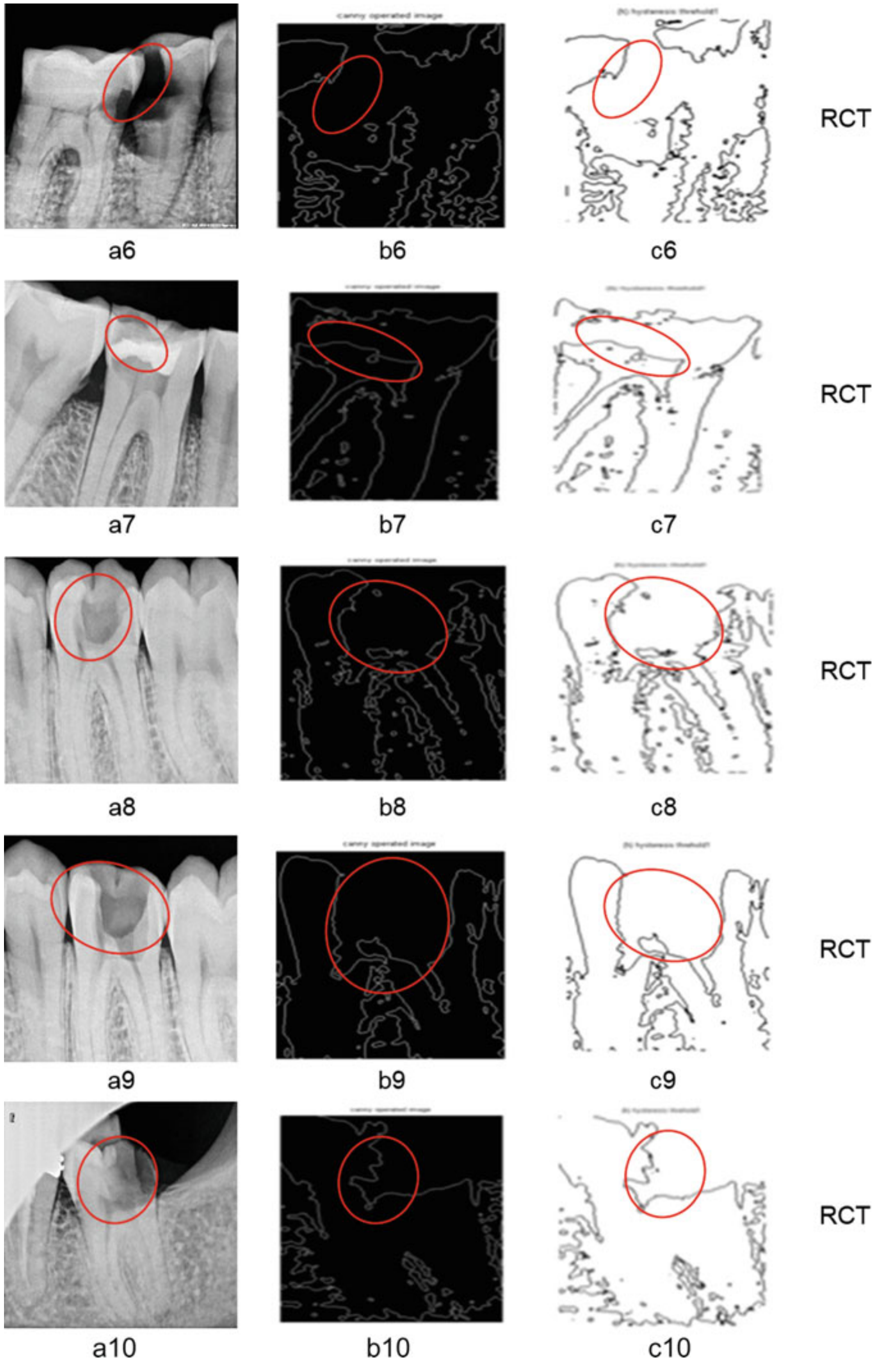

Fig. 3.24 (continued)

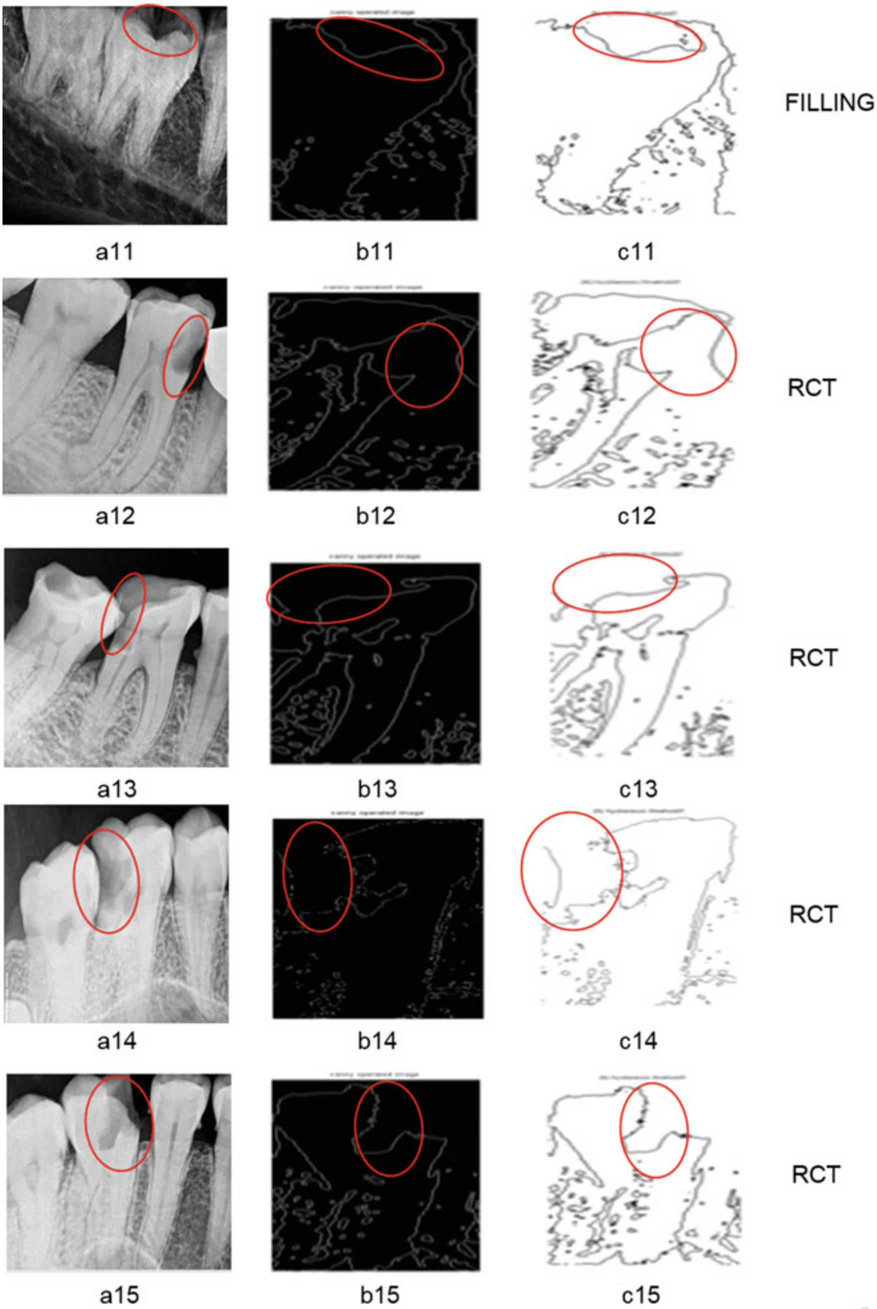

Fig. 3.24 (continued)

As shown in Fig. 3.24, the first column contains images in which ROI is marked (red circles) by expert, that is, the ROI is selected by dentist in red boundaries. The second and third columns represent the results of segmentation through edge detection methods. The red boundaries in these images are the caries which are marked manually. In order to measure the performance of the method, we describe few terminologies like positive region (pixels of the main class of interest) and negative region (region of image except positive region). More specifically, the positive region means the ROI according to domain expert (dentist) in our radiographic image and false region means the areas excluding ROI. Let P be the number of pixels in positive region and N be the number of pixels in negative region. For each region, we compare the identified class label with the region's known class label. The four important terminologies used in the whole process of measurement are as follows.

True Positive (TP) refer to the positive region(s) that was/were correctly labelled by the classifier.

True Negative (TN) refer to the negative region(s) that was/were correctly labelled by the classifier.

False Positive (FP) refer to the negative region(s) that was/were incorrectly labeled by the classifier as positive region(s).

False Negative (FN) refer to the positive region(s) that were incorrectly labelled by the classifier as negative region(s).

The above terms [43] are summarised in a confusion matrix as shown in Table 3.1 where the predicted class means the segmented region(s) of affected tooth based on the proposed algorithm and the actual class means the ROI as indicated by the expert.

Based on the terms mentioned in confusion matrix, three performance evaluation measures—accuracy, error rate and specificity—are defined as follows.

Accuracy (A) On a given data set it is defined as the percentage of test pixels/regions that are correctly classified by the classifier. It is given by the following formula:

$$\text{accuracy} = \frac{\text{TP} + \text{TN}}{P + N} \tag{3.8}$$

Error Rate (ER) On a given data set it is defined as $1 - \text{Accuracy}$. It is given by the formula in Eq. 3.9.

$$\text{error rate} = \frac{\text{FP} + \text{FN}}{P + N} \tag{3.9}$$

Table 3.1 Confusion matrix

Predicted class				
Actual class		Yes	No	Total
	Yes	TP	FN	P
	No	FP	TN	N
	Total	P'	N'	$P + N$

Precision (PR) On a given data it refers to as true positive pixels/regions that are identified by exactness.

$$\text{precision} = \frac{\text{TP}}{\text{TP} + \text{FP}} \tag{3.10}$$

Specificity (S) On a given data set it is defined as the true negative pixels/regions that are correctly identified. It is given by the following formula in Eq. 3.11.

$$\text{specificity} = \frac{\text{TN}}{N} \tag{3.11}$$

Based on the above defined parameters, the confusion matrix for one of the radiographic images and its comparison with one ground truth image is shown in Table 3.2.

According to this confusion matrix the accuracy of our segmented result is 81.36%, error rate is 18.63%, precision is 8.23% and specificity is 92.38%. Such confusion matrix and all four measures are computed on a total of 484 images in the dataset. The values of the measures for first 15 images, and the overall average value of the measures for all the images are shown in Table 3.3.

Table 3.2 Confusion matrix of a sample image as compared with ground truth

Predicted class				
Actual class		Yes	No	Total
	Yes	491	9834	10,325
	No	5468	66,306	71,774
	Total	5959	76,140	82,099

Table 3.3 Evaluation measures for segmented images in the dataset

Images	Accuracy	Precision	Error rate	Specificity
1	81.36	8.23	18.63	92.38
2	79.83	16.32	20.16	87.45
3	80.61	6.79	19.38	89.05
4	75.13	10.31	24.86	86.48
5	80.44	20.05	19.55	89.42
6	83.38	28.17	16.61	96.32
7	74.45	6.13	25.54	84.58
8	71.42	6.00	28.57	82.18
9	69.24	15.29	30.75	81.90
10	74.50	6.55	25.49	83.80
11	73.49	1.03	26.50	89.17
12	72.88	5.78	27.11	82.55
13	72.74	19.79	27.25	84.70
14	79.85	8.10	20.14	85.58
15	77.04	16.63	22.95	84.96
Avg. 484 images	79.37	32.87	20.62	90.15

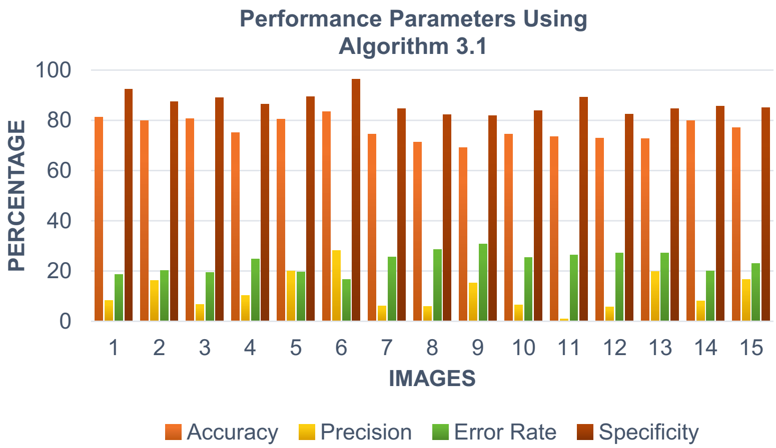

Fig. 3.25 Parametric evaluation measures based on Algorithm 3.1

Hence, now with the help of results of performance measures, it can be depicted that the suggested approach is quite helpful for the segmentation and analysis of dental radiograph images during the process of endodontic treatment. The results produced by the suggested method were further verified with the same practitioners who contributed for the dataset, and as per their feedback the results can help the practitioners in their work. A bar chart of the results shown in Table 3.3 is also plotted in Fig. 3.25. Average accuracy of 484 data base images is found to be 79.37% with a precision of 32.87%, error rate of 20.62% and specificity of 90.15%.

3.6 Result and Discussion

This chapter demonstrates user of basic morphological operations and edge detection methods for preprocessing and segmentation of dental radiographs. The results produced are compared with a set of ground truth images. The technique used was quite basic in nature. However, the results are quite clear but also have many pitfalls. The process carried out was manual in nature, and the grey level clipping varied from image to image. Moreover, the cropping being done to extract the tooth was manual in nature and later comparison with the ground tooth to finalise under which case the cyst falls was also manual. The methods shown in this chapter does not claim to be final tool. However, the identifications from the methods may be correlated with the clinical findings of the practitioners in order to proceed to further treatment.

Chapter 4
Segmentation of Dental Radiographs Using Active Contour Model

4.1 Introduction

The fundamental task in the case of medical images is detection of interested region (s) and their further investigations either in automated fashion or through expert interventions. The presence of noise and image anomalies lead to imperfection in boundary detection as it depends on intensity and contrast. The limitation of the tools/techniques is noticed when the medical practitioners based on his/her expertise confirm that the boundaries found by the edge detection algorithm in the tool are not clear and they do not discretise the regions properly. So proper image segmentation for extraction of features is essential [44]. To forfeit the above conditions partitioning of an image into subsections must satisfy certain conditions. These are considered segmentation properties.

Segmentation of a grid X into subsets X_1, X_2, X_3, …, X_N must satisfy the following conditions, where $P(R_i)$ is a uniformity predicate for all elements in set R:

$$\left.\begin{array}{ll} 1) & U_{i=1}^{n} X_i = X \\ 2) & \text{For } i \text{ and } j, \text{if } i \neq j, X_i \cap X_j = \phi \\ 3) & P(X_i) = \text{TRUE for all } i \\ 4) & P(X_i \cup X_j) = \text{FALSE if } i \neq j \end{array}\right\} \tag{4.1}$$

The first condition explained in Eq. 4.1 suggests that all sub-segments of an image combine to form the original image. Secondly all sub-segments are from the same set of matrix and union combines to form the original one. Thirdly the sub-images or segment so formed have same characteristics/properties within each. Lastly no two sub-images or sub-segments have identical properties outside their segment. The process of image segmentation can be broadly divided in two categories namely edge and region based [45]. On the basis of discontinuities with sub-regions image is portioned using edge-based segmentation technique.

K. R. Jain, N. C. Chauhan, *Dental Image Analysis for Disease Diagnosis*,
https://doi.org/10.1007/978-3-030-14136-3_4

4.1.1 Edge-Based Segmentation

Discontinuities in the intensity of an image leads to edge-based segmentation. In broader sense it is more deviated aspect of boundary detection rather than the main motive of segmentation. The concept lies in separation of regions within an image based on uniformity with in individual sub-regions. The sub-region uniformity is purely based on computation of a local derivation operator. Edge-based portions work perfectly with sharp intensity transition and relative low noise images [46].

The use of local derivation operator for partitioning requires a prerequired noise removal process. It makes the resultant image more vulnerable to use as the blurring effect in the images leads to smoothening. This smoothening leads further to discontinuities in edges. The only reason for its popularity is the computational cost and time, which is too less as compared to others.

4.1.2 Region-Based Segmentation

The uniformity in any sub-region of an image can be identified based on intensity, colour and texture. Such uniformity can play important role in classification or clustering. Region growing in another way is to converge the alike pixels or small portions of a sub-image to a larger one. The best compliment for such an approval is pixel aggregation, which starts with a user defined set of seed points and grow regions from them by adjoining nearby pixels which satisfy the user criteria [47].

However, region growing involves some major pitfalls like selection of initial seeds and suitable properties to grow the region. Another technique namely region competition has emerged up. It combines the neighbouring sub-regions under the condition of equality of regions or sharpness of boundaries [48]. Bounding more parameters for perfection of sub-regions leads to oversegmented results and lean boundary condition led to poor segmentation resulting in cover merging the sub-regions with blurry boundaries. Split and merge though traditional but still satisfies few medical application like CT scan and Brain MRI.

4.1.3 Active Contour

The use of deformable contours has increased its applications to image segmentation and motion tracking commonly known as ACM. In the case of medical images there are certain regions, as suggested by practitioners, with unphysically very large curvatures. Moreover, the boundary so detected may be quite noisy and the preferable edge detected might detect many edges where the practitioners might require a single one to differentiate the ROI [49].

The presence of an edge depends on two things out of which one is local gradient information and other one is long range spatial distribution of the gradient. Active contour incorporates long range view by combining continuity and curvature constraints with local gradient strength. Snakes is considered an elastic curve, which minimises the energy to deform and adjust its initial shape on the basis of addition image information to provide a continue boundary [50]. Minimisation of energy function is a joint venture of external and internal energy. Internal energy keeps the curve together and prevents it from bending too much using elasticity and rigidity. External energy draws the curve towards the desired object boundaries.

4.2 Active Contour Model

In this model, bi-dimensional contours are being used and handled [49].We start with the classic snakes introduced by Kass. The basic mathematical set-up of these curves is illustrated below. To simplify the model we will use the curve parametric model. Let us call γ our contour, where γ can be either open or closed curve.

$$\gamma(s) = \begin{cases} [a,b] \subset \Re \rightarrow \quad \subset \Re^2 \\ s \mapsto \gamma(s) = \left(\gamma_x(s), \gamma_y(s)\right) \end{cases} \tag{4.2}$$

The set-up for our deformable curve allows us to have the two types of curves, that is, open or closed if $\gamma(a) = \gamma(b)$ as shown in Fig. 4.1.

The idea is to create a curve whose behaviour is driven by two aspects of active contour. The first aspect is to perform partitioning of the image based on object and shape detection. The second aspect lies on the model of the contour we want to have.

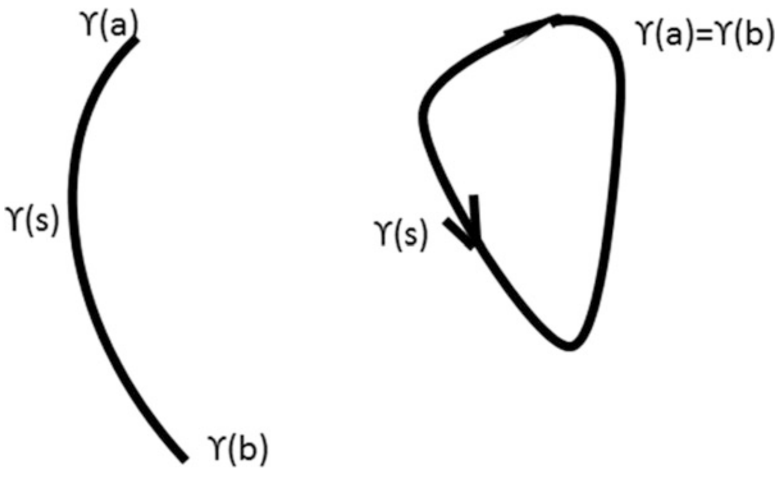

Fig. 4.1 Open and closed contours

Basically this curvature must match the shape curvature. These two aspects are considered the energy function that we are going to present [51].

4.2.1 External Energy

The external energy is the component of the behaviour function that describe how the deformable curve will match with objects of the image. Indeed the external energy is the function that will constrain the contours displacement. To be attracted by a shape, a function is required with the following properties: have at least one local minimum and be monotonic on areas around this point. To have such a function in an image its gradient is used [52]. Indeed, around edges the gradient presents these two characteristics of presenting a local extreme and having a monotonic behaviour. We will enforce this behaviour with a preprocessing consisting in a Gaussian Smoothing of the image to improve this aspect. So the external energy function is expressed as:

$$E_{\text{ext}} = P(\gamma(s)) \tag{4.3}$$

where P stands for a potential attraction field onto the edge of an object. So we have to consider this energy not only locally but for the whole contour C and to plug in the previous equation the properties we mentioned above. If the contour is closed we have:

$$E_{\text{ext}} = \oint_C \|\nabla I\|^2(\gamma(s))ds \tag{4.4}$$

or if we just consider a non-closed contour going from A to B:

$$E_{\text{ext}} = \int_A^B \|\nabla I\|^2(\gamma(s))ds \tag{4.5}$$

where I represents the input image and ∇ is the spatial gradient function defined by:

$$\nabla I = \left(\frac{\partial I}{\partial x}, \frac{\partial I}{\partial y}\right) \tag{4.6}$$

Due to the fact that we want to minimise this energy, we take the opposed value and introduce our Gaussian smoothing to enforce convergence to a local minimum:

$$E_{\text{ext}} = -\int_{A}^{B} \left\|\nabla\left(G_n{}^{*}I\right\|^{2}(\gamma(s))ds \tag{4.7}$$

where G_n is a Gaussian weighted kernel of dimension n. A weighting parameter on the external energy will allow us to increase the "visibility" of the gradient field by the snakes. So it is written as:

$$E_{\text{ext}} = -\delta\int_{A}^{B} \left\|\nabla\left(G_n{}^{*}I\right\|^{2}(\gamma(s))ds \tag{4.8}$$

where δ is a real weighting value which for obvious reason would be positive.

4.2.2 Internal Energy

The internal energy is the component of the behaviour function that describe the physical properties of our contour like smoothness or continuity and curvature [52]. It is composed of two terms, the first one is describing the contour behaviour regarding elasticity or smoothness so it is a function of the first derivative of our contour. The second term is describing the curvature model of the curve and is function of the second derivative of our contour. If we put that into a mathematical form, we have:

$$E_{\text{int}} = f(\gamma'(s)) + g\left(\gamma''(s)\right) \tag{4.9}$$

The functions f and g are just going to be the Euclidean norm of the function. Then we need to specify that we want the energy for the whole curve C so not only for one spatial locations so we are going to sum this energy along the curve, which will lead to two different cases. If our contour is closed:

$$E_{\text{int}} = \oint_{C} \|\gamma'(s)\|^{2} + \left\|\gamma''(s)\right\|^{2} ds \tag{4.10}$$

or if we just consider a non-closed contour going from A to B:

$$E_{\text{int}} = \int_{A}^{B} \|\gamma'(s)\|^{2} + \left\|\gamma''(s)\right\|^{2} ds \tag{4.11}$$

The previous definition is defining a model of smooth curve or function to describe the contour's behaviour, which goes through the use of its derivative and in our case in their minimisation.

$$E_{\text{int}} = \int_A^B \alpha\|\gamma'(s)\|^2 + \beta\left\|\gamma''(s)\right\|^2 ds \tag{4.12}$$

where $(\alpha, \beta) \in R^2$ in a general definition but we will see that there are certain restrictions to their possible values. Indeed a shape with straight and sharp angles requires a lot more internal energy than a more continuous shape.

4.2.3 Contour Global Energy

The final contour energy function is presented as:

$$\begin{aligned} E_{\text{snake}} &= E_{\text{int}} + E_{\text{ext}} \\ &= \int_A^B \alpha\|\gamma'(s)\|^2 + \beta\left\|\gamma''(s)\right\|^2 ds - \delta \int_A^B \left\|\nabla\left(G_n{}^*I\right\|^2(\gamma(s))ds \end{aligned} \tag{4.13}$$

As we said before, this active contour method relies on an energy minimisation technique [53].

4.2.4 Optimisation

Our goal in this section is to find the optimal parameters that will minimise the previous energy function defined earlier. These parameters are position vectors that will define the position of the snake which minimises this energy. Indeed, we are looking for $\gamma(s) = (\gamma x, \gamma y)$ (s) so that E_{snake} is minimal. The optimisation formulation of our problem is then:

$$s_{\text{optimal}} = \underset{\gamma \in F}{\operatorname{argmin}} \; E(\gamma(s)) \tag{4.14}$$

which means that we want to find the value of s which is the argument that makes the curve γ, of the set of possible curve, of minimal value regarding the energy function E.

The gradient descent method is used for finite dimensions. It is a 1st order optimisation technique based on 1st order Taylor series decomposition. This method is relied while we would implement Euler–Lagrange snake method [54].

The general set-up of such an optimisation problem involves small variations modelled using a time evolution variable and the following equation.

$$X^{k+1} = X^k + t^k d^k \tag{4.15}$$

where 't' represents the time step used and 'd' represents the direction in which this time step modification is performed. In gradient descent method decomposition is as follows

$$f\left(X^k + t^k d^k\right) = f\left(X^k\right) + t\nabla X^{KT} d \tag{4.16}$$

Based on the medical problem at hand we need to minimise the energy function in the time evolution. Hence, the final imposed condition on our algorithm would be

$$f\left(X^{K+1}\right) < f\left(X^K\right) \tag{4.17}$$

Therefore, Eq. 4.15 is further modified and the formulate leads to

$$\nabla X^{KT} d < 0 \Rightarrow d = -\nabla X^K \tag{4.18}$$

4.2.5 Gaussian Smoothening

An important part of the set-up to perform a segmentation using active contour is to preprocess the image using a Gaussian filtering [55]. If the input image has a good quality, then its edges are normally well defined. This may find availability of abruptness in the image. This property may play an inverse role in the optimisation algorithm and the snake energy evolution because the external energy relies on the use of the image gradient. In fact, the snake is attracted progressively towards the edge of the object. To do that we need to "spread" the edges around to create a more smoothed gradient around the edge.

Smoothing has an influence on the size of the spread edge and on the value of the local minimum. So one can conclude that the gradient field is directed to the edge rather than going away. Hence, it will attract the snakes. Secondly this gradient field is spread more around the edge to have a wider influence. Finally this spread is dependent on the kernel size and a trade-off with the initialisation distance [56].

When computing the external energy, opposite value of the gradient norm is selected. Indeed, we can see on the image that the gradient norm is increasing while getting closer to the edge as we are interested in minimising the energy. So we need to make it become as low as possible when we get closer.

Another reason of applying a Gaussian filtering is to handle the noise. In fact, it's pretty common to have noisy images, and noise is modifying a lot the external energy of the image.

4.2.6 Kernel Settings

The kernel size and type are really important as we mentioned before because it influences the way the edge is spread around. It has a consequence of simple convolution implementation that reduces the size of the resulting image. This aspect can of course be noticed while looking at the intensity curve of the smoothed image where we can clearly see null areas on the sides of the intensity curve. There is a choice to make in the design of the filtering kernel that is further illustrated with the results.

4.2.7 Contour Construction

As we said before, we are going to rely on the user to define an initial shape around the object that will serve as an initialisation set-up.

4.2.8 Stopping Criterion

In the original method presented by Kass in 1987, there is no indications about a stopping criterion on the snakes model's evolution [49]. When using the greedy method we have two stopping criterion. The first one is whether the number of points that move at each iteration fall under a certain threshold value and the other one is that the number of iterations reaches another threshold value.

4.3 Proposed Approach

The first test was to analyse the working of our contour. We had to see that each point being displaced over time in the way we selected them because we are iterating over points to make them move. To make the test successful and to identify the ROI based on segmentation we tried to match the curve based on edges of the subject. Later we calculated the accuracy of our system by comparing the segmented region so obtained by our proposed approach with ROI of experts. The set-up of α and β coefficient plays an important role in the shape of contour. One important point to be noted is the size of smoothing kernel in relation to the size of minimisation window.

This size of window must be same as that of kernel to produce best results. Another constraint during implementation is to have an initial contour, which is not too far from the ROI. As the distance from ROI increases the convergence is not ensured because the attracting field would not be visible.

The number of points and its distance from each other is quite important while implementing the algorithm and keeping the constraints in the mind. The results were not so much satisfactory. So we wanted to work on a coarser method, where mathematical properties rely much on optimisation. The proposed approach relies on calculus variations and is Euler–Lagrange method. As discussed earlier the initial shape is selected and then the evolution of contour begins. For the sake of ease and increased efficiency in the continuity and smoothness of curve discrete deviation matrices are used. The gradient information is utilised for the purpose of computing external energy. Finally, we iterate until the energy reaches a local minimisation after a certain number of iterations. The steps for the proposed approach are mentioned in Algorithm 4.1 for extracting the cyst:

Algorithm 4.1 Image Segmentation of Dental Radiograph Using Active Contour Model
Steps:

1. Collection of periapical database images comprising of cyst diseases.
2. Fix all the values of parameters as described in snakes model. In this, various parameters $\alpha, \beta, \gamma, W(E_{\text{line}}), W(E_{\text{edge}}), W(E_{\text{term}})$ are utilised for getting the affected area of disease on various database images.
3. Initialise the contour by clicking at a sequence of points close to the object to be segmented, the contour is then defined as the set of consecutive points.
4. Design a stopping criterion for the iterative process.
5. Choose different initialisations for starting contour, also with the different number of control points, and observe the evolution of the deformable contour.

As discussed earlier too that selection of seed points is quite crucial in this proposed process. If the seed points so selected are too far away from the ROI then after iterations the ROI so targeted would not be useful as shown in Fig. 4.2. Moreover, if the seed points are too close to ROI then in that case too, the targeted ROI would not be achieved as shown in Fig. 4.3. In the Fig. 4.2a shown below we take an example of an erythroplakia patient where the ROI is the white patch being developed on the tongue where 4.2b, c represent the seed points and ROI after iterations respectively.

We initialise our model of seed points little bit far away from the targeted test shape. During first iteration the snake moves slowly. Once we get closer to the ROI the magnitude gets large and attracts the snake more strongly which increases the distance between the intermediate contours to finally have enough energy to jump to the boundary of the shape.

As seen in the Fig. 4.4 the iteration of snake and its seed points closely match the ROI. In the latter we found out the edge of the affected part using canny edge detection method. Hence, we measure the area of that part.

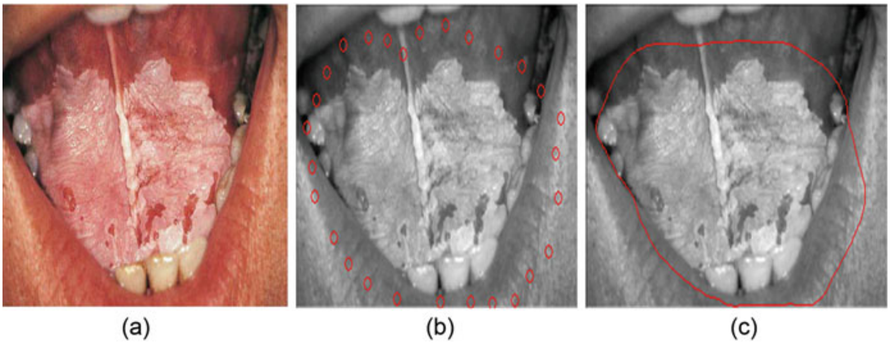

Fig. 4.2 Erythroplakia case with seed points at far off place. (**a**) Original image. (**b**) Seed points at far place. (**c**) ROI after iterations

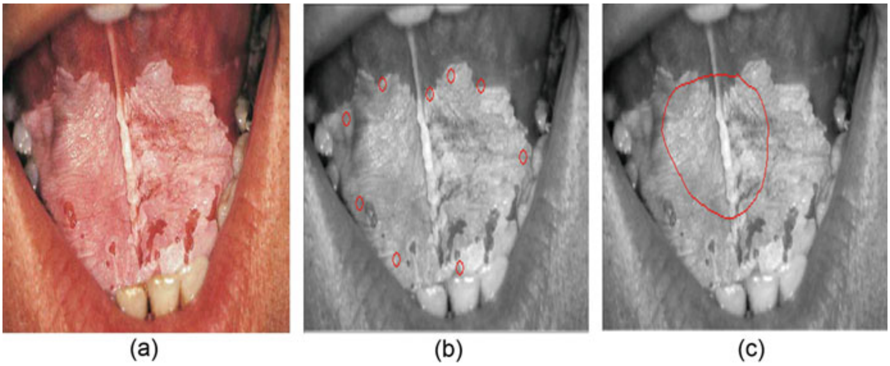

Fig. 4.3 Erythroplakia case with seed points on ROI. (**a**) Original image. (**b**) Seed points on ROI. (**c**) ROI after iterations

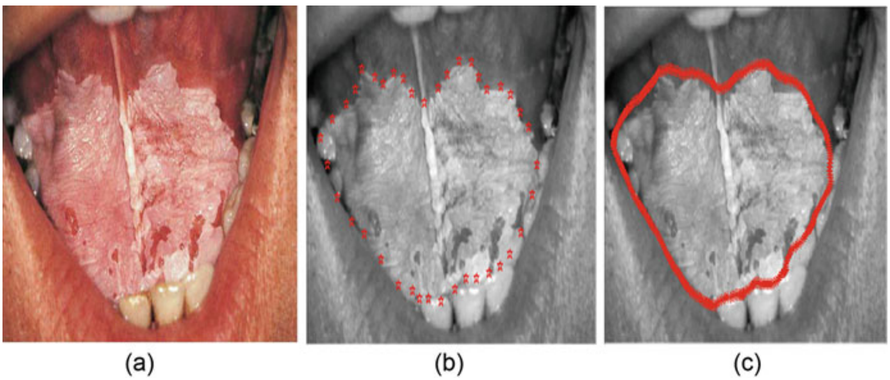

Fig. 4.4 Erythroplakia case with seed points near to ROI. (**a**) Original image. (**b**) Seed points near to ROI. (**c**) ROI after iterations

4.4 Experiment and Results

As discussed in step 2 of the Algorithm 4.1 various parameters have their own significance. The value of α denotes smaller distances between points. If we choose value of α as high, then the distance between points is minimised. β denotes the angle between the points. If we choose the value of β as higher, then the angle between edges are minimised. So from that we get smooth edge. γ indicate intensity of images. If we choose the value of γ is high, then contrast between background and feature is low. To extract the affected area of disease from the original image, we choose value of α, β and γ by trial–error method. After getting proper value of α, β, γ, $W(E_{\text{line}})$, $W(E_{\text{edge}})$, $W(E_{\text{term}})$ using trial–error method, we take the same value of this parameters for applying various database images for getting proper contour of affected area of the diseases.

$W(E_{\text{line}})$ denotes weighting factor for intensity based potential term. $W(E_{\text{edge}})$ denotes weighting factor for edge based potential term. $W(E_{\text{term}})$ denotes the weighting factor for termination-based potential term (Table 4.1).

With these values as constant snakes model for identification of abscess, cyst, idiopathic resorption, erythroplakia and leucoplakia was designed and implemented. A total of 244 jpeg images of erythroplakia and leucoplakia patients along with 372 RVG images of dental implants, abscess, cyst and idiopathic resorption were analysed through experimental methodology. For the ease of access an interactive GUI for the developed methodology was prepared and it is shown in Fig. 4.5a–h. The screenshots of the GUI portray step by step the process of interaction and the execution of the method. At first, the image is uploaded as shown in Fig. 4.5b, c. Then the image is converted to grey scale. Later seed points are selected on the greyscale image depending on the ROI and expert's advice/interaction as shown in Fig. 4.5d. In our case after 200 iterations the selected region of interest would be highlighted which is further processed and separated for further analysis. Edge is detected with a fixed threshold of 0.70 using canny edge detection method which is explained in the previous chapter. The extracted ROI is then measured –based on the number of pixels in which it is elaborated.

Few results of identification of cyst with the help of snakes model are shown below in Fig. 4.6. The first row represents the original image, and rest represent the variation in results by changing the number of seed points selected during the initial model generation of ROI and its evolution through different number of iterations. The effect so observed is displayed in the figure below where with different number of seed points and variations in iterations the closeness to achieve the desired ROI is shown. Finally, the extracted portion of cyst was analysed by further converting the image to binary form. The ROI so obtained through this process is identified as cyst. So using geometric operations area in the form of number of pixels was calculated.

Table 4.1 Parameter values for proposed process

Parameter	Alpha	Beta	Gamma	Kappa	$W(E_{\text{line}})$	$W(E_{\text{edge}})$	$W(E_{\text{term}})$
Value	0.4	0.2	1.0	0.15	0.3	0.4	0.7

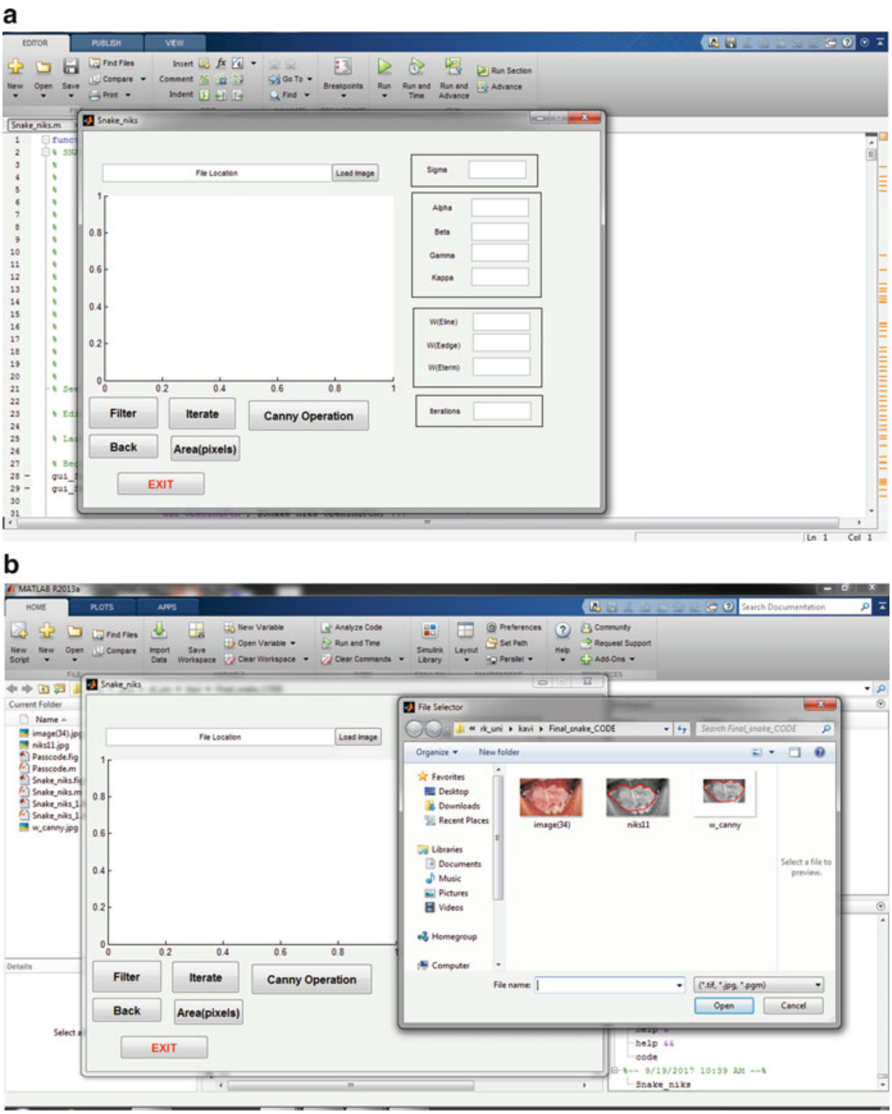

Fig. 4.5 An interactive tool for extraction of ROI. (**a**) GUI Screenshot stage 1. (**b**) GUI Screenshot stage 2. (**c**) GUI Screenshot stage 3. (**d**) GUI Screenshot stage 4. (**e**) GUI Screenshot stage 5. (**f**) GUI Screenshot stage 6. (**g**) GUI Screenshot stage 7. (**h**) GUI Screenshot stage 8

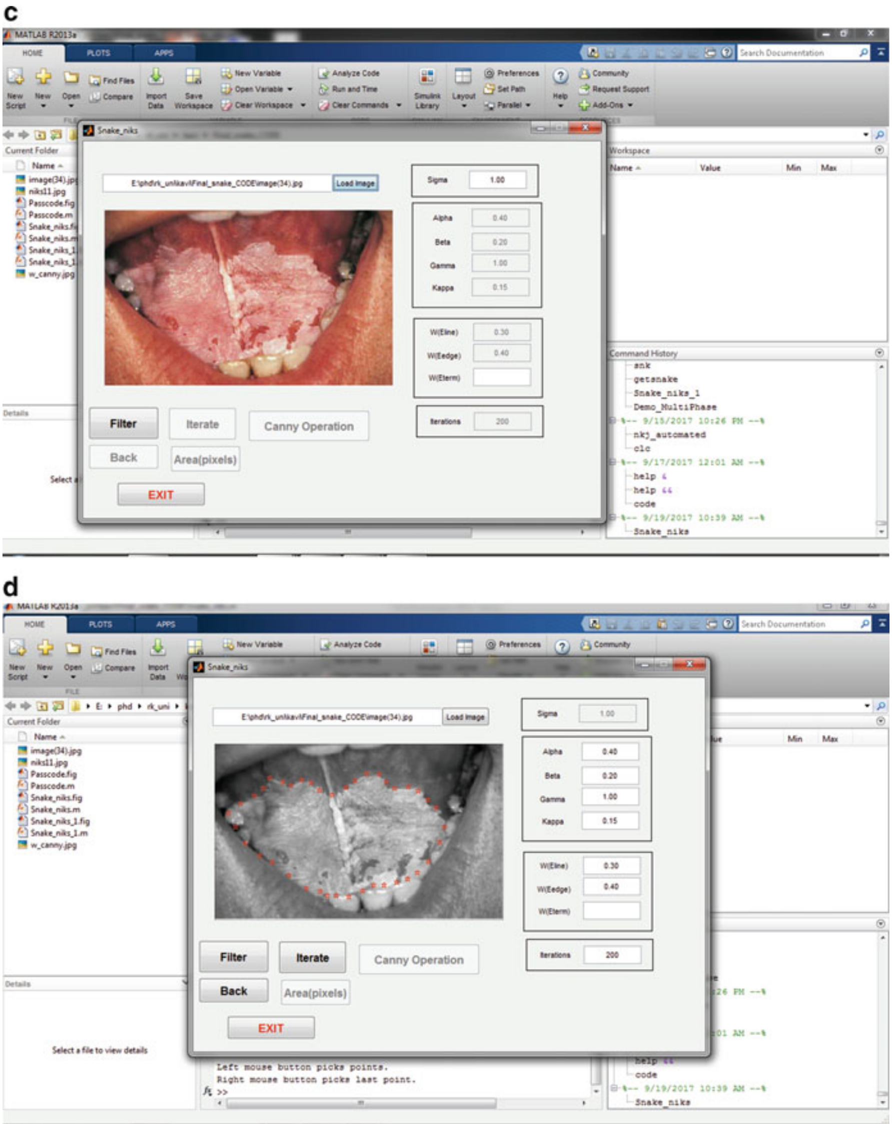

Fig. 4.5 (continued)

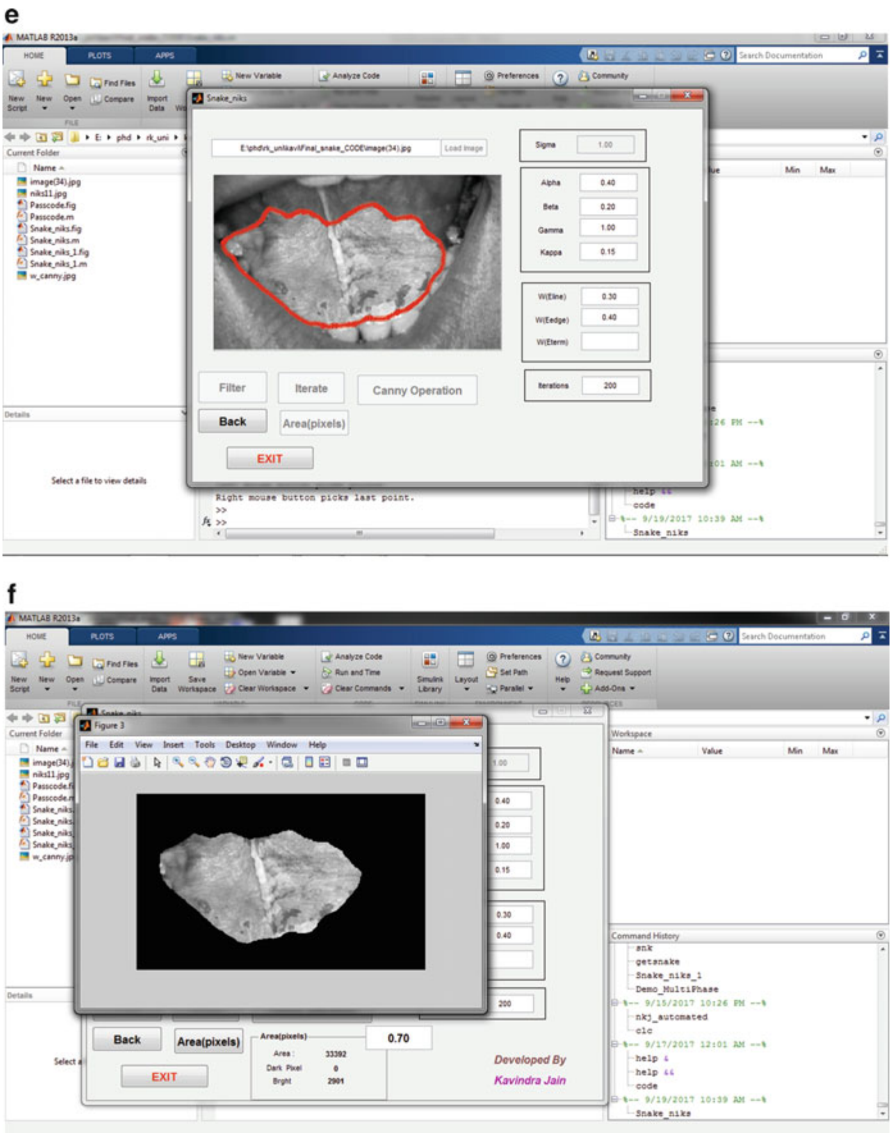

Fig. 4.5 (continued)

Few more identifications of different types of cyst with variation in number of seed points and evolution through different iterations are shown in Figs. 4.7 and 4.8.

The same approach of snakes model was applied on tongue-based diseases. The two particular problems being faced were red and white patches, namely erythroplakia and leucoplakia. Actually, these diseases are considered the

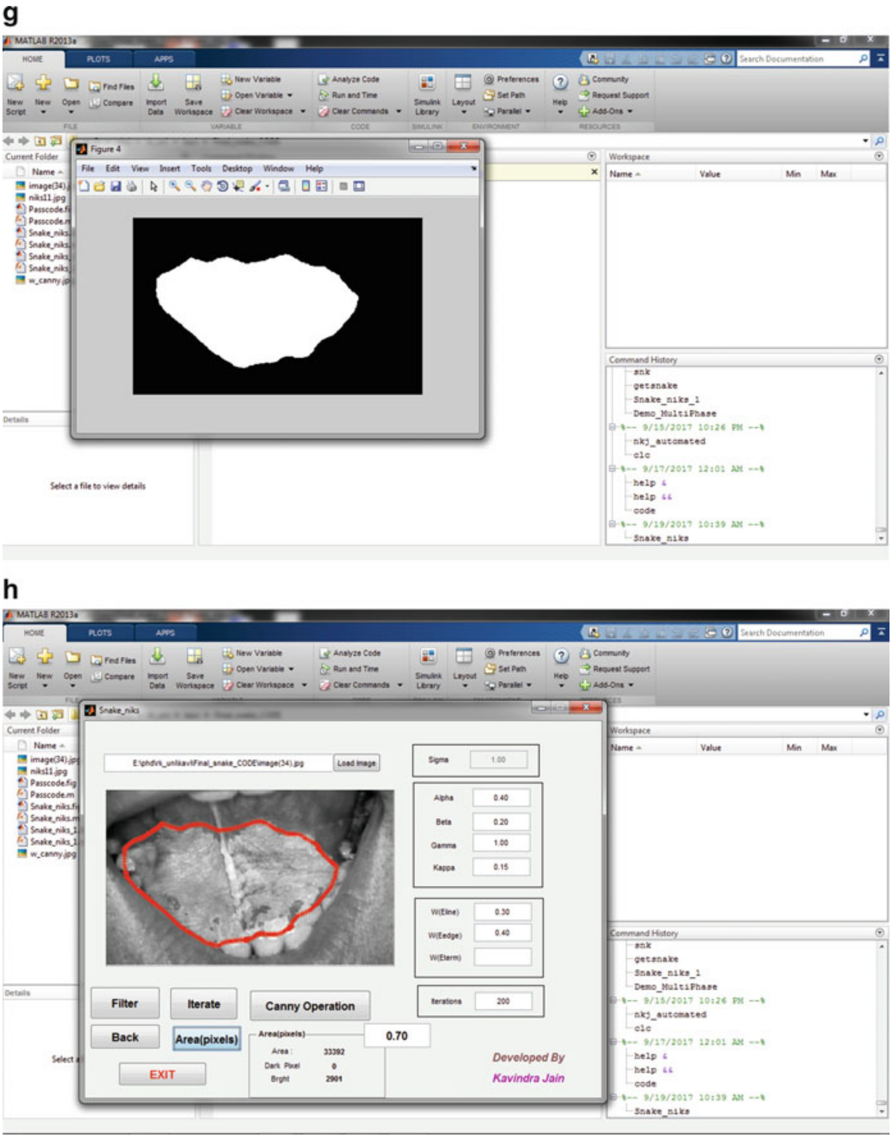

Fig. 4.5 (continued)

precancerous steps of oral mucosa. Their symptoms and tests are directly sent to the pathological laboratory for further processing. The given database images are provided in RGB planes. Images utilise the RGB planes straightforwardly to stand for colour images. But medical investigations have proved that the human eye

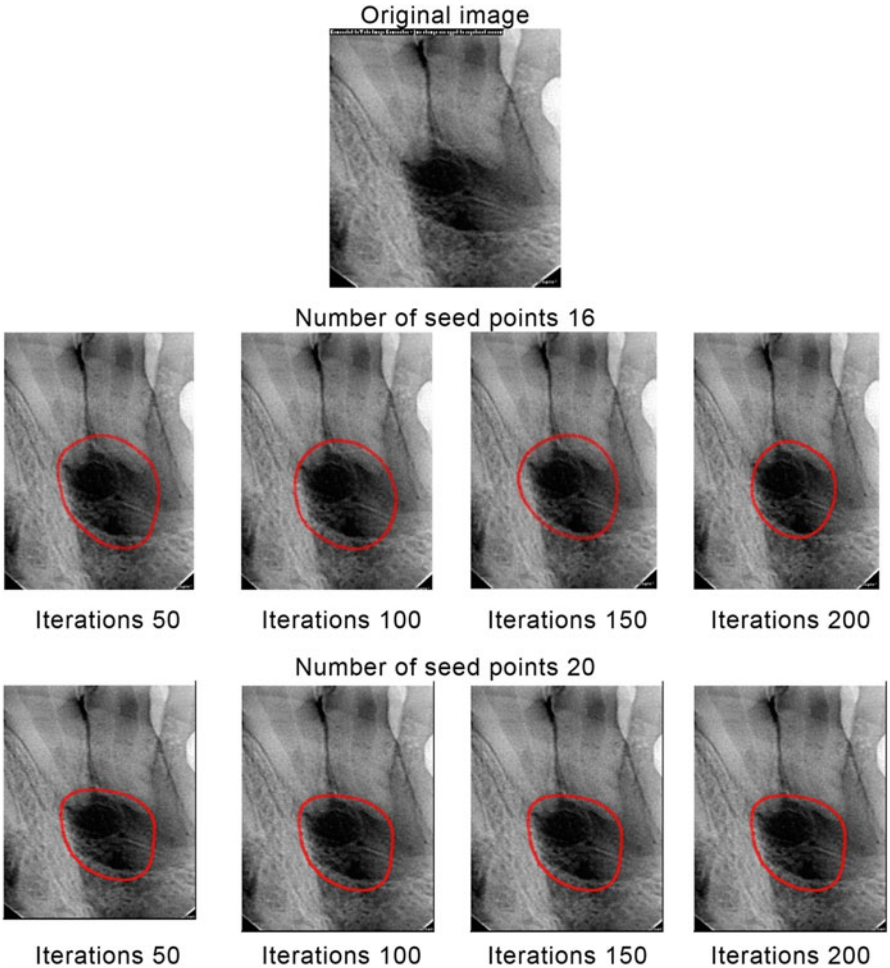

Fig. 4.6 Cyst identification of a test dental radiograph with different number of point selection and iterations

has dissimilar sensitivity to colour and brightness [57]. Thus there came an idea of converting RGB colour model to YCbCr model. It is specified in terms of luminance (Y channel) and chrominance (Cb and Cr channel). It segments the image into a luminous component and chrominance component. In YCbCr colour model, the distribution of the skin areas is consistent across different races in the Cb and Cr colour spaces. Its chrominance components are almost independent of luminance and there is non-linear relationship between chrominance (Cb, Cr) and luminance (Y) of the skin colour in the high and low luminance region. Analysing the concerned planes which contain maximum contents of white and red patches as shown in Figs. 4.9 and 4.10. Luminance is very comparable to the grayscale version of the original image. Cb is well built in case of parts of the image including the sky

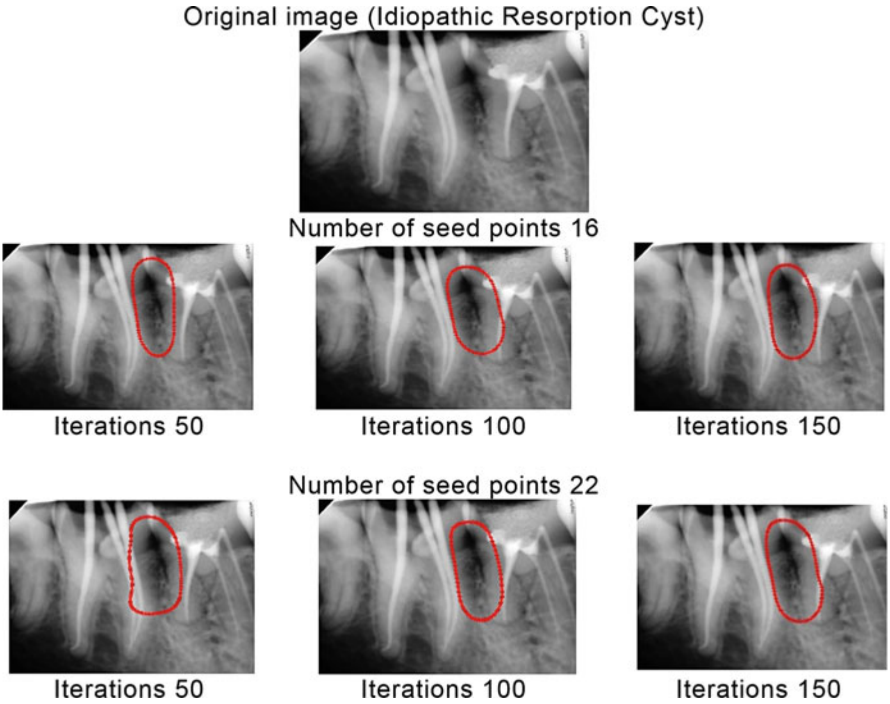

Fig. 4.7 Idiopathic resorpted cyst identification from dental radiograph with different iterations and seed points

(blue), both Cb and Cr are feeble in case of a colour like green, and Cr is strong in spaces of occurrence of glowing colours. In Figs. 4.9 and 4.10a represents the original image being converted to YCbCr. Separating the three different planes of Y, Cb and Cr in Fig. 4.10b–d respectively. Out of three planes Y plane has more information than Cb and Cr.

But the results so obtained were not uniform for all images and in case of dental radiographs too. Hence, proceeding further with snakes model the approach was modelled in that case and results are displayed in Fig. 4.11.

4.5 Evaluation Measurement for the Extracted ROI Using Snake Model

The parametric snakes model through GUI was investigated on various dental diseases. 177 erythroplakia-based red patches and 67 leucoplakia-based white patches on tongue were detected and diagnosed by our proposed process correctly. A total of 372 dental radiographs of RVG file format-based dental images were also being diagnosed. The performance parameters as discussed in Chap. 3 (Sect. 3.5) accuracy, precision, error rate and specificity are also investigated

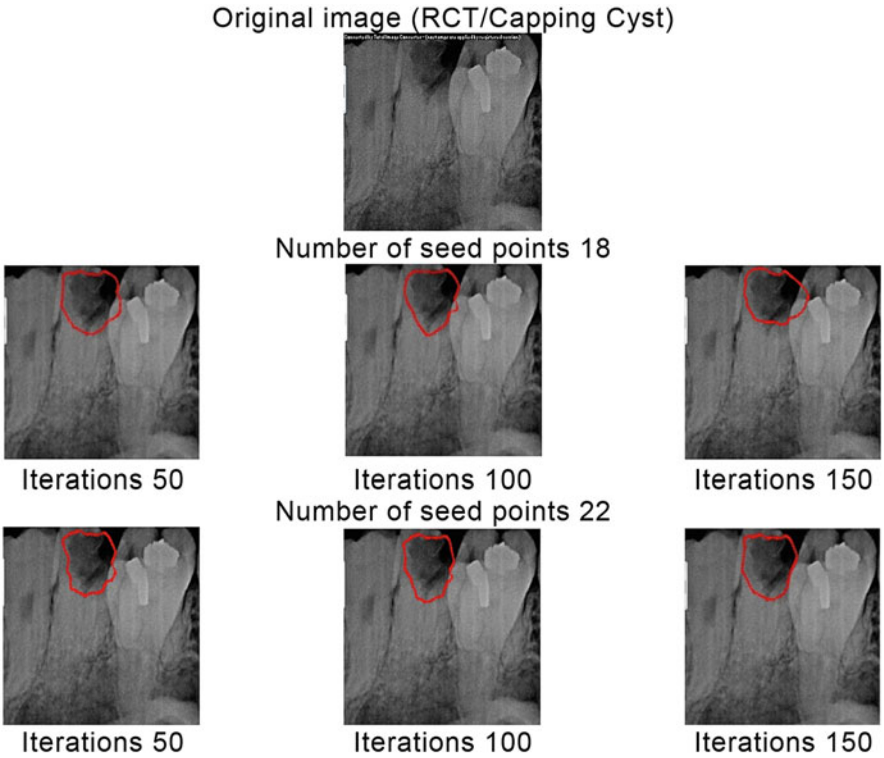

Fig. 4.8 Endodontic cyst identification from some dental radiograph with different iterations and seed points

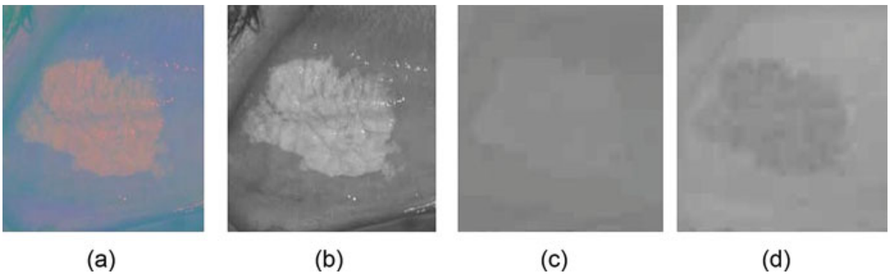

Fig. 4.9 Conversion of leucoplakia image to YCbCr model and separating in Y, Cb, Cr plane

on these images. Based on the above defined parameters for measurement, the confusion matrix for one of the radiographic images and ROI of Ground truth set-1 is shown in Table 4.2.

The confusion matrix shown in Table 4.2 shows the accuracy of the segmented resultant image based on ground truth to be 86.26%. For this image the error rate is 13.73%, precision is 16.32% and specificity is 87.45%. According to the confusion

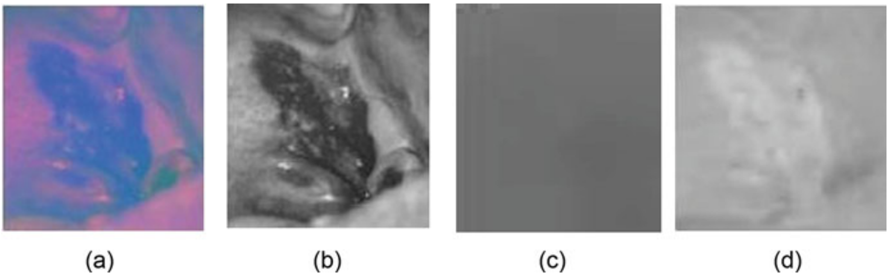

Fig. 4.10 Conversion of erythroplakia image to YCbCr model and separating in Y, Cb, Cr plane

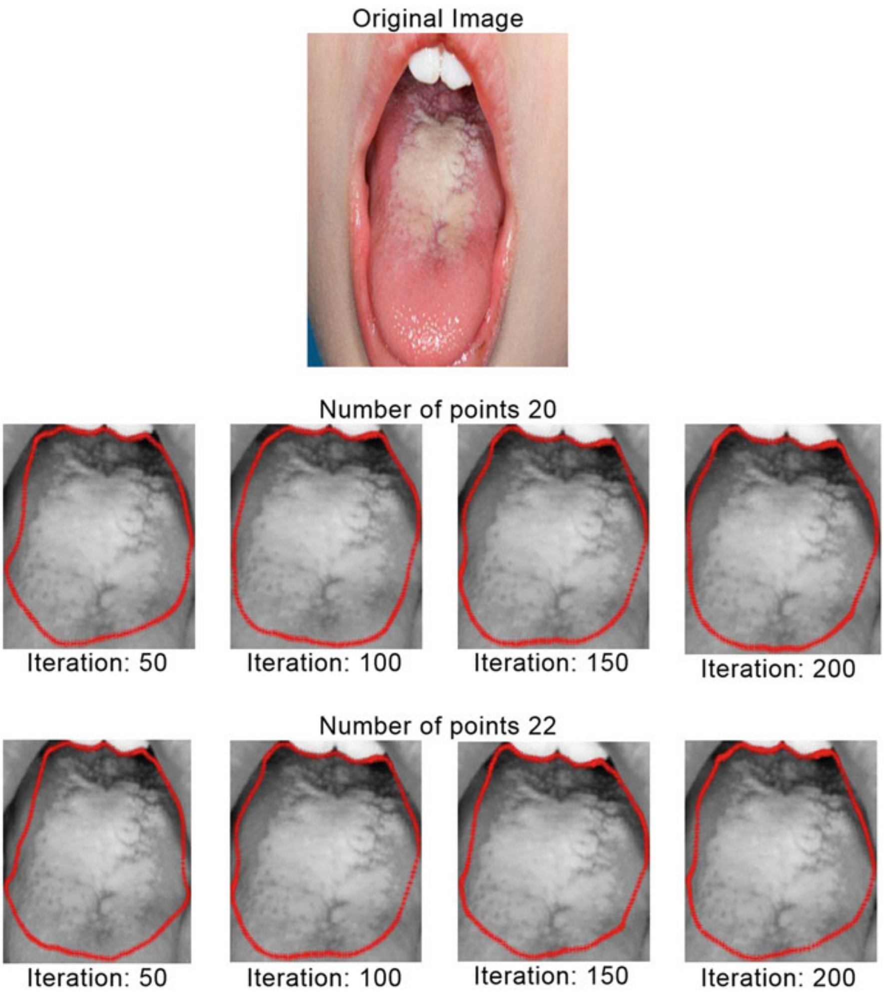

Fig. 4.11 Erythroplakia and leucoplakia patch identification of using snakes model from sample radiographs with different iterations and seed points

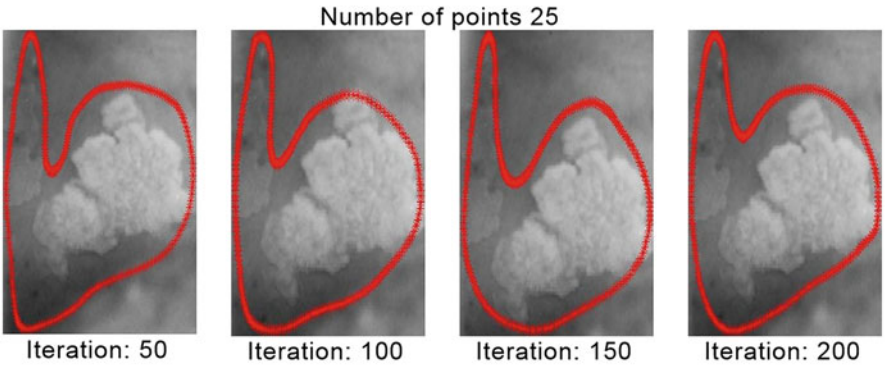

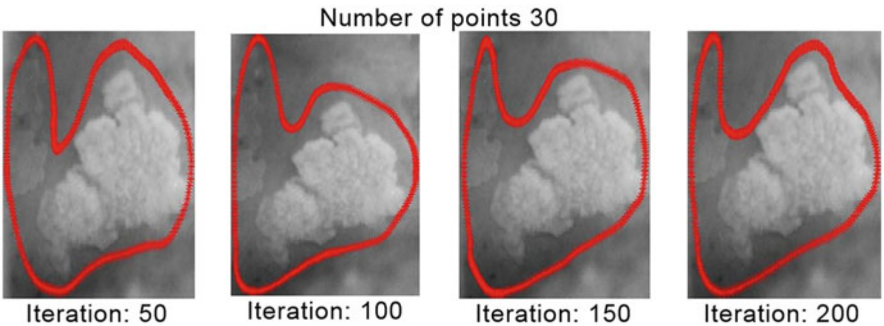

Fig. 4.11 (continued)

matrix shown in Table 4.2 the accuracy, precision, error rate and specificity of our segmented results of proposed process 1 and ROI of ground truth set-1 are presented in Table 4.3.

With the help of results of performance measures, it can be depicted that the suggested approach is quite useful for the semi-automatic segmentation and analysis of dental radiograph images during the process of dental treatment. The

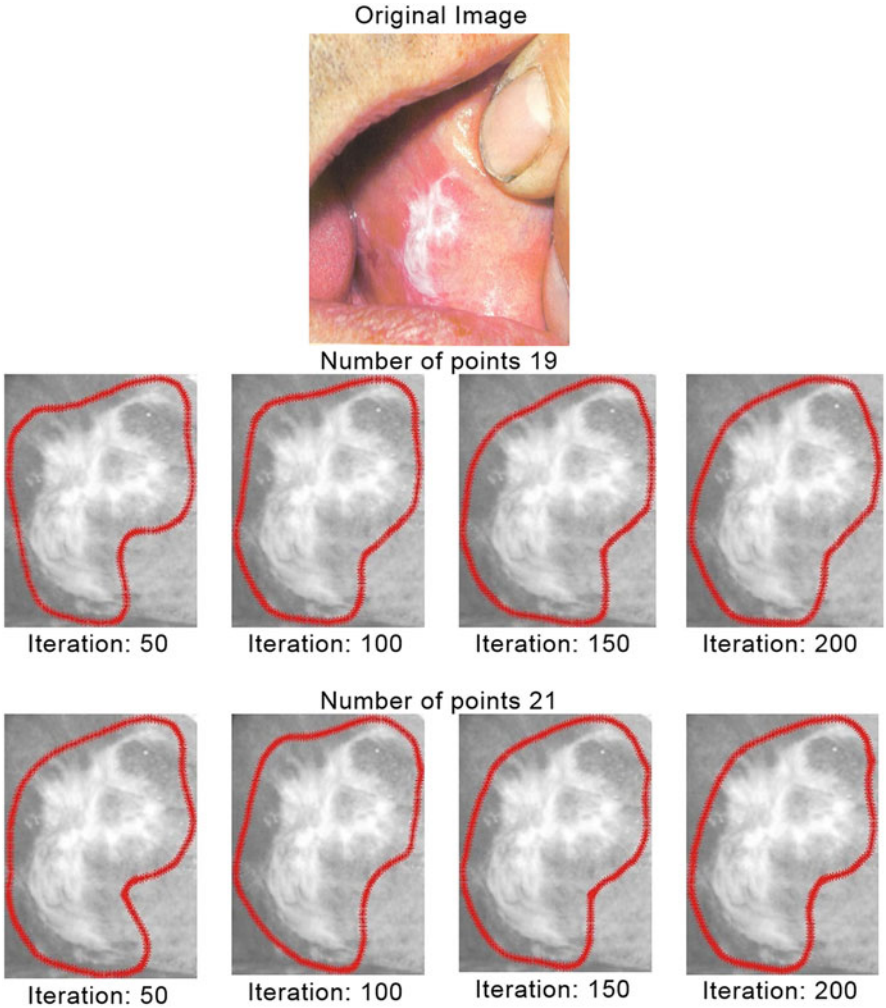

Fig. 4.11 (continued)

results produced by the proposed method were shown to the respective dentist and were found to be really helpful. The average is resultant of 616 such images taken for analysis is shown in Table 4.3, the bar chart of the same is shown in Fig. 4.12. Average accuracy of 616 data base images was found to be 83.29% with precision of 35.88%, error rate of 16.70% and specificity of 91.57%.

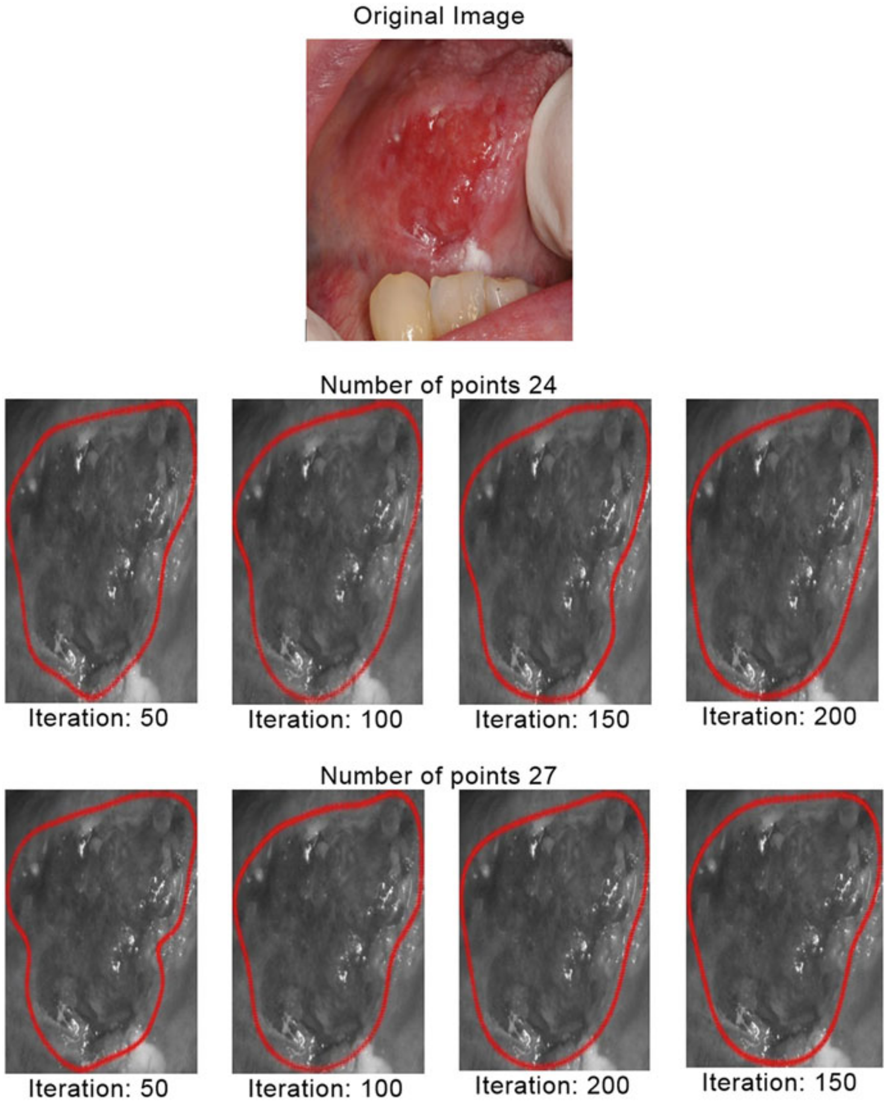

Fig. 4.11 (continued)

4.6 Summary and Concluding Remarks

Oral mucosa-based images for research work were obtained by the courtesy of Dr. Dhrumin Patel. Here, in the proposed snakes-based approach we took the points directly so that it can automatically extract the affected part. An entire interactive tool with GUI was developed in MATLAB and used to generate all results shown in

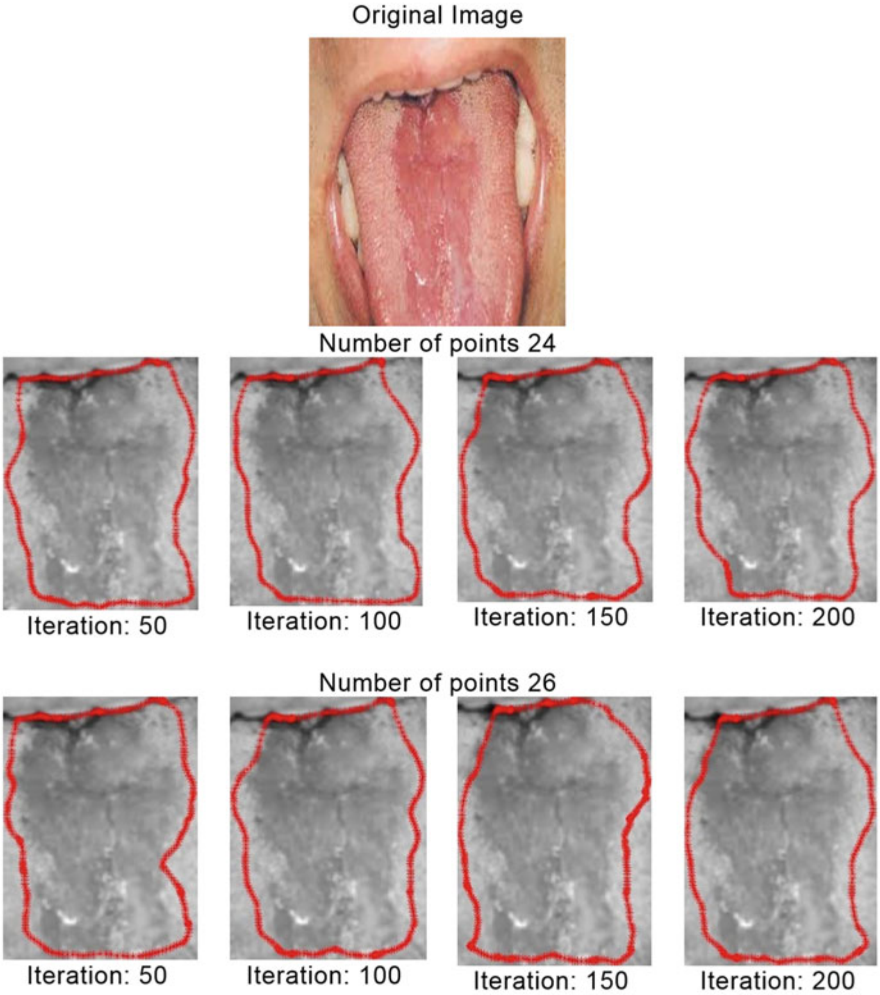

Fig. 4.11 (continued)

this chapter. In addition to snakes model, some of the basic features like area and canny were also included in the GUI-based tool. This interactive user friendly approach can help practitioners in identification of region of interest which can be further used for a precancerous treatment. It was observed that cases with precancerous treatment under erythroplakia and leucoplakia were satisfactorily diagnosed and results obtained were satisfactory for helping out the practitioners too.

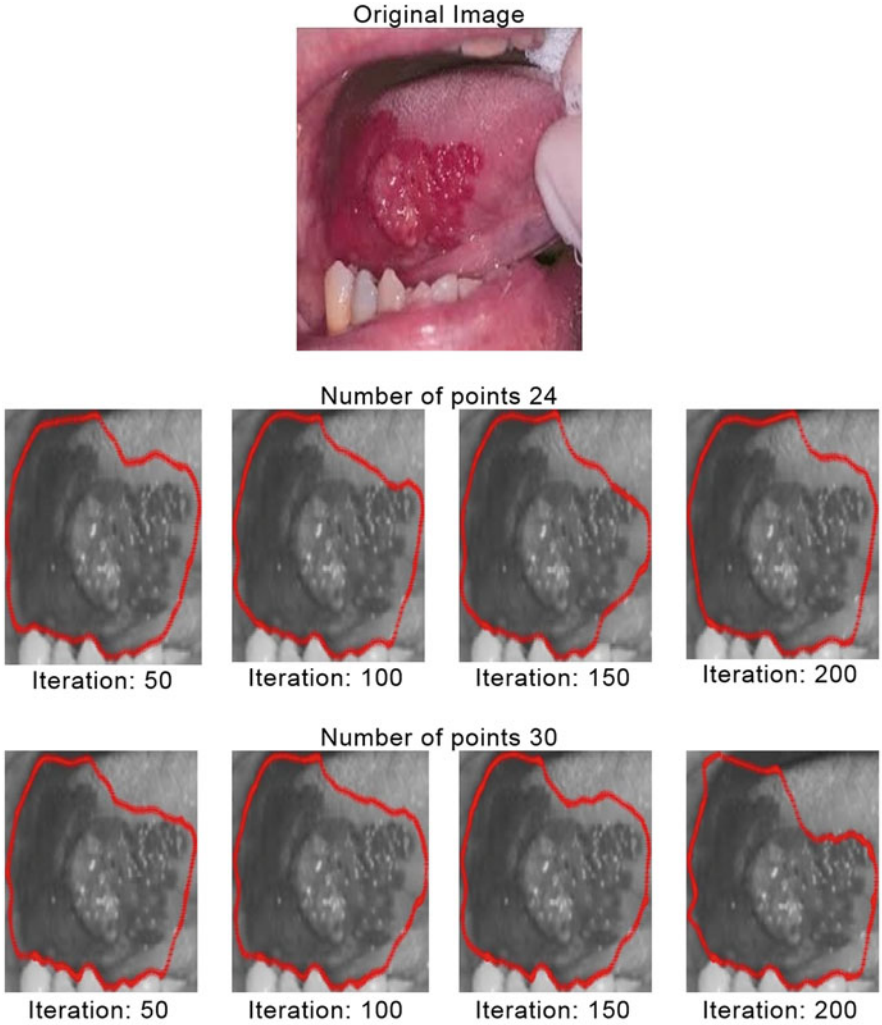

Fig. 4.11 (continued)

Table 4.2 Confusion matrix of a sample radiograph with reference to its ground truth

	Predicted class			
Actual class		Yes	No	Total
	Yes	1751	1265	3016
	No	8976	62,566	71,542
	Total	10,727	63,831	74,558

Table 4.3 Evaluation parameters of 15 images and its average over 616 dental radiographic images

Images	Accuracy	Precision	Error rate	Specificity
1	85.52	8.23	14.47	92.38
2	86.26	16.32	13.73	87.45
3	83.65	6.79	16.34	89.05
4	76.16	10.31	23.89	86.48
5	87.67	20.05	12.32	89.42
6	85.17	28.17	14.82	96.32
7	77.29	6.13	22.70	84.58
8	75.08	06.00	24.91	82.18
9	73.23	15.29	26.76	81.90
10	83.10	6.55	16.89	83.80
11	88.35	10.31	11.64	89.17
12	82.14	5.78	17.85	82.55
13	81.41	19.79	18.58	84.70
14	83.33	8.10	16.66	85.58
15	78.67	16.63	21.32	84.96
Avg. 616 images	83.29	35.88	16.70	91.57

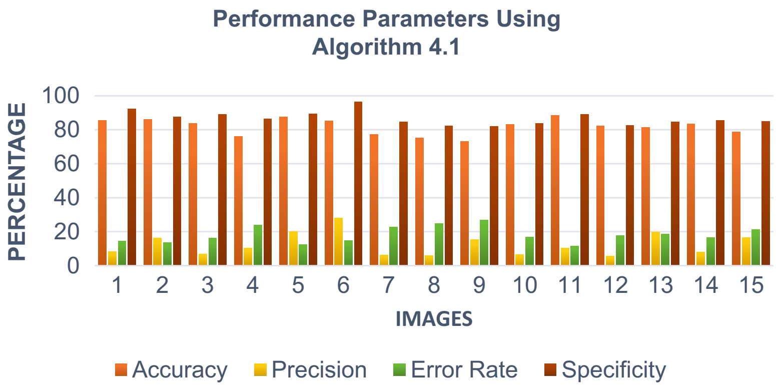

Fig. 4.12 Parametric evaluation measures based on Algorithm 4.1

Chapter 5
Multiphase Level Set Segmentation for ROI Extraction from Dental Radiographs

5.1 Introduction

Image guided surgery, quantitative analysis and visual understanding along with proper medical interpretation have led to the development of segmentation techniques in image processing in a more precise manner [58]. As seen in the previous chapter and state-of-the-art review, the low-level segmentation methods like pixel-based segmentation, region growing and filter-based edge detection depend on additional preprocessing and postprocessing methods. Due to their semi-automated nature, they require interventions or information of medical practitioners. In this chapter, we study and use a new approach to further automate the process and reduce/eliminate requirement of interventions from the process during identification of region of interest.

The deformable models provide an explicit representation of the boundary and shape of the object [59]. Various features like inherent connectivity and smoothness which counteract noise and boundary irregularities are present in such models. Based on the region of interest they incorporate knowledge of the nearby regions. While using parametric model we faced certain pitfalls. Firstly, the conditions when the initial model and region of interest boundary differ greatly in size and shape, resulting in high error rate and lesser accuracy as discussed in previous chapter. Secondly, it was observed that when the region of interest is large, then the model has to be applied more than once separately for each case.

To overcome such situations, the level set deformable models also referred as geometric deformable model which provide an elegant solution to address the primary limitation of parametric deformable model [60]. It includes no parameterisation of the contour, topological flexibility and good numerical stability.

K. R. Jain, N. C. Chauhan, *Dental Image Analysis for Disease Diagnosis*,
https://doi.org/10.1007/978-3-030-14136-3_5

5.2 Level Set Framework

In 1988 Osher and Sethian [61] proposed the idea of geometric deformable model which lead to an implicit formulation of deformable contour in a level set framework. Consider a closed contour dedicated as a region of interest for our boundary as C deforming with a speed S along with its normal direction

$$|\nabla C|S = 1 \quad S > 0 \tag{5.1}$$

The main motive is to embed the curve into higher dimension function $\Phi(x,y,t)$ instead of tracking it in time positions.

$$\Gamma(t) = \{(x, y)|C(x, y) = t\} \tag{5.2}$$

Γ represents the closed curve w.r.t time. The conditions would be as follows:

- At time zero the initial contour C_o symbolises the level zero of the function Φ

$$C_O = \{(x, y)|\varphi(x, y, 0) = 0\} \tag{5.3}$$

- Function Φ evolves with dynamic equation

$$\frac{\partial\varphi}{dt} = |\nabla\varphi|S \tag{5.4}$$

So the modified level set frame is defined as (Fig. 5.1)

$$\Gamma(t) = \{(x, y)|\varphi(x, y, t) = 0\} \tag{5.5}$$

Various level set segmentation methods based on image gradient intensity have limitation of accurate region of interest segmentation in areas with low contrast [62]. Secondly the segmentation methods are quite sensitive to initial seed point position. It leads to false edges corresponding to local minima of the function. In case of medical images which are quite prone to insufficient and spurious edges inherent to light acquisition and noise due to machines, it become quite difficult to segment the image properly [63].

To solve the above said problem two approaches came to spot light. First is to fuse regularise terms in the speed function [64] while the second is to reformulate the problem in terms of region-based segmentation derived from Mumford–Shah function implemented in a level set framework [65].

Mumford–Shah function [66] do not assume inhomogeneity of image intensities; therefore, they are able to segment images with intensity inhomogeneity.

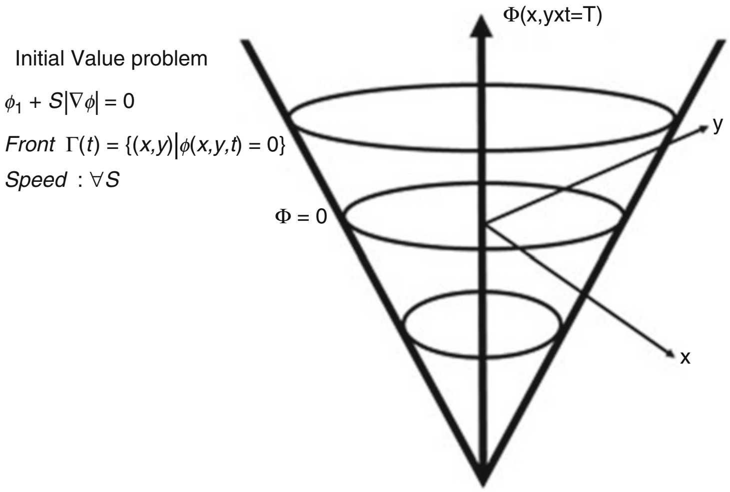

Fig. 5.1 Implicit level set formulation with speed term along the normal direction

5.3 Proposed Approach

We propose a region-based process for segmentation of dental radiograph images in this chapter. Here we would derive a local intensity clustering property. Later, it would be integrated over the neighbourhood centre to define an energy function which is converted to a level set formulation. Using level set evolution and estimation of bias field minimisation of vitality is formulated. The overall key steps for the implementation of proposed approach is briefed in the form of Algorithm 5.1.

Algorithm 5.1 Segmentation of Dental Radiograph Using Multiphase Level Set Approach
Steps:

1. Formulation of Image Model
2. Nearby power bunching property
3. Vitality detailing
4. Level set definition and vitality minimisation
5. Three-phase level set formulation
6. Vitality Minimisation
   (a) Vitality Minimisation with respect to θ
   (b) Vitality Minimisation with respect to C
   (c) Vitality Minimisation with respect to e
7. Numerical Implementation

5.3.1 Formulation of Image Model

Keeping in mind the end goal to manage power inhomogeneities in image segmentation, we define our strategy in light of an image model that depicts the structure of true images, in which force inhomogeneity is credited to a part of an image. We consider the accompanying multiplicative model of force inhomogeneity. From the prospect of image processing an image can be modelled as

$$P = eL + r \tag{5.6}$$

where L indicates true or actual image. e represents variation in intensity, that is, bias field and r represents Gaussian noise. We consider image I as a function $P : O \to \mathfrak{R}$ in continuous time domain O. e can be more profoundly defined as a constant at each point in the image. L on the contrary can be considered as constants alongside of impaired sections of O_1, O_2, and $O_3 \ldots O_N$. Hence, according to Eq. 5.6 and above-defined terminologies, this method suggest to fragment the image based on the segmentation properties.

5.3.2 Nearby Power Bunching Property

Local level image division techniques normally depends on a specific local descriptor (e.g. force mean or a Gaussian dispersion) of the intensities in every area to be sectioned. In any case, it is difficult to give such an area descriptor for pictures with force inhomogeneity. In addition, power inhomogeneity regularly prompt cover between the appropriations of the intensities in the areas O_1, O_2, $O_3 \ldots O_N$. Along these lines, it is unthinkable to portion these locales straightforwardly taking into account the pixel intensities. Moreover, the property of neighbourhood intensities is basic, which can be successfully abused in the definition of our technique for image fragmentation with synchronous estimation of the inclination field.

In light of the image model in Eq. 5.6 and the terminologies of L and e, we can infer a helpful property of neighbourhood intensities, which is alluded to as a nearby power grouping property as portrayed and justified underneath. To be specific, we consider a round neighbourhood with a span focused at every point as shown in Eq. 5.6a defined by Eq. 5.6b.

$$y \in O \tag{5.6a}$$

$$\begin{aligned} & y \in O \\ & A_y =^{\nabla} \{x : |x - y| \le \rho\} \end{aligned} \tag{5.6b}$$

For a slowly varying bias field e, the values $e(x)$ for all x in the circular neighbourhood A_y are close to $e(y)$, that is, $e(x) \approx e(y)$ for

$$x \in A_y \tag{5.7}$$

Therefore, the intensities $e(x)\,L(x)$ in each sub region $A_y \cap O_i$ are close to constant $e(y)\,c_i$, that is,

$$e(x)\,L(x) \approx e(y)\,c_i \text{ for } \mathrm{A_y} \cap O_i \tag{5.8}$$

Hence, the modified image model in Eq. (5.1) becomes

$$P(x) = e(y)\;\; c_i + r(x) \quad \text{for}\;\; x \in A_y \cap O_i \tag{5.9}$$

where $r(x)$ is additive zero mean Gaussian noise. Hence, the intensities in the set ensembles in such a way that every distinct bunch are well separated and have their own loci as $m_i \approx e(y)c_i$.

$$P_y^i = \{P(x) : x \in A_y \cap O_i \tag{5.10}$$

Each such loci is unique in itself and have its own identity. This property of nearby bunching is used further in the proposed approach [67].

5.3.3 Vitality Detailing

In the upper subsection the nearby power bunching capability helps us in getting a clear idea that the intensities in the nearby areas can be distinguished into N such bunches having their own loci. With the help of K-means method our target is to reduce the number of bunches [67]. It can be done using a windowing function. So the final equation for such bunching criteria is given in Eq. (5.11).

$$\varepsilon_y = \sum_{i=1}^{N} \int_{O_i} K(y-x)|P(x) - e(y)c_i|^2 dx \tag{5.11}$$

where ε represents the vitality, $K(y–x)$ expresses the windowing function. Therefore, the need is to reduce the vitality for all y in O. This can be done by reducing the integral of vitality with respect to O.

5.3.4 Level Set Definition and Vitality Minimisation

The vitality ε in Eq. (5.11) is communicated as O_1, O_2, and $O_3 \ldots O_N$. It is difficult to determine an answer for the vitality minimisation issue from this statement of ε.

In this area, the vitality is changed over to a level set detailing by speaking to the disjoint locales O_1, O_2, $O_3 \ldots$ O_N with various level set capacities, with a regularisation term on these level set capacities. In the level set detailing, the vitality minimisation can be settled by utilising entrenched variational techniques [68]. In level set techniques, a level set capacity is a capacity that take positive and negative signs, which can be utilised to speak to a segment of the area O into three disjoint districts, O_1, O_2 and O_3. Let $P : O \to \mathfrak{R}$ be a level set capacity, then its signs define three disjoint locales,

$$O_1 = \{x : \theta(x) > 0\}, O_2 = \{x : \theta(x) < 0\} \text{ and } O_3 = \{x : \theta(x) = 0\} \tag{5.12}$$

which frame a parcel of the space O. For instance, two or more level set capacities can be utilised to areas of O. The level set definition of the vitality can then be defined as three-phase level set formulation in next subsection.

5.3.5 *Three-Phase Level Set Formulation*

We first consider the three-phase case: The region of interest O is divided into three disjoint locales, O_1, O_2 and O_3. Furthermore, for this situation, a level set capacity θ is utilised to represent three regions based on Eq. (5.11). These regions can now be defined by two level sets as θ_1 and θ_2 respectively, where $M_1(\theta_1, \theta_2) = H(\theta_1)H(\theta_2)$, $M_2(\theta_1, \theta_2) = H(\theta_1)(1-H(\theta_2))$ and $M_3(\theta_1, \theta_2) = 1-H(\theta_1)$ respectively, where H represents Heaviside function [69]. Thus, the energy Eq. 5.11 can be modified as

$$\varepsilon = \int \left(\sum_{i=1}^{N} \int K(y-x)|P(x) - e(y)c_i|^2 M_i\big(\theta_1(x), \theta_2(x)\big)dx \right) dy \tag{5.13}$$

The vitality detailing is achieved by a continuous process, in each iteration the vitality is reduced based upon the $\varepsilon(\theta, e, c)$ with respect to each variable θ, e, c. We can rewrite this equation in the following form:

$$\varepsilon(\theta, e, c) = \int \left(\sum_{i=1}^{N} \int e_i(x) M_i(\theta(x))dx \right) \tag{5.14}$$

where e_i is the function defined by

$$e_i(x) = \int K(y-x)|P(x) - e(y)c_i|^2 dy \tag{5.15}$$

With the help of the above equation we try to minimise this energy and form an Equation on the basis of level set function θ and estimation of the bias field e.

The process of minimisation is iterative and on the basis of speed function F which is able to minimise $F(\theta,c,e)$ with respect to each of the variable θ, c and e [70]. So the solution to vitality reduction is with respect to each of the variables as follows:

1. *Vitality detailing with respect to "θ"*

For fixed values of e and c the detailing of $\varepsilon(\theta, e, c)$ can be calculated using gradient descent method by gradient flow Equation

$$\frac{\partial \theta}{\partial t} = -\frac{\partial F}{\partial \theta} \tag{5.16}$$

where $\frac{\partial F}{\partial \theta}$ is the Gateaux derivative which can further be modified based on Mumford shah function as

$$\frac{\partial \theta}{\partial t} = -\delta(\theta)(e_1 - e_2) + v\delta(\theta)\mathrm{div}\left(\frac{\nabla \theta}{|\nabla \theta|}\right) + \mu \mathrm{div}\big(d_p(|\nabla \theta|)\nabla \theta\big) \tag{5.17}$$

where gradient and divergence operator along with d_p is defined as

$$d_p(s) \triangleq \frac{p'(s)}{s} \tag{5.18}$$

While the evolution of level set function was being done in Eq. 5.17 the constants e_1 and e_2 in the bias field are updated by minimising the vitality $\varepsilon(\theta, e, l)$ with respect to e and l.

2. *Vitality detailing with respect to "c"*

For the constant values of θ and e the l parameter minimises the vitality $\varepsilon(\theta, e, l)$ denoted by below model is symbolised as

$$\begin{aligned} \hat{c} &= c_i^{\wedge}, \ldots, c_n^{\wedge} \\ c_i^{\wedge} &= \frac{\int (e * M) P v_i dy}{\int \left(e^2 * M\right) v_i dy} \end{aligned} \tag{5.19}$$

as $u_i(y) = M_i(\theta(y))$.

3. *Vitality detailing with respect to "e"*

For the constant values of θ and c the e parameter minimises the vitality $\varepsilon(\theta, e, c)$ which is denoted by $\hat{e}$is provided by Eq. (5.19). The convolution in Eq. 5.13 shows the slowly varying characteristics of $\hat{e}$.

$$\hat{e} = \frac{\left(P\sum_{i=1}^{N} l_i v_i\right) * M}{\left(P\sum_{i=1}^{N} l_i^2 v_i\right) * M} \tag{5.20}$$

Moreover the Heaviside function H is swapped by a suave function that provides a close value to H.

5.3.6 Multiphase Level Set Formulation

For the case of $N \geq 3$ or more we can use two or more level set functions $(\theta_1, \theta_2 \ldots \theta_k)$ by a vector valued function Φ. Hence, the membership function can be reformulated as $M_i(\Phi)$. The energy can be converted to multiphase level set formulation as

$$\varepsilon(\Phi, e, c) = \int \left(\sum_{i=1}^{N} \int e_i(x) M_i(\Phi(x)) dx \right) \tag{5.21}$$

The energy functional F in our multiphase level set function formulation based on gradient flow equation it can be further formulated staring from θ_1, $\theta_2 \ldots \theta_k$ form individual gradient flow equation.

5.4 Experiment and Results

To demonstrate the effect of proposed method for fragmentation. Consider a dental radiograph image as shown in Fig. 5.2a. This radiographic image is referred for endodontic treatment. According to our proposed approach the radiograph is first preprocessed and then segmented. In this process the random points are generated for initialisation and then slowly these areas grow according to the vitality increase or decrease in the nearby regions. Finally, we get a fragmented image based on three-phase level set method as theoretically explained in proposed algorithm in Sect. 5.3. The red region displayed in Fig. 5.2b shows the affected areas for endodontic treatment. Later on based on fragmentation and level set the three areas are given same vitality for the purpose of identification as black grey and white. Hence, as shown in Fig. 5.2c, the black portion between two teeth are the affected areas for analysis along with the tooth itself having black portion in neck of tooth encircled in the radiograph.

As described in the chapter we have run the code on various databse images and their results will be attached here. This approach of segmentation is investigated on different dental radiographs containing different dental problems such as idiopathic

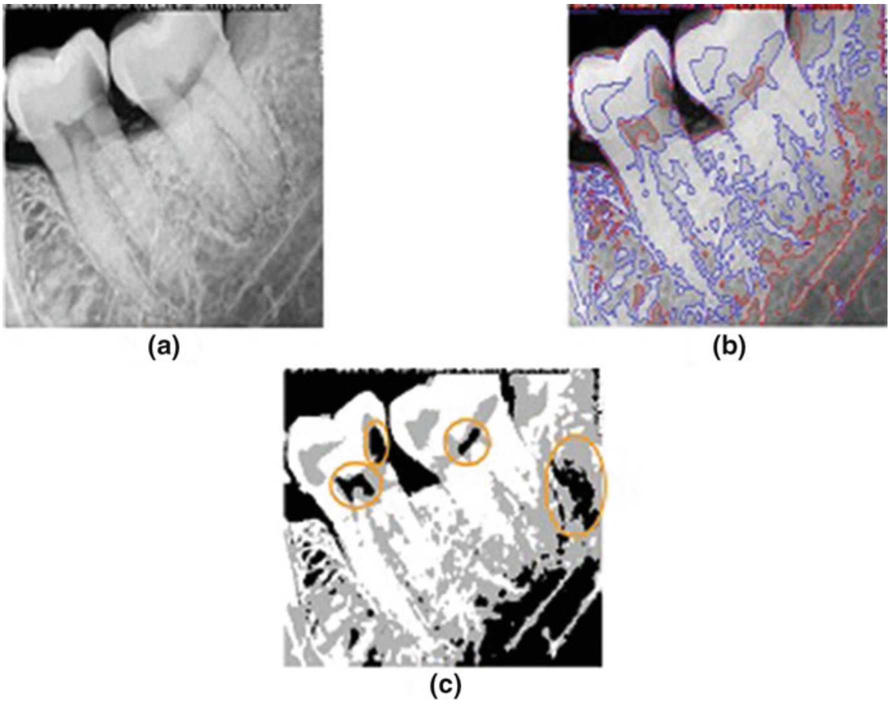

Fig. 5.2 Segmentation of a dental radiograph using three-phase level set method: (**a**) Original dental radiograph, (**b**) Segmentation status after 99 iterations, (**c**) Final segmented radiograph

resorption, abcess and cyst as well as root canal-based problems. The results obtained are displayed in Fig. 5.3. Figure 5.3a1–a15 represents the original images in the first column, whereas Fig. 5.3b1–b15 represents the image after 99 iterations in the second column, and lastly the segmented image is shown in Fig. 5.3c1–c15 in the third column.

5.5 Evaluation Measurement for Prediction of ROI

The geometric model using three-phase level set segmentation was applied on various dental cases. A total of 723 cases (dental radiographs) of RVG format were analysed. As stated in database summary. The segmented images were validated based on comparison with two sets of ground truth images. These ground truth images were obtained from two dental practitioners. The region of interest in both ground truth image sets are marked by colours red and yellow in Fig. 5.4. The first and second column represents the ROI of ground truth set-1 and set-2 in

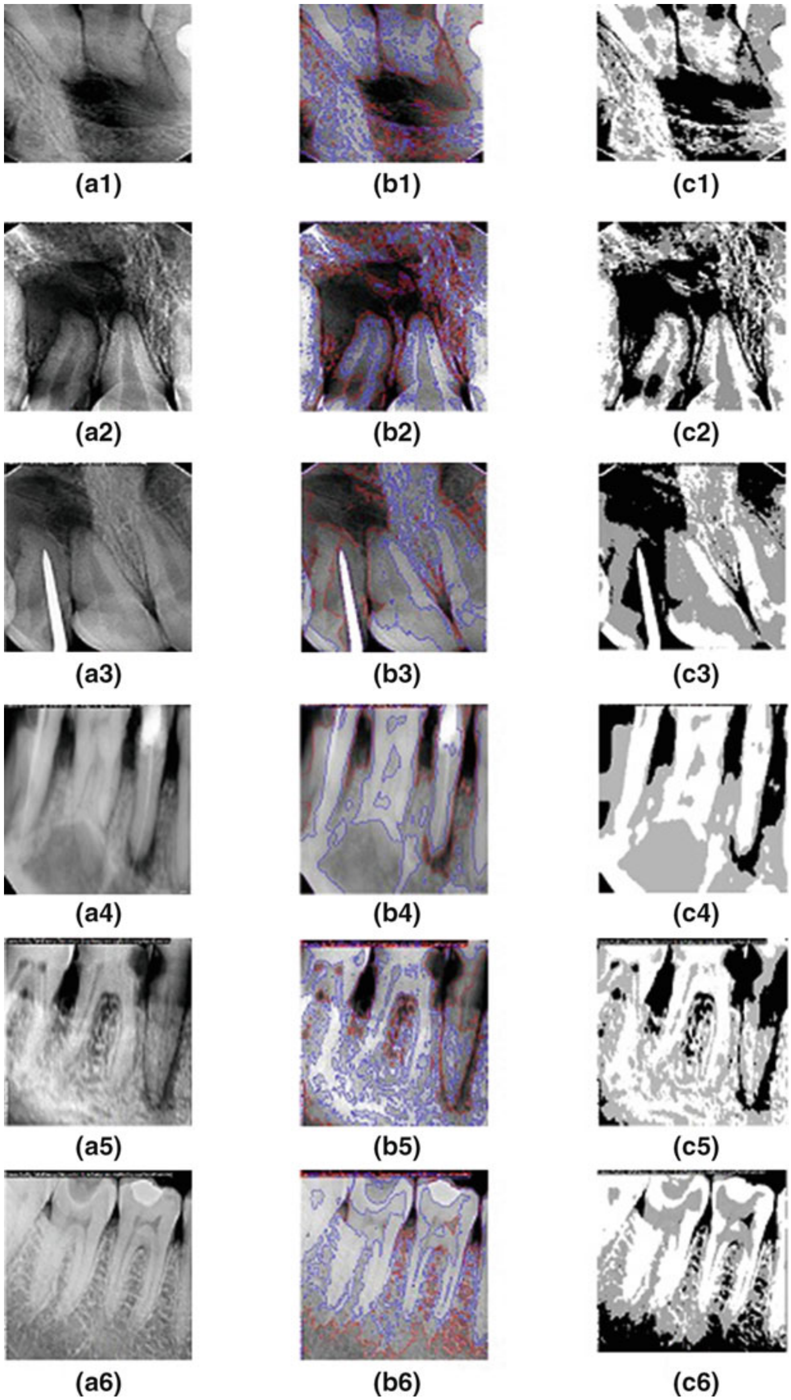

Fig. 5.3 Segmentation results on dental radiograph using multiphase level set method

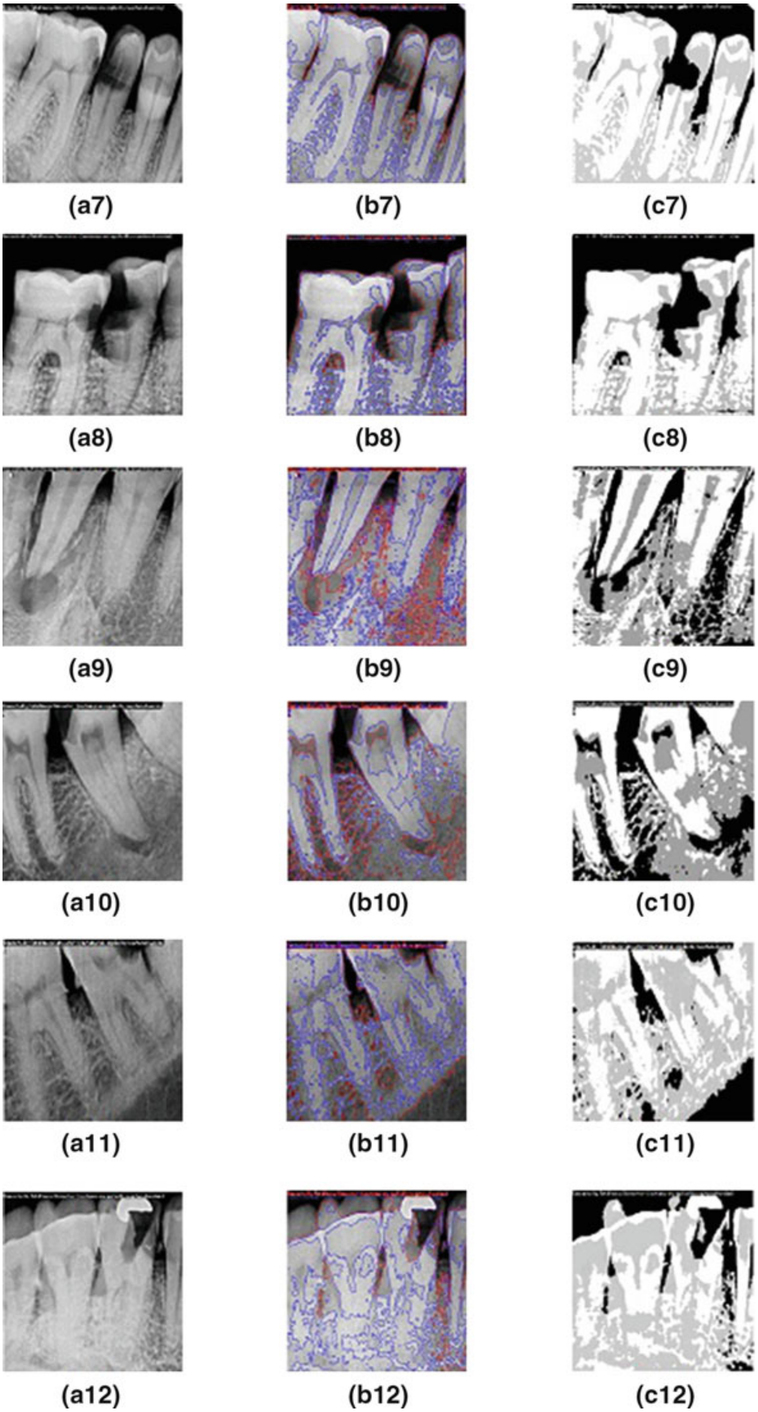

Fig. 5.3 (continued)

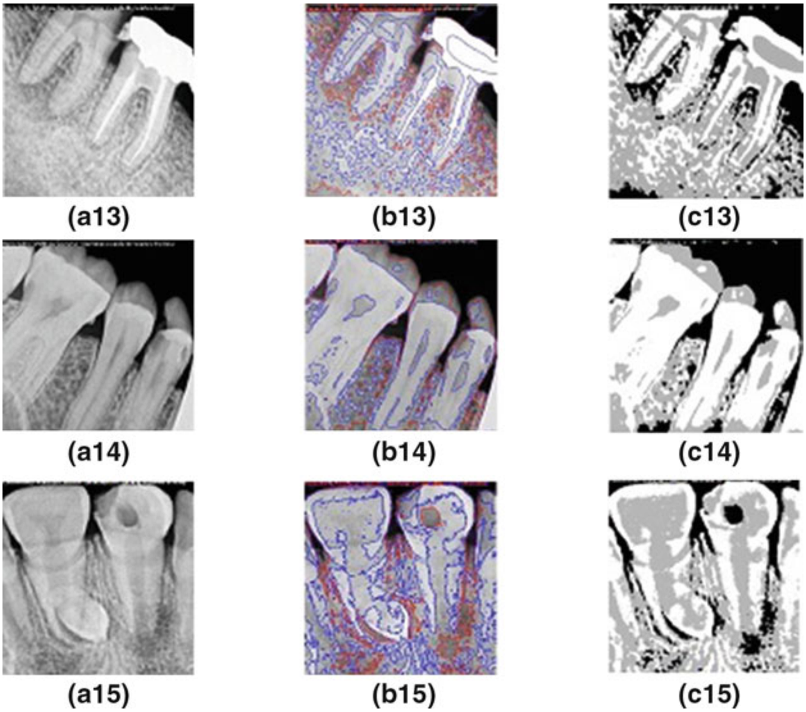

Fig. 5.3 (continued)

Fig. 5.4a1–a11 and in Fig. 5.4b1–b11 respectively. The third column represents the segmented image obtained from our proposed method in Fig. 5.4c1–c11.

As shown in Fig. 5.4 the first column represents images in which the ROI is marked by first expert, that is, the ROI is selected by one dentist in yellow boundaries. The second column represents images in which ROI is indicated by second expert, that is, the ROI is selected by another dentist in red boundaries. The third column represents the segmented result by our proposed algorithm. The performance parameters—accuracy, precision, error rate and specificity—are kept same as discussed in Chaps. 3 and 4, and they are computed for all these images. In order to calculate all these parameters for measurement, the confusion matrixes are first calculated for all images for both the ground truth image sets. The confusion matrix for a sample segmented dental radiograph with both ground truth image sets are shown in Tables 5.1 and 5.2 respectively.

So according to the above confusion matrix the accuracy of our segmented result based on ROI of ground truth set-1 is 99.21%, error rate is 0.78%, precision is 90.01% and specificity is 99.56%. The confusion matrix for the same radiographic image and ROI of ground truth set-2 is shown in Table 5.2.

According to the confusion matrix shown in Tables 5.3 and 5.4, the accuracy, precision, error rate and specificity of our segmented result based on ROI ground

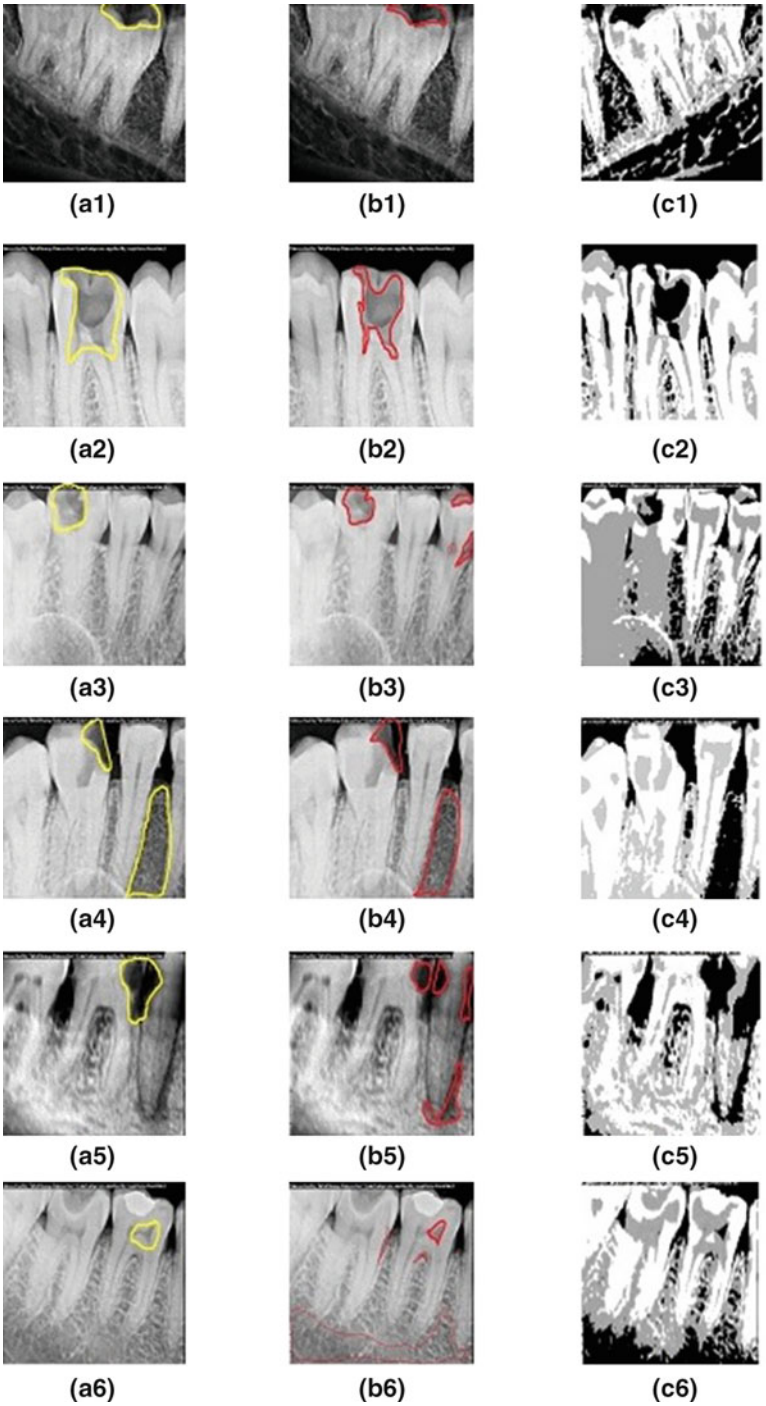

Fig. 5.4 Comparison of segmented image results with the ROIs of two ground truth sets

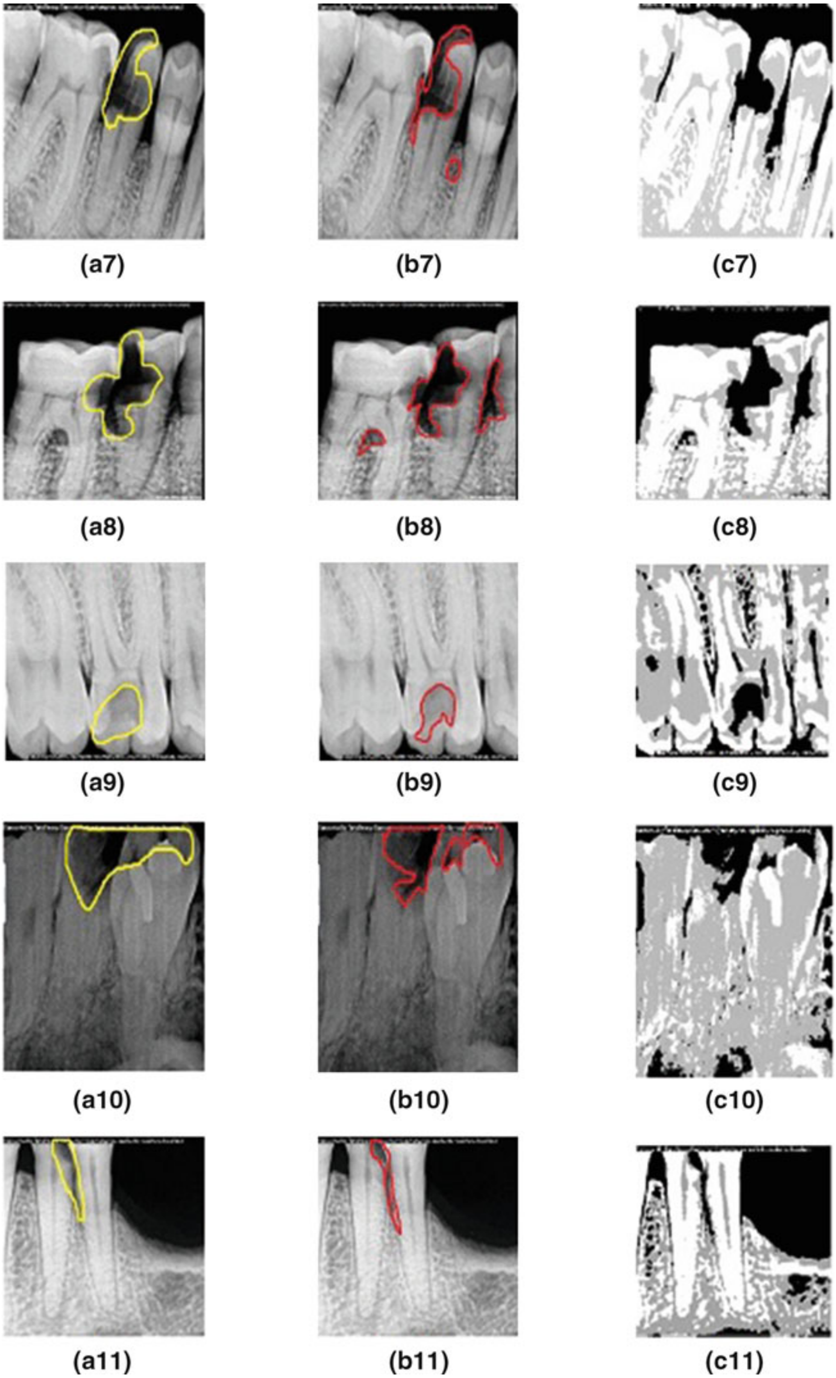

Fig. 5.4 (continued)

Table 5.1 Confusion matrix of a sample radiograph with ROI of ground truth set-1

	Predicted class			
Actual class		Yes	No	Total
	Yes	2605	257	2862
	No	289	66,738	67,027
	Total	2894	66,995	69,889

Table 5.2 Confusion matrix of a sample radiograph with ROI of ground truth set-2

	Predicted class			
Actual class		Yes	No	Total
	Yes	2605	2984	5589
	No	2435	66,738	69,173
	Total	5040	69,722	74,762

Table 5.3 Performance parameters for segmentation of ROI as compared by ground truth set-1

Images	Accuracy	Precision	Error rate	Specificity
1	98.82	65.91	1.17	99.38
2	98.99	91.30	1.00	99.43
3	97.69	68.87	2.30	98.78
4	76.75	12.04	23.24	86.48
5	98.81	90.46	1.18	99.37
6	93.45	63.39	6.54	96.32
7	98.64	84.08	1.35	99.28
8	98.26	73.24	1.73	99.09
9	95.71	78.28	4.28	97.59
10	99.21	90.01	0.78	99.56
11	99.77	96.15	0.22	99.87
12	97.39	48.77	2.60	98.65
13	97.81	88.31	2.18	98.77
14	98.29	70.47	1.70	99.10
15	93.59	56.62	6.40	96.36
Avg. 723 images	97.83	79.54	2.16	98.77

truth set-1 and ground truth set-2 are presented in Tables 5.3 and 5.4, respectively.

Based on the results of performance measures, it can be depicted that the suggested approach is very helpful for the automatic segmentation and analysis of dental radiograph images during the process of endodontic treatment. The results produced by the proposed method were actually validated with respective dentist and were found to be helpful. The average result of 723 images used for analysis are also shown in Tables 5.3 and 5.4. The bar chart of the evaluation measures of interested region with respect to ROI of ground truth set 1 is shown in Fig. 5.5 based on Table 5.3. A total of 723 cases of RVG format-based dental images were also

Table 5.4 Performance parameters for segmentation of ROI as compared by ground truth set-2

Images	Accuracy	Precision	Error rate	Specificity
1	98.12	74.05	1.87	98.98
2	95.97	80.82	4.02	97.93
3	97.65	67.70	2.34	98.73
4	96.21	82.18	3.78	97.98
5	98.28	85.73	1.71	99.05
6	99.49	88.22	0.50	99.75
7	99.90	99.39	0.09	99.96
8	92.66	57.71	7.33	95.76
9	95.40	49.64	4.59	97.53
10	98.41	91.66	1.58	99.20
11	98.81	79.17	1.18	99.46
12	99.13	80.90	0.86	99.62
13	94.18	81.47	5.81	96.45
14	91.89	78.91	3.45	97.65
15	98.61	77.45	1.23	99.10
Avg. 723 images	96.00	66.12	3.99	97.82

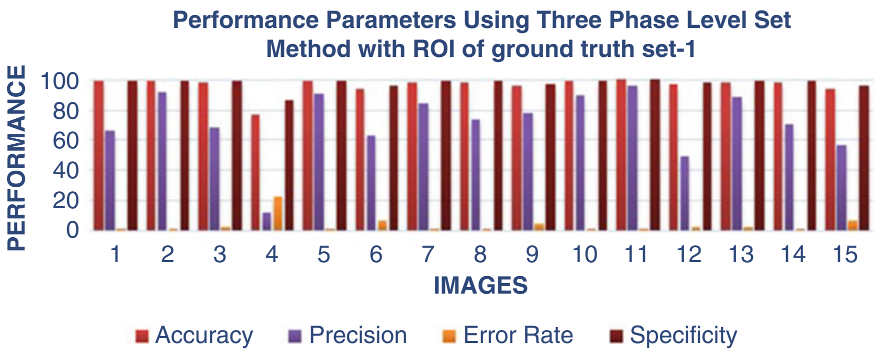

Fig. 5.5 Comparison of parametric evaluation measures for segmentation based on three-phase level set method (ROI of ground truth set-1)

analysed. The average accuracy of 723 data base images was found to be 97.83% with precision of 79.54%, error rate of 2.16% and specificity of 98.77%.

The bar chart of the evaluation measures of interested region with respect to ROI of ground truth set-2 is shown in Fig. 5.6 based on Table 5.4. Average accuracy of 723 data base images was found to be 96.00% with precision of 66.12%, error rate of 3.99% and specificity of 97.82% with respect to ground truth 2, that is, ROI of ground truth set-2.

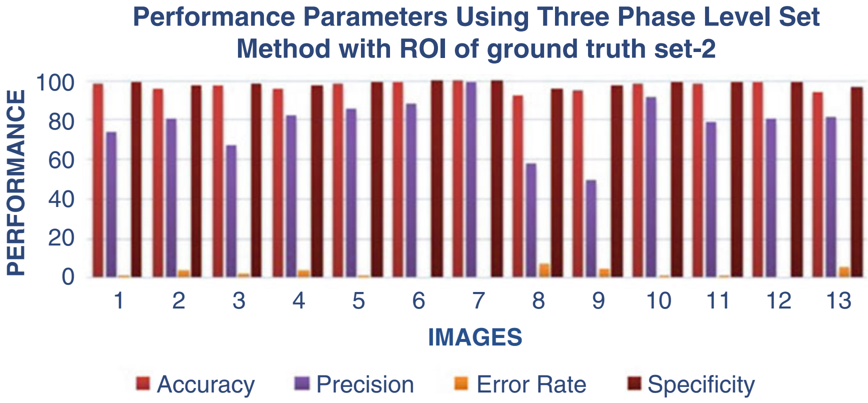

Fig. 5.6 Comparison of parametric evaluation measures for segmentation based on three-phase level set method (ROI of ground truth set-2)

5.6 Discussion and Concluding Remarks

In this chapter, an automated segmentation method based on level set approach for segmenting region of interest from a dental radiographic image is presented. The results produced by the proposed method were compared with the ground truth results obtained with two domain experts. Based on the evaluation measures, the proposed method is found to be very effective in identification of interested region. The proposed method can be useful for assistance to the dental medical practitioners during their endodontic treatment of the tooth. The method can further be evaluated rigorously and can also be integrated in any computer-based diagnostic tool.

Chapter 6
Clustering Techniques for Dental Image Analysis

Analysis of digital dental radiograph plays a key role in oral dentistry and is widely used for detection of dental diseases. Extraction of tooth or teeth, or other important regions plays an important role in identification and diagnosis of diseases. Machine learning techniques, specifically clustering techniques, have contributed actively for preparing model and using it for segmentation [71]. Some popular clustering techniques like K-means, Fuzzy C-means (FCM), and other advance clustering techniques have been investigated in this chapter in this chapter for segmentation of dental radiographs [72]. Similar to level set-based method, clustering-based segmentation is also automated and its results are compared with the other two methods discussed in Chaps. 3 and 4. In this chapter we provide a comparative study of presented methods on various dental problems and its consequences. Clustering can be viewed as the most promising unsupervised learning methods [73, 74].

6.1 K-Means Clustering for Image Segmentation

K-Means clustering is the simple and effective unsupervised learning technique [75]. The algorithm is based on the partition between n number of observations into kth clusters. The methodology takes over after a straightforward and simple approach to order a given informational index through a specific number of bunches (accept k groups) settled from the earlier [76]. The fundamental thought is to characterise k centroids, one for each bunch. These centroids should be set cleverly on account of various area causes distinctive outcome. In this way, the better decision is to place them however much theycould reasonably be expected far from each other. The following stride is to take each direct having a place toward a given informational index and partner it to the closest centroid. Now, we have to refigure k new centroids as barycentres of the groups coming about because of the

K. R. Jain, N. C. Chauhan, *Dental Image Analysis for Disease Diagnosis*,
https://doi.org/10.1007/978-3-030-14136-3_6

past stride. A circle has been created. Subsequently of this circle we may see that the k centroids change their area well ordered until no more changes are observed. At the end the centroids do not move any more. Minimising an objective function known as squared error function given by:

$$J(V) = \sum_{i=1}^{c} \sum_{j=1}^{c_i} \left(\|x_i - v_j\| \right)^2 \tag{6.1}$$

where J is the objective function, c is the cluster centre. x_i is the ith of d-dimensional measured data elements of the cluster, v_j is the d-dimension centre of the cluster j. C_i is represented the number of data points in ith cluster. K-implies grouping calculation utilises iterative refinement to create a last outcome. The calculation information sources are the quantity of groups K and the informational index. The informational collection is a gathering of elements for every information point. The calculations begins with starting evaluations for the K centroids, which can either be arbitrarily produced or haphazardly chosen from the informational index [77].

This algorithm is applied in the following steps: Let $X = \{x_1, x_2 \ldots x_n\}$ is the set of data points and $V = \{v_1, v_2 \ldots v_n\}$ is the set of centres.

Algorithm 6.1 K-Means Clustering
Steps:

1. Choose arbitrarily k objects from K as the initial cluster centres.
2. Calculate the Euclidean distance between each data point and cluster centres.
3. Assign the data point to the cluster centre whose distance from the cluster centre is minimum of all the cluster centres.
4. Recalculate the new cluster centres using

$$V_i = \left(\frac{1}{c_i} \right) \sum_{j=1}^{c_i} x_i \tag{6.2}$$

5. Recalculate the distance between each data point and newly obtained cluster centres.
6. If no data point was reassigned then stop, otherwise repeat from step 3.

The advantages and drawbacks of K-means clustering are mentioned below
Advantages

- Fast, powerful and simple.
- Relatively productive: $O(t_{knd})$, where n is objects, k is groups, d is measurement of each question, and t is cycles. Regularly, k, t, $d << n$.
- Gives best outcome when informational indexes are particular or very much isolated from each other.

Disadvantages

- The learning calculation requires a priori determination of the quantity of bunch focuses.
- The utilisation of exclusive assignment—If there are two exceptionally covering information then k-means will not have the capacity to determine that there are two bunches.
- The learning calculation is not invariant to non-direct changes, that is, with various portrayal of information we get diverse outcomes (information spoken to in type of Cartesian co-ordinates and polar co-ordinates will give distinctive outcomes).
- Euclidean separation measures can unequally weight fundamental elements.
- The learning calculation gives the neighbourhood optima of the squared mistake work.
- Randomly picking the group focus cannot lead us to a productive outcome.
- Applicable just when mean is characterized, that is, comes up short for clear-cut information.
- Algorithm comes up short for non-straight informational index.

Algorithm 6.2 K-Means Clustering for Segmentation of Dental Radiograph
Steps:

1. Take any input dental radiograph image from the given dataset.
2. Apply the shaping effect (variation on the radius and amount strength on the shaping effect) in the given input image.
3. Apply K-–Means segmentation technique to find the cluster index and cluster centre.
4. After K-–Means clustering, the image index is labelled by the cluster index.
5. We apply the Harris Corner detection in image labelled by the cluster index for detecting corner feature.
6. After segmentation image is classified by the three clusters.
7. Results of segmentation are shown in Fig. 6.2.

6.1.1 Experiment and Results

Based on the discussed algorithm various digital dental radiographs were applied with K-Means clustering technique. The steps of this algorithm are shown in Algorithm 6.2. The results obtained based on the application of algorithm are shown in Fig. 6.2. Each column represents the stepwise result of different radiographs. The process of application of radiograph segmentation is also shown graphically in Fig. 6.1. The individual column represents the three different clusters namely cluster 1, 2 and 3 being formed for the purpose of classification in Fig. 6.2d1–d12, e1–e12 and f1–f12 respectively. In Fig. 6.2, 12 different radiographs of various dental problems are considered, and the results are displayed for the purpose of analysing the clustering technique and its effect for the purpose of

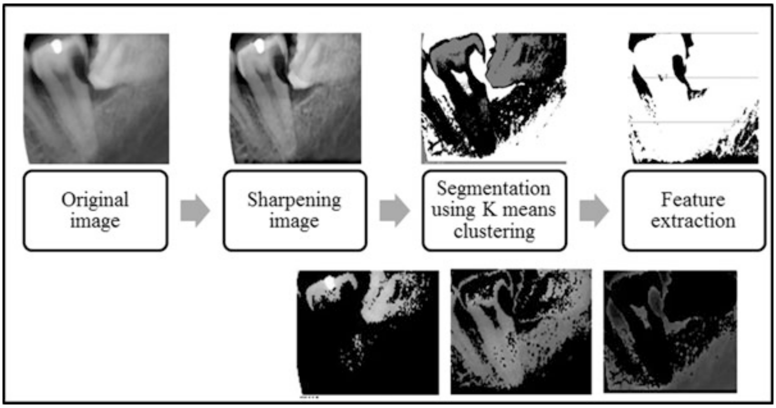

Fig. 6.1 Block diagram of dental radiograph segmentation using K-means clustering

understanding the outcome. The first column represents the original radiograph in Fig. 6.2a1–a12. The next column represents the sharpened radiographs after preprocessing in Fig. 6.2b1–b12. The third column represents the result of segmentation on sharpened radiographs in Fig. 6.2c1–c12.

6.1.2 Validation of Results Using Performance Parameters

The performance parameters as discussed in Chap. 3 are analysed on available radiographic images. Based on the defined parameters for measurement, the confusion matrix for one of the radiographic images and ROI of one of ground truth image (obtained with one expert) is shown in Table 6.1 which is same as that discussed in Table 3.1.

According to the confusion matrix shown in Table 6.1 the accuracy of our segmented result based on ROI of ground truth set-1 is 95.71%, error rate is 4.28%, precision is 78.28% and specificity is 97.59%. The confusion matrix for the same radiographic image and ROI indicated from ground truth set-2 is shown in Table 6.2.

According to the confusion matrix shown in Tables 6.1 and 6.2, the accuracy, precision, error rate and specificity of our segmented result based on ROI of ground truth set-1 and ground truth set-2 are presented in Tables 6.3 and 6.4 respectively. The algorithm was evaluated on 723 database images and simulation results of all RVG images comprising of different dental problems. The results obtained were also validated with same medical practitioner (refer the certificates of medical practitioners in the Appendix), the results are found to be useful during their practice.

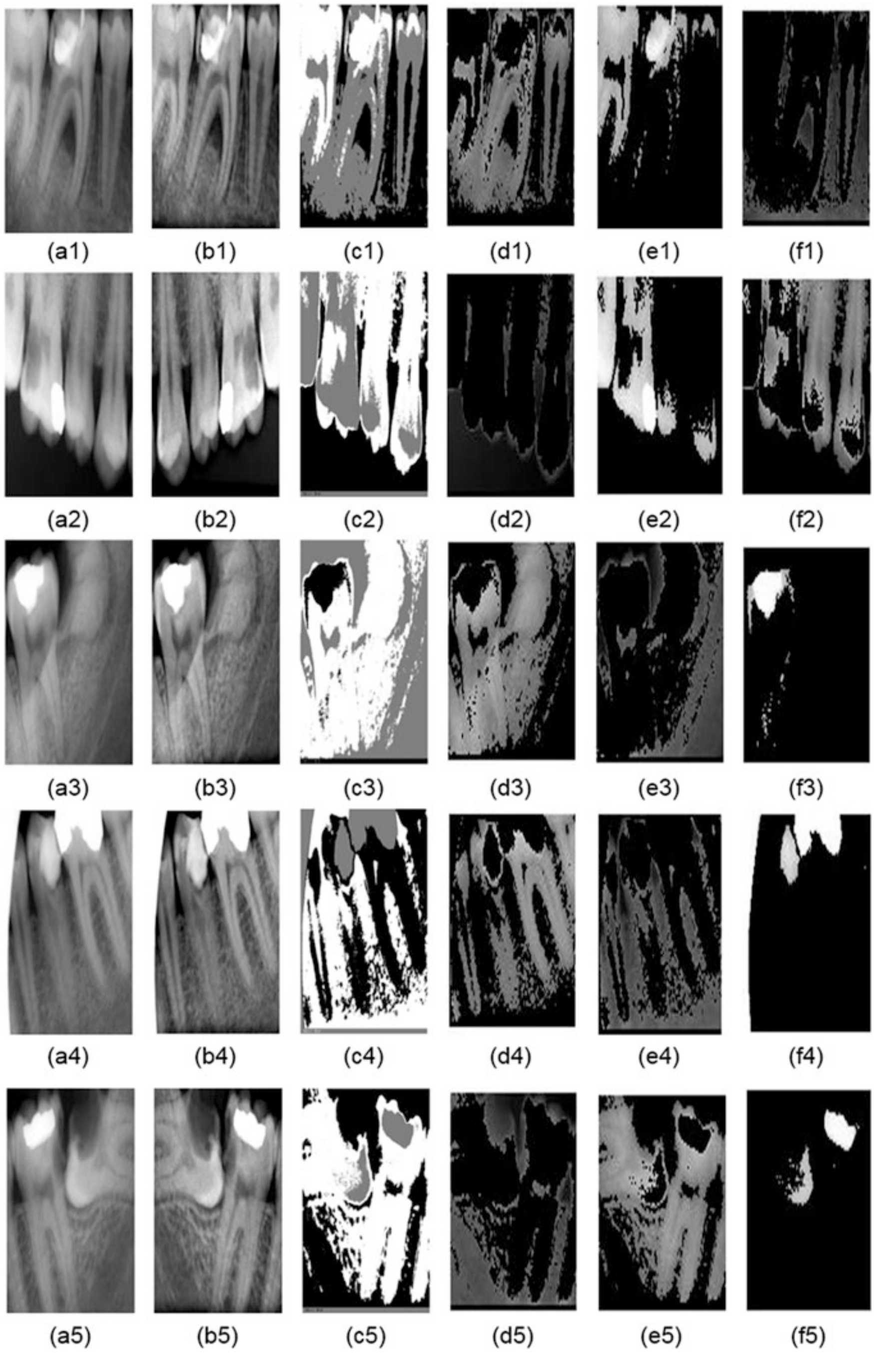

Fig. 6.2 K-means clustering technique for segmentation and clustering

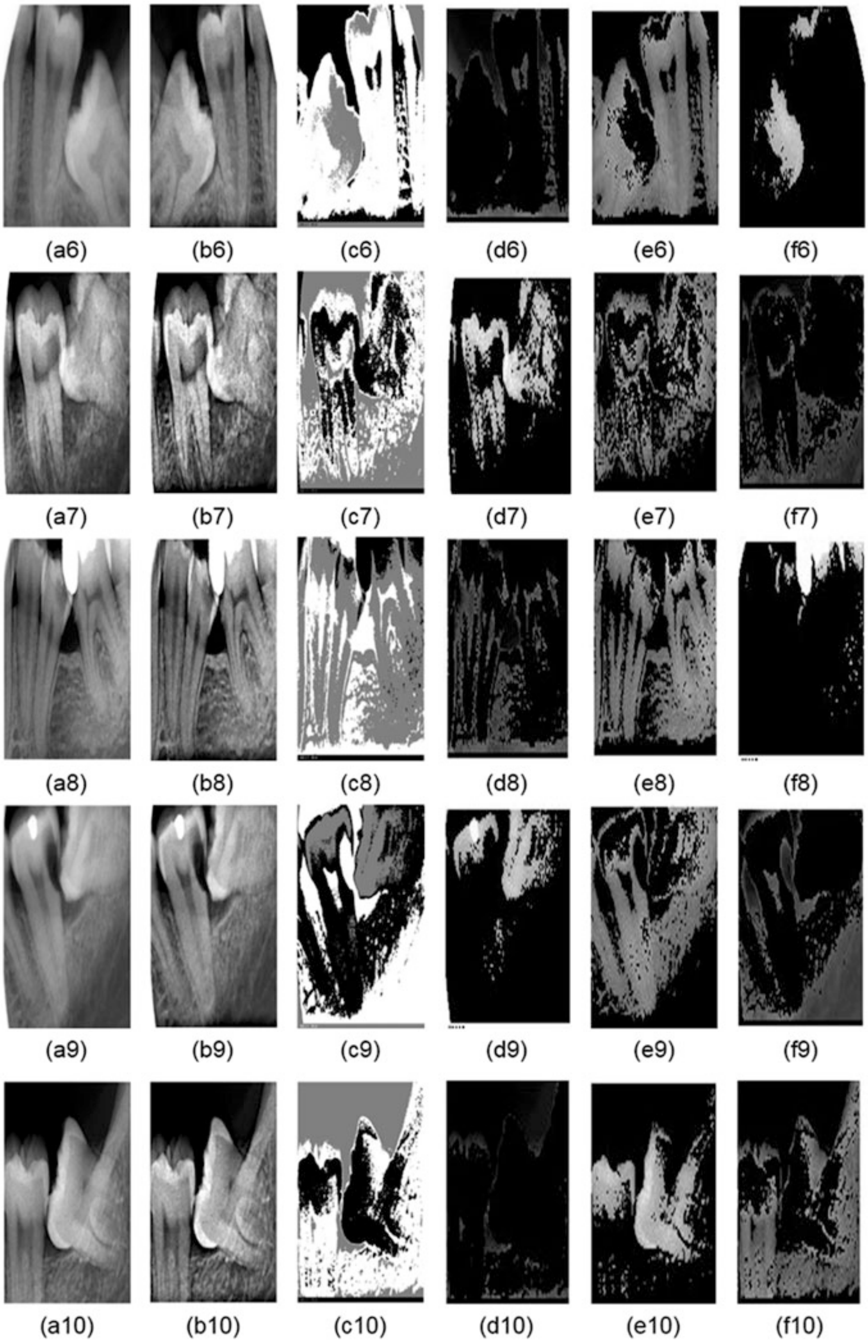

Fig. 6.2 (continued)

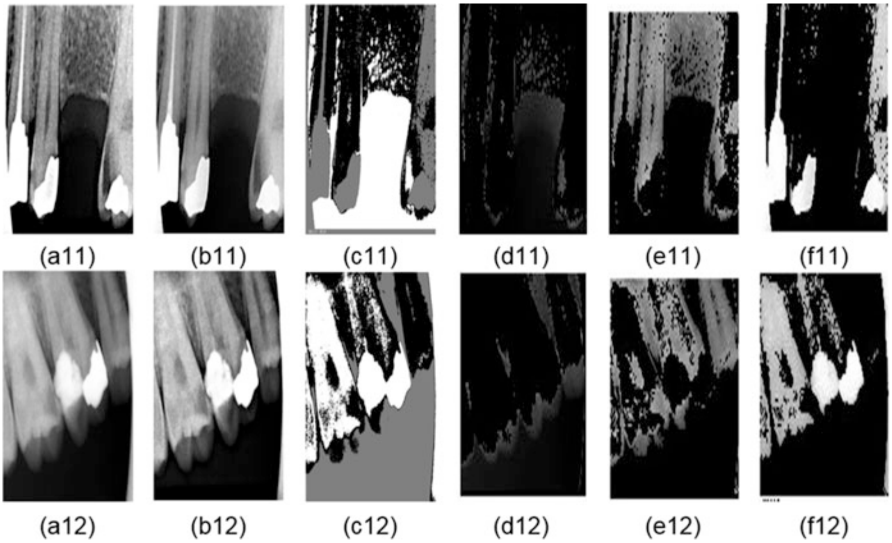

Fig. 6.2 (continued)

Table 6.1 Confusion matrix of a sample radiograph image compared with ROI of ground truth set-1

	Predicted class			
Actual class		Yes	No	Total
	Yes	5439	1472	6911
	No	1509	61,133	62,642
	Total	6948	62,605	69,553

Table 6.2 Confusion matrix of the sample radiograph image compared with ROI of ground truth set-2

	Predicted class			
Actual class		Yes	No	Total
	Yes	5439	1502	6941
	No	1290	61,133	62,423
	Total	6729	62,635	69,364

The bar chart summarising the evaluation measures of K-Means technique w.r.t. ROI of ground truth image set-1 and ROI of ground truth image set-2 is shown in Figs. 6.3 and 6.4 respectively. Average accuracy of 723 database images was found to be 97.83% with precision of 79.54%, error rate of 2.16%, recall of 81.08% and specificity of 98.77% w.r.t. ROI of ground truth image set-1. Average accuracy of 723 data base images was found to be 96.4% with precision of 68.7%, error rate of 3.59%, recall of 67.67% and specificity of 98.14% w.r.t. ROI of ground truth image set-2.

Table 6.3 Performance parameters for ROI indicated in ground truth image set-1 using K-means clustering

Images	Accuracy	Precision	Error rate	Recall	Specificity
1	91.54	65.91	1.17	67.09	99.38
2	94.34	91.3	1	92.2	99.43
3	98.39	68.87	2.3	69.46	98.78
4	96.88	90.46	1.18	90.26	99.37
5	91.83	63.39	6.54	64.37	96.32
6	95.62	84.08	1.35	84.52	99.28
7	94.31	73.24	1.73	73.51	99.09
8	92.82	78.28	4.27	78.81	97.59
9	93.26	90.01	0.78	91.02	99.56
10	91.46	96.15	0.22	96.56	99.87
11	89.82	48.77	2.6	49.16	98.65
12	91.14	88.31	2.18	88.57	98.77
13	96.44	70.47	1.7	71.05	99.1
14	93.56	56.66	6.4	59.11	96.36
15	92.71	58.68	4.34	70.65	97.89
Avg. 723 images	97.83	79.54	2.16	81.08	98.77

Table 6.4 Performance parameters for ROI indicated in ground truth image set-2 using K-means clustering

Image no.	Accuracy	Error rate	Specificity	Precision	Recall
1	92.43	00.26	99.79	85.05	95.30
2	93.59	01.71	99.05	85.73	86.60
3	98.27	02.34	98.73	67.70	69.32
4	97.02	07.33	95.76	57.71	60.26
5	92.01	04.59	97.53	49.64	50.87
6	95.87	04.02	97.93	80.82	78.36
7	94.89	07.24	96.47	51.68	46.60
8	93.1	01.87	98.98	74.05	75.74
9	93.8	03.30	98.28	63.50	63.02
10	92.03	05.49	97.07	30.23	31.25
11	90.9	06.40	96.93	29.09	25.60
12	91.54	03.78	97.98	82.18	80.79
13	97.01	02.23	98.91	65.55	62.83
14	93.04	01.58	99.20	91.66	90.21
15	97.61	02.04	98.97	78.90	64.53
Avg. 723 images	96.40	3.59	98.14	68.71	67.67

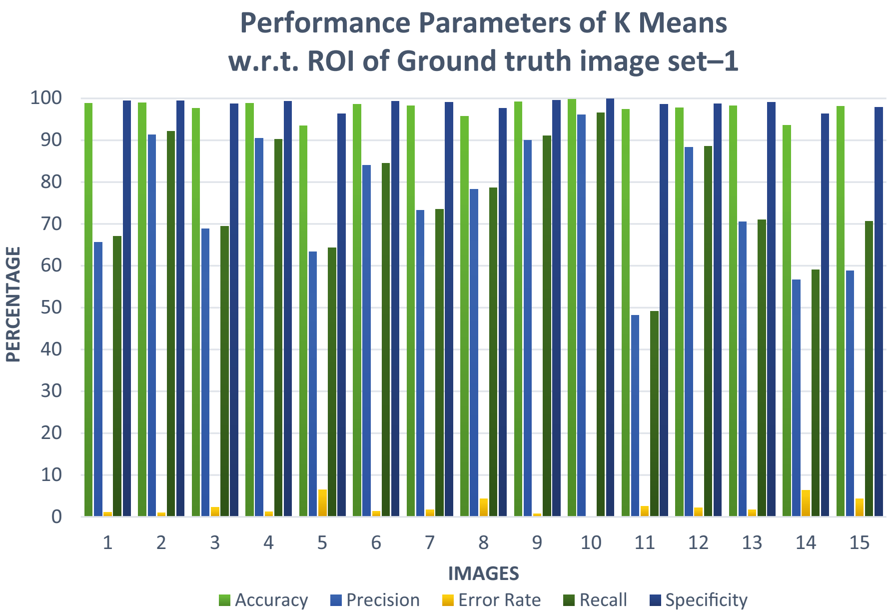

Fig. 6.3 Parametric evaluation measures of K-means w.r.t. ROI of ground truth image set-1

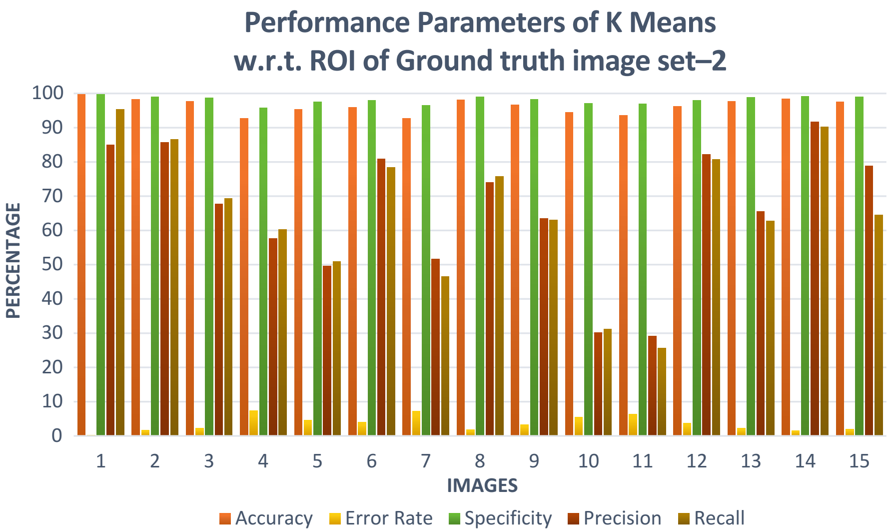

Fig. 6.4 Parametric evaluation measures of K-means w.r.t. ROI of ground truth image set-2

6.2 Fuzzy C-Means Clustering for Segmentation of Dental Radiographs

The foundation of fuzzy collection theory, introduced the idea of uncertainty of belonging described by a membership function [78].

Clustering can be further classified as hard clustering and soft clustering. Fuzzy C-means (FCM) is the clustering assign that one piece of data which may belong to more than one cluster [79]. FCM algorithm attempts to partition a finite collection of elements $X = \{x_1, x_2, \ldots x_N. \ldots\}$ into a collection of c fuzzy clusters with respect to some given criteria. The algorithm is based on minimisation of the objective function.

$$J_m = \sum_{i=1}^{N} \sum_{j=1}^{C} u_{ij}^m \left\| x_i - c_j \right\|^2 \tag{6.3}$$

where J is the intra-cluster similarity to be minimised, m is any real number greater than 1, u_{ij} is the degree of membership of x_i in the cluster j, x_i is the ith of d-dimensional measured data, c_j is the d-dimension centre of the cluster, and ||*|| is any norm expressing the similarity between any measured data and the centre. $\|x_i - c_k\|$ is the distance from point i to other current centres j. $\|x_i - c_j\|$ is the distance from point i to current centres j.

$$u_{ij} = \frac{1}{\sum \left(\frac{\|x_i - c_j\|}{\|x_i - c_k\|} \right)^{\frac{2}{m-1}}} \tag{6.4}$$

Algorithm 6.3 Fuzzy C-Means Clustering
Steps:

1. Initiate $U = [u_{ij}]$ matrix, $U(0)$ and the data point $x_i = (1, 2\ldots N)$.
2. At k-step calculate the centre's vectors $C(k) = [c_j]$ with $U(k)$.

$$c_j = \frac{\sum_{i=1}^{N} u_{ij} * x_i}{\sum_{i=1}^{N} u_{ij}^m} \tag{6.5}$$

3. Update $U(k)$, $U(k + 1)$

$$u_{ij} = \frac{1}{\sum \left(\frac{\|x_i - c_j\|}{\|x_i - c_k\|} \right)^{\frac{2}{m-1}}} \tag{6.6}$$

4. If $\|U^{(k+1)} - U^{(k)}\| < \epsilon$ then stop, otherwise return to step 2.

The algorithm for performing segmentation of radiograph using fuzzy C-Means clustering is presented as Algorithm 6.3. The steps of this algorithm are also produced in the form of a block diagram and presented in Fig. 6.5. The advantages and drawbacks of this technique are listed as follows:

Advantages

- FCM provides best outcome for covered informational index and nearly better then k-implies calculation.
- Unlike k-means where data point must exclusively belong to one cluster center here data point is assigned membership to each cluster center as a result of which data point may belong to more then one cluster center.

Disadvantages

- A priori particular of the quantity of groups.
- With lower estimation of β we show signs of improvement result yet to the detriment of more number of cycles.
- Euclidean separation measures can unequally weight hidden components.

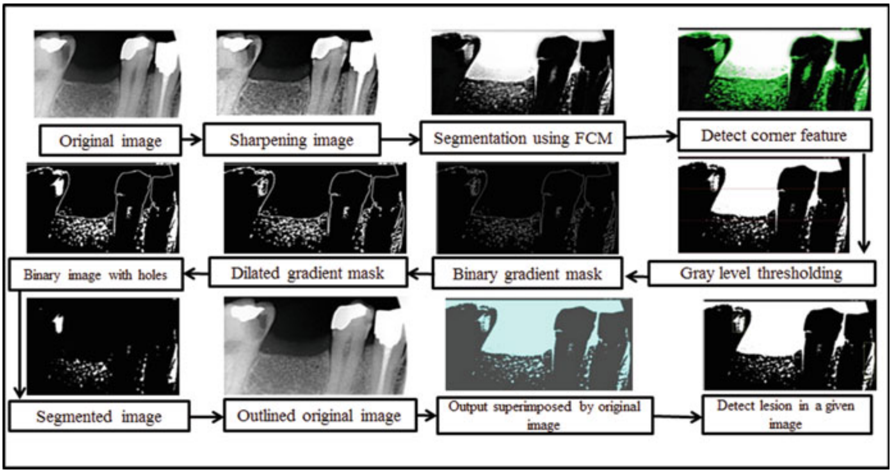

Fig. 6.5 Block diagram of segmenting dental radiograph image using FCM clustering

Algorithm 6.4 Fuzzy C-Means Clustering for Segmentation of Dental Radiograph
Steps:

1. Take any input dental radiograph image from the given dataset.
2. Using FCM segment the radiograph image in the following manner.
   (a) Choose random centroid at least two.
   (b) Compute membership matrix according to Eq. (6.6).
   (c) Calculate the "*c*" cluster centres according to Eq. (6.5).
3. The radiograph image index is labelled by the cluster index.
4. We apply Harris Corner detection in image labelled by the cluster index for detecting corner feature.
5. On the corner detected images apply dilated gradient masking technique for the purpose of separation of cyst from the radiograph.
6. Apply grey level thresholding to the gradient masked image and the radiograph image is then divided to three parts as shown in Fig. 6.5.
7. The final output radiograph is then superimposed on the original image to separate the cyst from the given radiograph.

6.2.1 Experiment and Results

Based on the discussed algorithm various digital dental radiographs were applied with FCM clustering technique. The steps of this algorithm are shown in Algorithm 6.4. The results obtained based on the application of algorithm are shown in Fig. 6.6. Each column represents the stepwise result of different radiographs. In Fig. 6.6, 12 different radiographs of various dental problems are considered, and the results are displayed for the purpose of analysing the FCM clustering technique and its effect for the purpose of understanding the outcome. The first column of Fig. 6.6 represents the original radiograph from ((a1)–(a12)). The next column of Fig. 6.6 represents the segmented radiograph using FCM from ((b1)–(b12)). The third column of Fig. 6.6 represents the result of corner detection on segmented radiographs from ((c1)–(c12)). The fourth column represents the dilated gradient masked radiographs. The next column of Fig. 6.6 represents the grey level thresholded radiograph from ((d1)–(d12)). At last, the resultant radiograph is superimposed on the original radiograph to identify the cyst in Fig. 6.6 from ((e1)–(e12)).

6.2.2 Validation of Results Using Performance Parameters

The performance parameters as discussed in Chap. 3 are analysed on available radiographic images. Based on the defined parameters for measurement, the

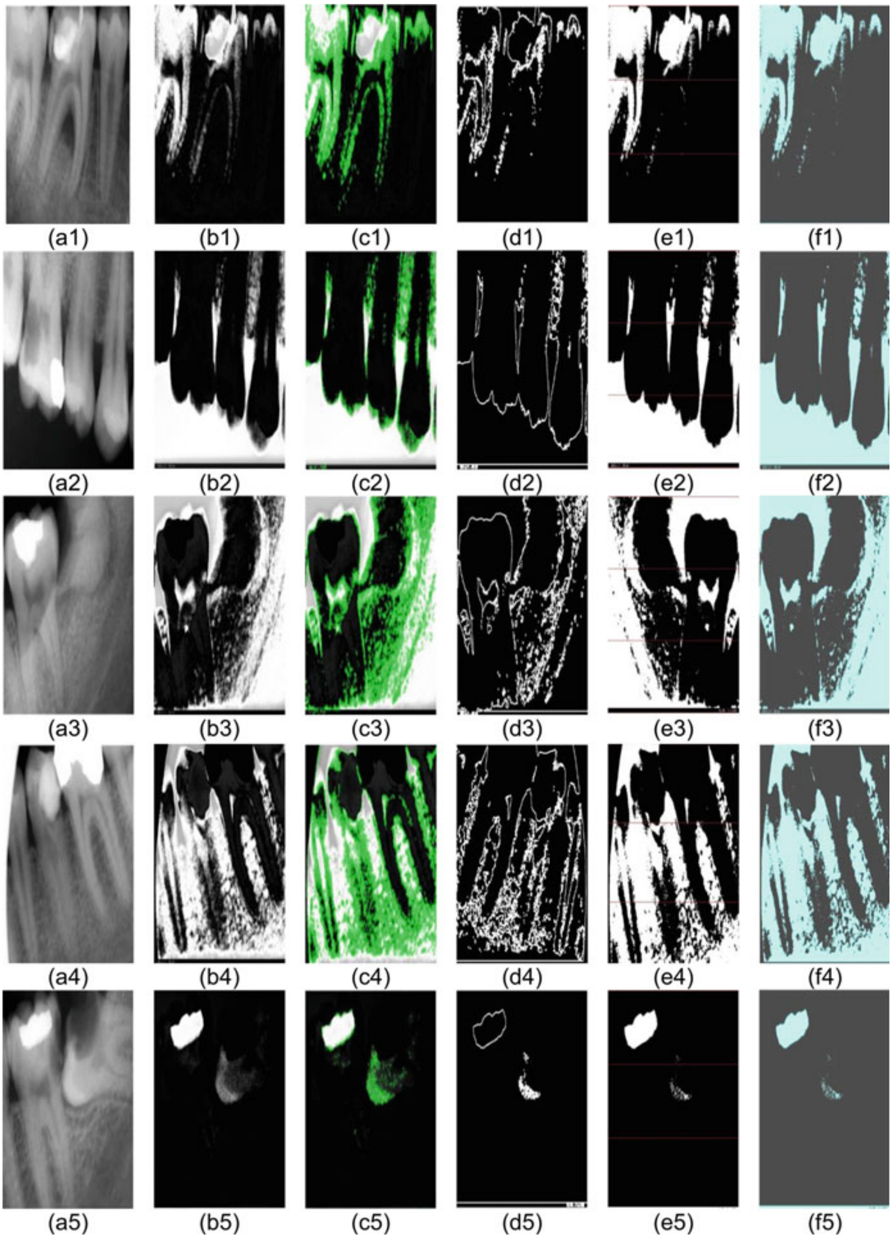

Fig. 6.6 FCM clustering for segmentation

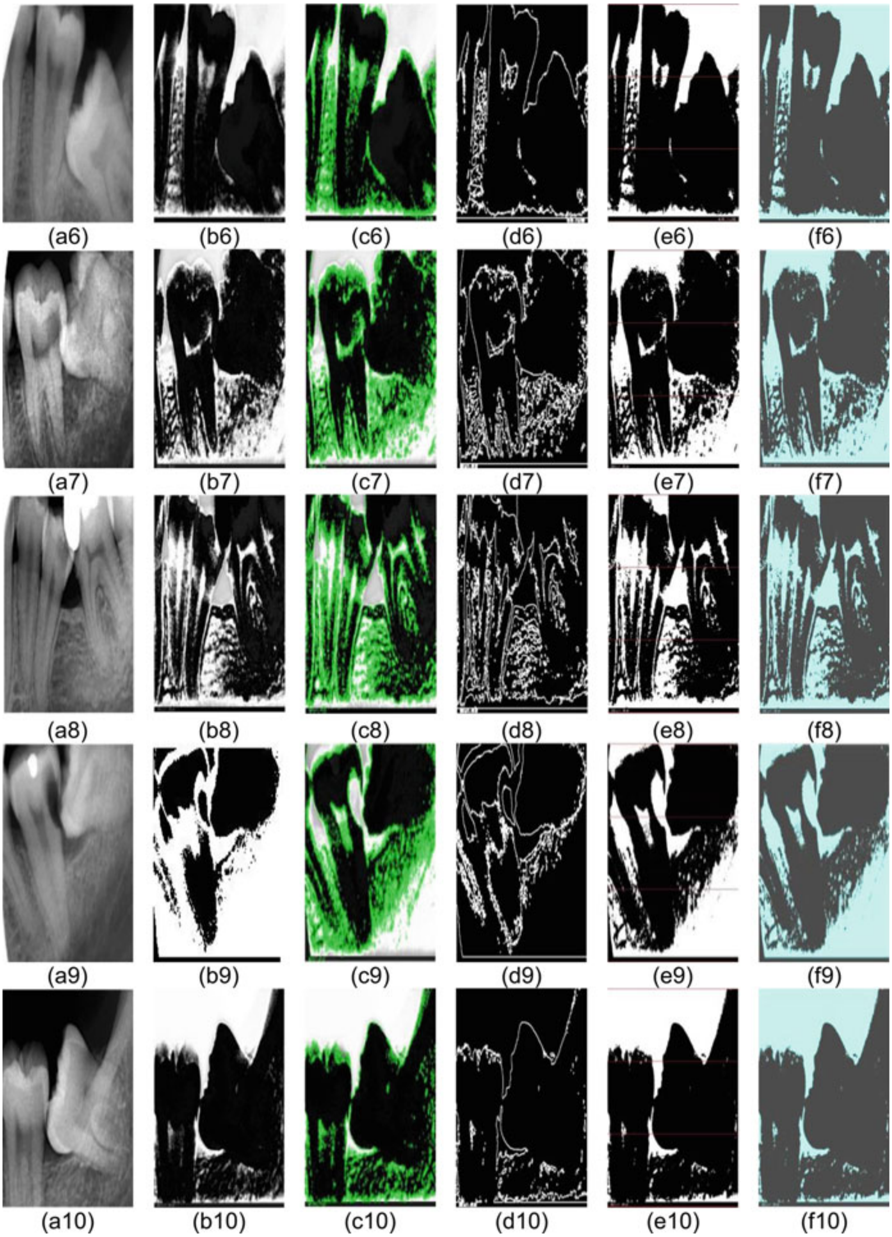

Fig. 6.6 (continued)

confusion matrix for one of the radiographic images and ROI of ground truth set-1 as shown in Table 6.5 which is same as that discussed in Table 3.1.

So according to the above confusion matrix the accuracy of our segmented result based on ROI of ground truth set-1 is 95.71%, error rate is 4.28%, precision is

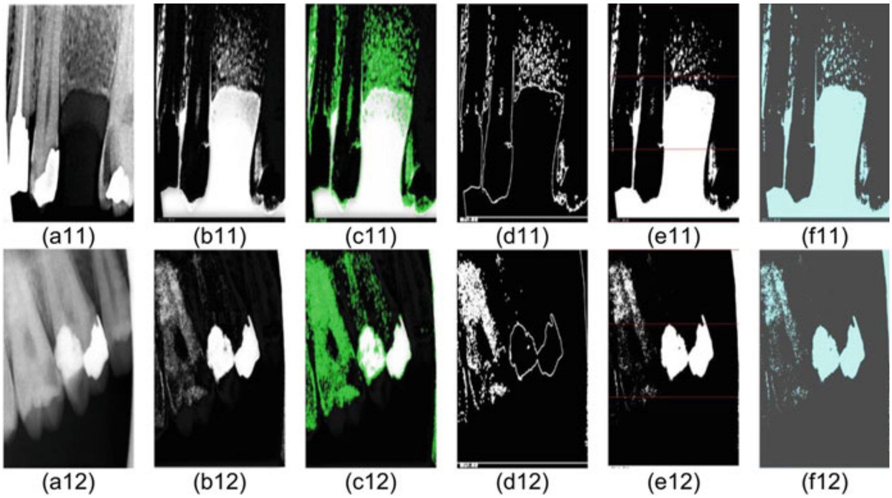

Fig. 6.6 (continued)

Table 6.5 Confusion matrix of a sample image for ROI of ground truth set-1

	Predicted class			
Actual class		Yes	No	Total
	Yes	5439	1472	6911
	No	1509	61,133	62,642
	Total	6948	62,605	69,553

Table 6.6 Confusion matrix of the sample image for ROI of ground truth set-2

	Predicted class			
Actual class		Yes	No	Total
	Yes	5439	1502	6941
	No	1290	61,133	62,423
	Total	6729	62,635	69,364

78.28% and specificity is 97.59%. The confusion matrix for the same radiographic image and ROI of ground truth set-2 is shown in Table 6.6.

According to the confusion matrix shown in Tables 6.5 and 6.6, the accuracy, precision, error rate and specificity of our segmented result based on ROI of ground truth set-1 and set-2 is presented in Tables 6.7 and 6.8. The proposed process is being applied on 723 database images and simulation results of all RVG images comprising of dental problems were summarised. The results so obtained were also shown to the medical practitioners.

The bar chart summarising the evaluation measures of FCM technique w.r.t. ROI of ground truth set-1 and ROI of ground truth set-2 is shown in Figs. 6.7 and 6.8. Average accuracy of 723 data base images was found to be 98.12% with precision of 80.48%, error rate of 1.87%, recall of 82.04% and specificity of 98.94% w.r.t. ROI of ground truth set-1.

Table 6.7 Performance parameters for ROI indicated of ground truth set-1 and FCM clustering technique

Image no.	Accuracy	Precision	Error rate	Recall	Specificity
1	97.1	67.81	1.11	66.89	99.18
2	95.61	91.25	1.12	91.1	99.41
3	99.04	69.87	2.28	69.16	98.79
4	96.11	54.89	6.31	58.15	96.31
5	91.01	89.91	1.16	89.88	99.47
6	96.34	64.41	6.41	65.38	95.42
7	95.24	83.18	1.31	83.63	99.28
8	93.05	74.11	1.61	74.1	99.1
9	92.56	78.18	3.98	77.89	96.45
10	93.62	89.88	0.69	91.2	99.37
11	99.04	95.99	0.18	96.15	99.78
12	92.84	47.79	2.78	50.01	98.56
13	97.96	86.13	2.09	87.45	98.67
14	99.75	71.1	1.68	70.97	99.3
15	97.81	80.45	1.78	81.99	98.64
Avg. 723 images	97.21	79.46	1.85	81.97	97.98

Table 6.8 Performance parameters for ROI indicated of ground truth set-2 and FCM clustering technique

Image no.	Accuracy	Precision	Error rate	Recall	Specificity
1	96.89	84.89	0.29	97.21	99.68
2	94.16	85.61	1.52	87.17	99.03
3	98.79	68.61	2.36	69.46	97.83
4	95.76	56.68	6.35	60.86	96.75
5	91.84	49.54	4.39	51.25	96.58
6	95.9	79.98	4.21	79.36	97.97
7	94.8	52.1	6.48	45.96	96.57
8	92.3	73.88	1.67	74.75	98.99
9	91.45	64.13	3.29	63.27	98.38
10	92.45	31.33	5.47	30.27	96.7
11	98.76	30.09	6.48	26.65	97.39
12	91.9	81.18	3.68	79.8	98.97
13	96.58	64.76	2.13	63.82	99.18
14	98.79	92.54	1.85	91.02	99.18
15	97.68	70.18	1.24	79.58	97.54
Avg. 723 images	97.45	68.15	2.48	64.65	98.74

Average accuracy of 723 database images was found to be 97.40% with precision of 66.51%, error rate of 2.84%, recall of 65.64% and specificity of 97.84% w.r.t. ROI of ground truth set-2.

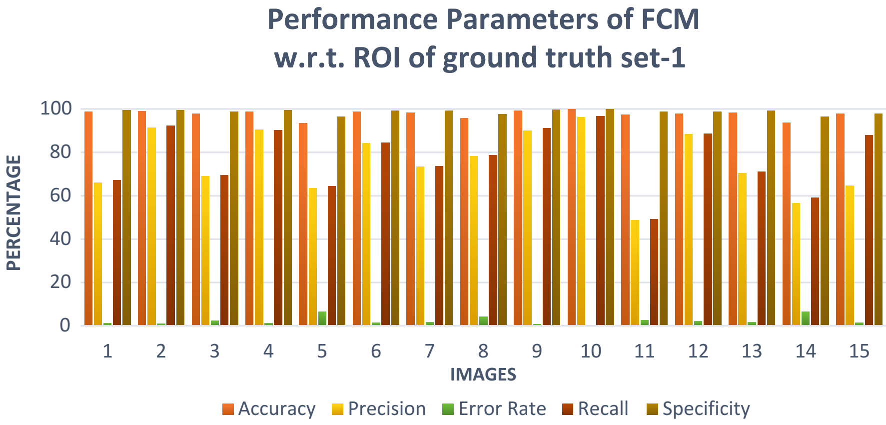

Fig. 6.7 Parametric evaluation measures of FCM w.r.t. ROI of ground truth set-1

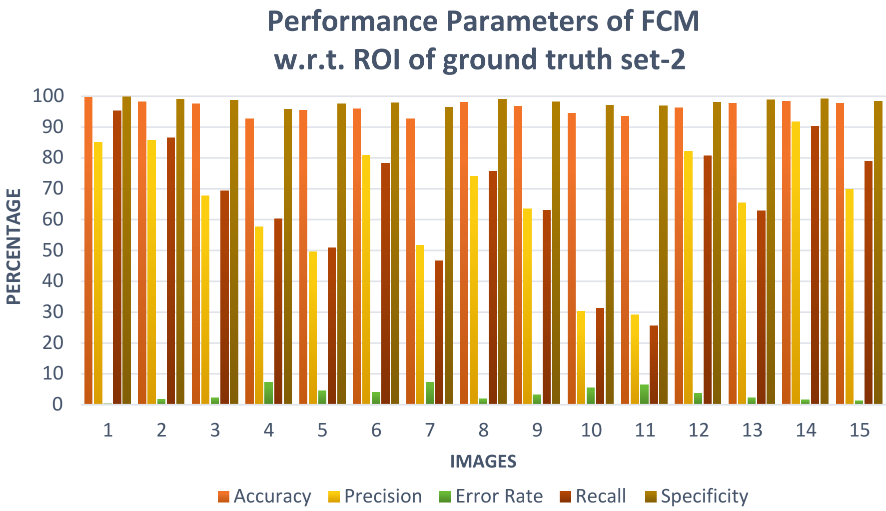

Fig. 6.8 Parametric evaluation measures of FCM w.r.t. ROI of ground truth set-2

6.3 Kernel Fuzzy C-Means Clustering

The Kernel Fuzzy C-Means (KFCM) calculation adds part data to the customary Fuzzy C–Means calculation and it conquers the drawback that FCM calculation cannot deal with the little contrasts between bunches [71]. The portion technique maps nonlinearly the information space into a high dimensional component. We construct a kernel version of FCM (KFCM), where the original Euclidian distance in FCM is replaced with kernel-induced distance measures as shown in Eqs. 6.7 and 6.8 [80]:

$$d(x,y) = \|\varphi(x) - \varphi(y)\| \tag{6.7}$$

$$d(x,y) = \sqrt{k(x,x) - 2k(x,y) + k(y,y)} \tag{6.8}$$

where φ is a nonlinear function which maps from the input space X to a new space F with higher or even infinite dimensions. Kernel function which is defined as the inner product in the new space F with x and y as the input space [81].

$$k(x,y) = \varphi(x)\varphi(y) \tag{6.9}$$

A nonlinear map is defined as

$$\varphi : x \rightarrow \varphi(x) \in F \quad \text{as well as} \quad x \in X \tag{6.10}$$

where X indicate Data space, while F indicates the Transformed feature space with higher even infinite dimension. The KFCM minimises the following objective function:

$$J_m = \sum_{i=1}^{c} \sum_{k=1}^{n} u_{ij}^{m} \|\varphi(x_k) - \varphi(v_i)\|^2 \tag{6.11}$$

where $K(x_k, v_i) = 1$

$$K(x_k, x_k) + k(v_i, v_i) - 2k(x_k, v_i) \tag{6.12}$$

Kernel functions: for Gaussian kernel

$$k(x,y) = \exp\left(-\frac{\|x-y\|^2}{\sigma^2}\right) \tag{6.13}$$

Combine Eqs. 6.11 and 6.13 can be rewritten as:

$$J_m = (U,V) = 2\sum_{i=1}^{c} \sum_{k=1}^{n} u_{ik}^{m}(1 - k(x_k, V_i)) \tag{6.14}$$

Algorithm 6.5 of Kernel Fuzzy C-Means Clustering
Steps:

1. Fix c, $t_{\max}$, Initiate $U = [u_{ij}]$ matrix, $U(0)$.
2. For $t = 1, 2 \ldots t_{\max}$. Update all prototypes v_i as

$$v_i = \frac{\sum_{k=1}^{n} u_{ik}^m k(x_k, v_i)}{\sum_{k=1}^{n} u_{ik}^m k(x_k, v_i)} \tag{6.15}$$

3. Update all memberships value. $U(t)$, $U(t+1)$

$$u_{ik} = \frac{\left(1 - k\left(x_k V_j\right)\right)^{-1/_{m-1}}}{\sum_{j=1}^{c} \left(1 - k\left(x_k, V_j\right)\right)^{-1/_{m-1}}} \tag{6.16}$$

4. Stop condition If $\|U(t+1) - U(t)\| < \epsilon$.

   The advantages of KFCM clustering technique are enlisted below.
   Advantages:

- We can obtain a linearly separable hyperplane in the high-dimensional, or even in an infinite feature space.
- They can identify clusters with arbitrary shapes.
- Kernel-based clustering algorithms have the capability of dealing with noise and outliers.
- There is no requirement for prior knowledge to determine the system topological structure.
- The kernel matrix can provide the means to estimate the number of clusters.

Algorithm 6.6 Kernel Fuzzy C-Means for Segmentation and Clustering of Dental Radiograph
Steps:

1. Choose the kernels for the input dental radiograph image.
2. Using KFCM segment the radiograph by following steps:
   (a) Evaluate the membership of pixels.
   (b) Compute the successive centres.
   (c) Repeat the steps iteratively until no new cluster centres are found.
3. Apply grey level thresholding on segmented radiograph.
4. Then apply binary gradient mask on thresholded radiograph.
5. Later on, to highlight the sharp edges dilated gradient mask is used.
6. Now the radiograph is Binarized and then again segmented to highlight the cyst in the outlined original radiograph. As shown in Fig. 6.9.

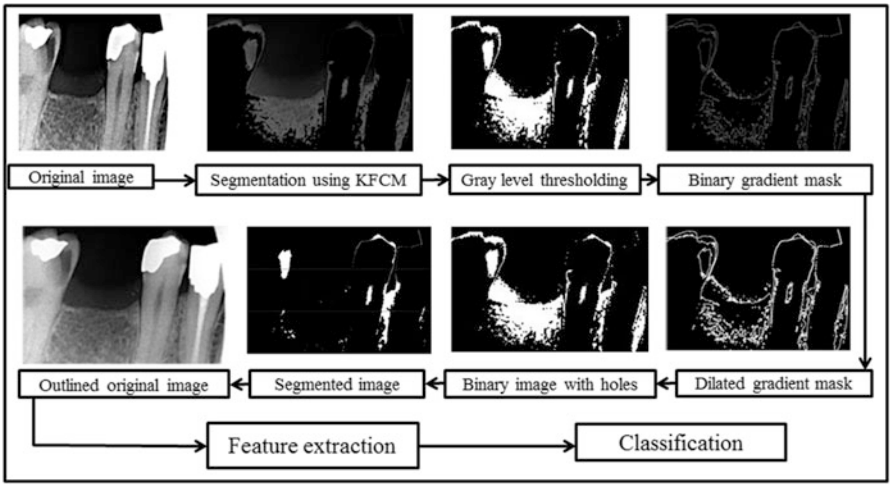

Fig. 6.9 Block diagram of segmentation and classification using Kernel FCM clustering

6.3.1 Experiment and Results

Based on the discussed Algorithm 6.6 various digital dental radiographs were applied with KFCM clustering technique and the results so obtained are shown in Fig. 6.10. Each column represents the stepwise result of each patient as discussed in the block diagram Fig. 6.9. In Fig. 6.10, 12 different radiographs of various dental problems are considered, and the results are displayed for the purpose of analysing the KFCM clustering technique and its effect for the purpose of understanding the outcome. The first column of Fig. 6.10 represents the original radiograph from ((a1)–(a12)). The second column of Fig. 6.10 represents the segmented radiograph using KFCM from ((b1)–(b12)). The next column of Fig. 6.10 represents the grey level thresholded radiograph from ((c1)–(c12)). The fourth column of Fig. 6.10 represents the dilated gradient masked radiographs from ((d1)–(d12)). The next column of Fig. 6.10 represents the segmented radiographs from ((e1)–(e12)). The last column of Fig. 6.10 represents the radiograph outlined with red line showing the cyst from ((f1)–(f12)).

6.3.2 Validation of Results Performance Parameters

The performance parameters as discussed in Chap. 3 are analysed on available radiographic images. Based on the defined parameters for measurement, the confusion matrix for one of the radiographic images and ROI of ground truth set-1 as shown in Table 6.9 which is same as that discussed in Table 3.1.

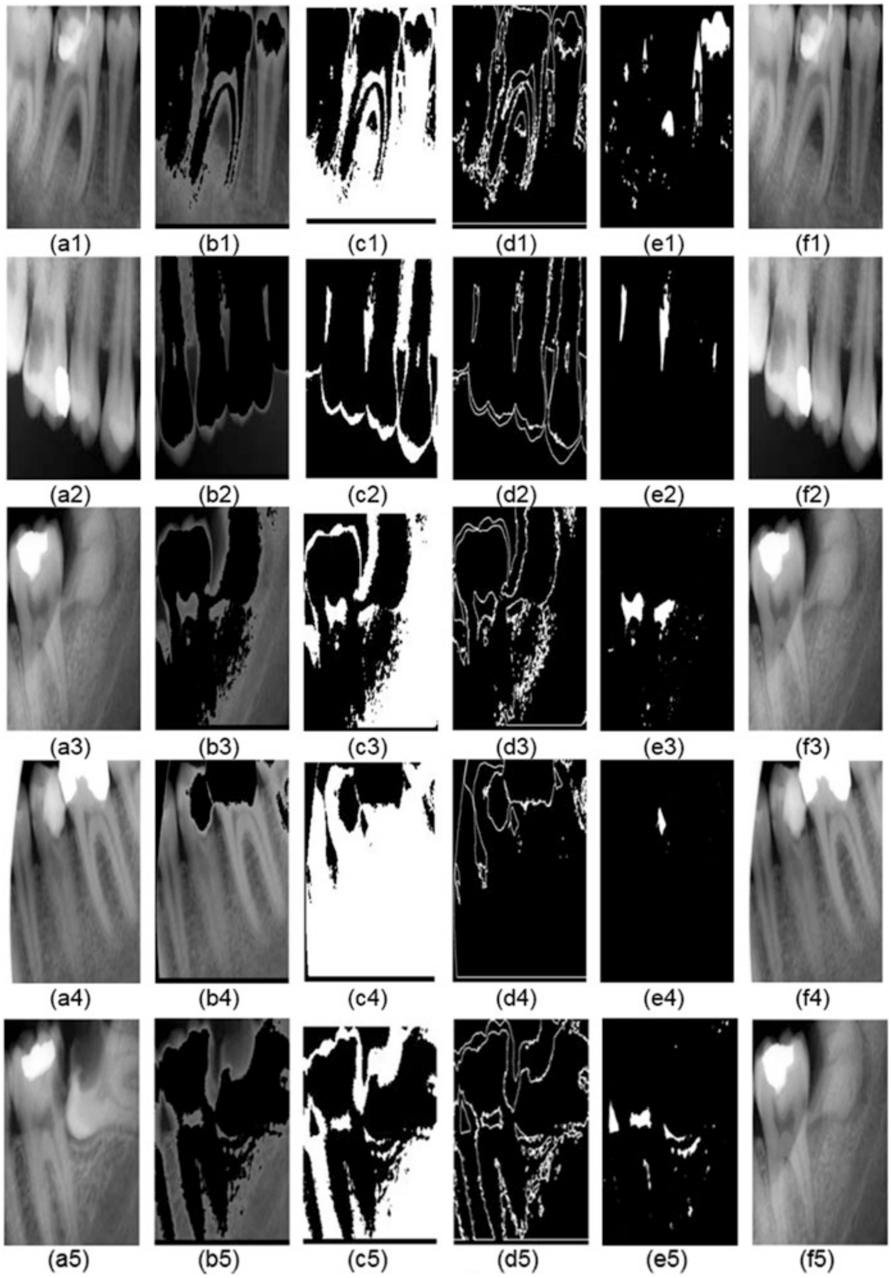

Fig. 6.10 KFCM clustering technique for segmentation

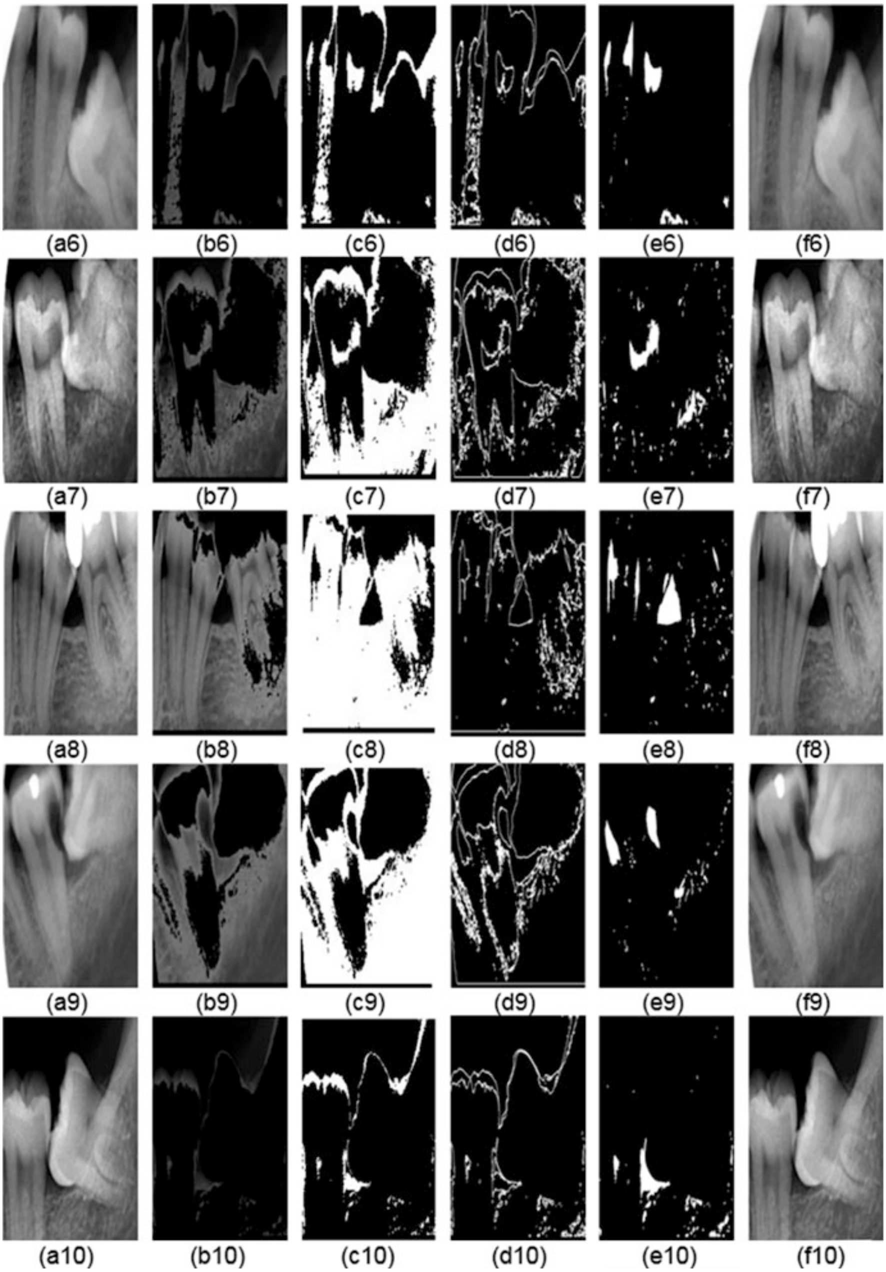

Fig. 6.10 (continued)

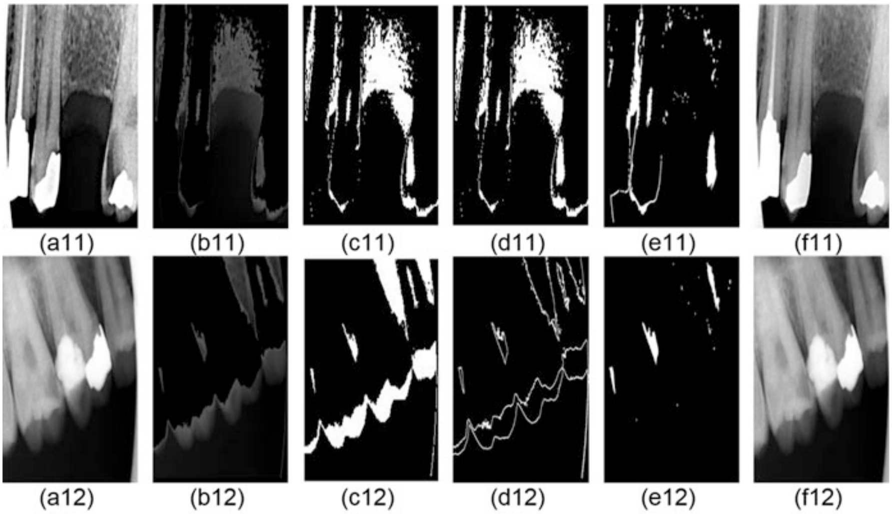

Fig. 6.10 (continued)

Table 6.9 Confusion matrix of a sample radiograph image compared with ROI form its ground truth set-1

	Predicted class			
Actual class		Yes	No	Total
	Yes	5439	1462	6901
	No	1509	61,133	62,642
	Total	6948	62,595	69,543

Table 6.10 Confusion matrix of a sample radiograph image compared with ROI form its ground truth set-2

	Predicted class			
Actual class		Yes	No	Total
	Yes	5439	1532	6971
	No	1487	61,133	62,620
	Total	6926	62,665	69,591

So according to the above confusion matrix the accuracy of our segmented result based on ROI of ground truth set-1 is 95.71%, error rate is 4.28%, precision is 78.28% and specificity is 97.59%. The confusion matrix for the same radiographic image and ROI of ground truth set-2 is shown in Table 6.10.

According to the confusion matrix shown in Tables 6.9 and 6.10, the accuracy, precision, error rate and specificity of our segmented result based on ROI of ground truth set-1 and ROI of ground truth set-2 is presented in Tables 6.11 and 6.12. The proposed process is being applied on 723 database images and simulation results of all RVG images comprising of dental problems are summarised. The results obtained were also validated with the medical practitioners.

Table 6.11 Performance parameters for ROI indicated in ground truth set-1 using KFCM clustering

Image no.	Accuracy	Precision	Error rate	Recall	Specificity
1	94.53	65.91	1.17	67.09	99.38
2	95.83	91.3	1	92.2	99.43
3	98.64	68.87	2.3	69.46	98.78
4	97.33	78.28	4.27	78.81	97.59
5	92.27	90.46	1.18	90.26	99.37
6	94.59	63.39	6.54	64.37	96.32
7	93.14	84.08	1.35	84.52	99.28
8	95.37	73.24	1.73	73.51	99.09
9	95.85	78.28	4.27	78.81	97.59
10	93.25	90.01	0.78	91.02	99.56
11	92.55	96.15	0.22	96.56	99.87
12	96.77	48.77	2.6	49.16	98.65
13	96.55	88.31	2.18	88.57	98.77
14	95.22	70.47	1.7	71.05	99.1
15	97.84	73.45	1.35	68.41	98.87
Avg. 723 images	98.50	81.08	1.79	80.81	99.01

Table 6.12 Performance parameters for ROI indicated in ground truth set-2 using KFCM clustering

Image no.	Accuracy	Precision	Error rate	Recall	Specificity
1	95.67	85.05	0.26	95.30	99.79
2	96.12	85.73	1.71	86.60	99.05
3	98.89	67.70	2.34	69.32	98.73
4	97.88	57.71	7.33	60.26	95.76
5	93.4	49.64	4.59	50.87	97.53
6	95.54	78.53	4.33	78.02	97.62
7	94.02	51.68	7.24	46.60	96.47
8	96.47	74.05	1.87	75.74	98.98
9	96.02	63.50	3.30	63.02	98.28
10	94.01	30.23	5.49	31.25	97.07
11	93.65	29.09	6.40	25.60	96.93
12	97.33	82.18	3.78	80.79	97.98
13	97.44	65.55	2.23	62.83	98.91
14	96.45	91.66	1.58	90.21	99.20
15	97.87	89.90	1.34	68.78	98.45
Avg. 723 images	98.97	69.71	2.01	66.64	98.97

The bar chart summarising the evaluation measures of KFCM technique w.r.t. ROI of ground truth set-1 and ROI of ground truth set-2 is shown in Figs. 6.11 and 6.12.

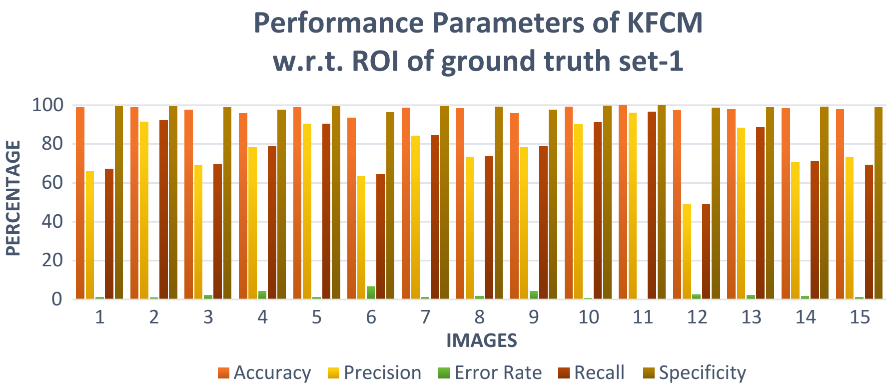

Fig. 6.11 Parametric evaluation measures of KFCM w.r.t. ROI of ground truth set-1

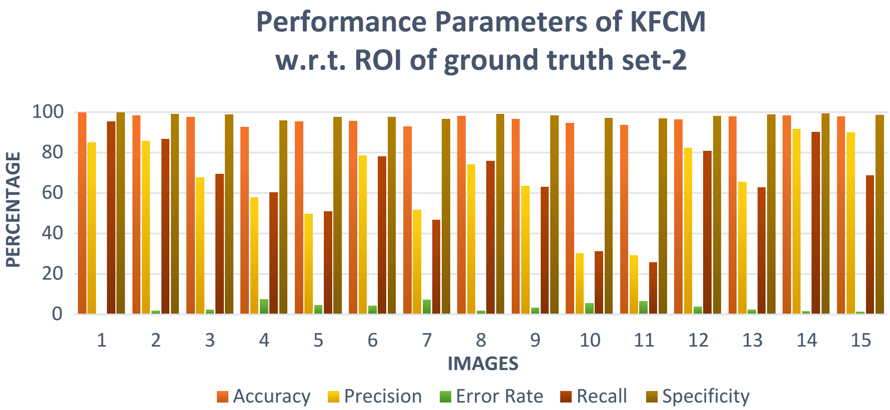

Fig. 6.12 Parametric evaluation measures of KFCM w.r.t. ROI of ground truth set-2

Average accuracy of 723 data base images was found to be 98.50% with precision of 81.08%, error rate of 1.79%, recall of 80.81% and specificity of 99.01% w.r.t. ROI of ground truth set-1. Average accuracy of 723 database images was found to be 98.97% with precision of 69.71%, error rate of 2.01%, recall of 66.64% and specificity of 98.97% w.r.t. ROI of ground truth set-2.

6.4 Discussion and Summary

In this chapter we have evaluated three clustering methods, namely K-Means, Fuzzy C-Means and Kernel based Fuzzy C-Means for dental segmentation of dental radiograph. FCM is used for more than one clustering and KFCM K-Means, FCM and KFCM is used for non-mapping clustering. Moreover, KFCM overcomes the demerit of FCM technique. Validation of segmentation is not the prime requirement for diagnosing the problem in radiograph; rather, the accuracy, precision, recall, error rate, specificity and, most importantly, reduction in computational speed of segmentation, as well as decrease in amount of manual interaction are major parameters to be considered.

Chapter 7
Conclusion and Further Enhancements

7.1 Overall Book Contributions

Through the computational analysis of various dental radiographs the aim of this research work is to develop an add-on approach to help medical practitioners in the pre-diagnosis treatment of various dental diseases. This thesis investigated and demonstrated the use of four categories of methods while performing image analysis of dental radiographs. The study began with the state-of-the-art review of the work done so far in the domain of image analysis, medical image analysis and then focused on dental image processing. The domain study also concentrated on acquiring knowledge of stomatology dentistry, and dental diseases and their diagnostic methods.

Based on the state-of-the-art review the first study was done revolving around the basic image processing techniques for dental radiographs and sorting out the various approaches useful for further identifications and analysis. In this thesis, active contour snakes model was introduced as a semi-automatic approach for the selection of region of interest. The region so detected was quite accurate and approximately similar to the selection being done by medical practitioners manually. The snakes model is not fully automated. It requires selection of input points from the domain expert to produce a final converged region.

Moreover, with more than one decay present in the dental radiograph the method was not found as efficient as expected in that case. The probability of false detection also increased in such cases which could lead to incorrect identification.

The method of multiphase level set approach as an automatic approach for diagnosis and detection of the affected tooth decay. The results of this method were found satisfactory when it was applied to various disease-affected dental radiographs.

The accuracy with this method was found to be above 95% in almost different cases (diseases).

K. R. Jain, N. C. Chauhan, *Dental Image Analysis for Disease Diagnosis*,
https://doi.org/10.1007/978-3-030-14136-3_7

Table 7.1 Summary of proposed method and respective problem solution

Methods proposed and investigated	Type of dental diseases present in radiographs used
Approach 1 Segmentation of ROI in radiographs using Morphological operations	Idiopathic resorption; abscess; cyst; endodontic treatment or filling
Approach 2 Parametric model of active contour (snakes model) for identification of ROI from dental radiographs	Erythroplakia; leucoplakia; idiopathic resorption; abscess; cyst; dental implants
Approach 3 Geometric model of active contour (multiphase level set approach) for analysis of dental radiographs	Idiopathic resorption; abscess; cyst; dental implants; endodontic treatment or filling; impacted 3rd molar
Approach 4 Investigation of clustering techniques for segmentation and analysis of dental radiographs	Idiopathic resorption; abscess; cyst; dental implants; endodontic treatment or filling; impacted 3rd molar

Our final proposal was to investigate the role of computational machine learning-based clustering techniques for the segmentation and analysis of decayed region in dental radiographs. Two popular clustering methods, namely K-means and fuzzy C -means were investigated and results were compared with the ground truth. Finally, a kernel-based fuzzy C-means method was investigated and found to be better and robust compared to earlier two clustering methods on radiographs having different diseases.

Table 7.1 summarises our all proposed approaches and their application to dental radiographs having different types of dental diseases. A total of 967 radiographs were obtained from two medical practitioners along with their ground truth information (i.e. marking of ROI) and used in the thesis as image dataset for analysis and investigations. Our results obtained by application of various proposed methods are validated using five evaluation parameters, namely accuracy, precision, error rate, recall and specificity. Sample results on few dental radiographs are presented in each chapter, while overall results are summarised using evaluation parameters in tabular fashion.

7.2 Comparison Among the Proposed Methods and Conducting Remarks

Dental features remain more or less invariant over time. Most of the research is focused in the area of forensic science. This doctoral thesis carries out four processes for the identification of region of interest from a dental radiograph revolving around the dental image processing. The study begins with basic image processing techniques used to identify dental caries affected region. We have used horizontal and vertical ROI to decide whether the caries-affected tooth is applicable for dental treatment like RCT or filling. However, the results were quite clear but had many pitfalls. The whole process was manual in nature. The grey level threshold used for clipping varied for different images. Moreover, the cropping being done to extract the tooth was manual in nature and later comparison with the ground tooth to finalise under which case the cyst fall was also manual. A total of 484 database images were being identified successfully affected from caries.

While the process of further investigation continued, we came across one more problem of oral mucosa among dental radiographs. Symptoms among patients are pain, sores, swelling, changes in taste, unusual colours, and changes in the texture of tongue [39]. Many of these issues are not serious and are caused by minor infections or mouth injuries. We observed that the tongue image segmentation would play a crucial role in identification and diagnostic process to practitioners. As per the discussion with practitioners, the samples are sent to pathological labs for testing and further diagnosis. The most common precancerous critical diseases in oral mucosa are leucoplakia and Erthyroplakia. We found that even the suggested method was quite useful for our dental problems too. A total of 177 erythroplakia-based red patches and 67 leucoplakia-based white patches on tongue were correctly identified by the proposed snakes model. A total of 372 cases of RVG file format-based dental images are also identified correctly. Here, in suggested approach we took the points directly so it can automatically extract affected part. We also implemented a Graphical User Interface (GUI) in MATLAB. In this GUI, we added some features like calculation of area affected regions and applying use of canny operator. Based on interaction with practitioners this user-friendly approach was found quite satisfactory in providing a broad idea to practitioners for a precancerous treatment. According to practitioner's perception, the GUI-based tool results can help practitioners better in explaining information/identification to patients.

An automated segmentation method based on level set approach for segmenting region of interest from a dental radiographic image is presented after active contour modelling. Based on the evaluation measures, the proposed method is found to be quite effective in identification of interested region. The proposed method can be useful for assistance to the dental medical practitioners during their endodontic treatment of the tooth. The method can further be evaluated rigorously and can also be integrated in any computer-based diagnostic tool. A total of 723 cases of RVG file format-based dental images were processed. An average accuracy on 723 database images was found to be 97.83% with precision of 79.54%, error rate of 2.16% and specificity of 98.77% w.r.t. ground truth image set-1. Average accuracy on 723 database images was found to be 96.00% with precision of 66.12%, error rate of 3.99% and specificity of 97.82% with respect to second ground truth image set.

Lastly, we have evaluated three clustering methods for dental segmentation. K-means, FCM and KFCM methods on various dental problems being discussed so far. The importance of accuracy and error rate of method is significant in medical application area. Therefore, validation of segmentation is not the prime requirement for diagnosing the problem in patient, rather the accuracy, precision, recall, error rate, specificity and, most importantly, reduction in computational speed of segmentation, as well as decrease in amount of manual interaction are major parameters to be considered.

Based on the evaluation measures the accuracy of three clustering techniques with multiphase level approach (MPLSA), snakes model-based approach (SBA) and morphological operations-based approach (MOBA) were compared and tabulated as shown in Table 7.2. The bar chart of the same is shown in Fig. 7.1.

The motivation for the realisation of this work is exploiting the methods of image processing as well as machine learning in the domain of applied medical sciences. The state-of-the-art review highlighted that there are no significant contributions made for dental disease identification and diagnosis. Hence, the proposed

Table 7.2 Comparison of accuracy among the various proposed approaches

Images	Accuracy KFCM	Accuracy K-means	Accuracy FCM	Accuracy of MPLSA	Accuracy of SBA	Accuracy of MOBA
1	97.1	83.03	99.54	98.12	85.52	81.36
2	95.61	95.83	96.39	95.97	86.26	79.83
3	99.04	98.64	98.39	97.65	83.65	80.61
4	96.11	97.33	96.88	96.21	76.16	75.13
5	91.01	92.27	91.83	98.28	87.67	80.44
6	96.34	94.59	95.62	99.49	85.17	83.38
7	95.24	93.14	94.31	99.9	77.29	74.45
8	93.05	95.37	92.82	92.66	75.08	71.42
9	92.56	95	93.2	95.4	73.23	69.24
10	93.62	93.25	95.46	98.41	83.1	74.5
11	99.04	92.55	99.82	98.81	88.35	73.49
12	92.84	96.77	91.14	99.13	82.14	72.88
13	97.96	96.55	96.44	94.18	81.41	72.74
14	99.75	95.22	93.56	98.87	83.33	79.85
15	97.87	98.13	97.68	97.89	78.67	77.04

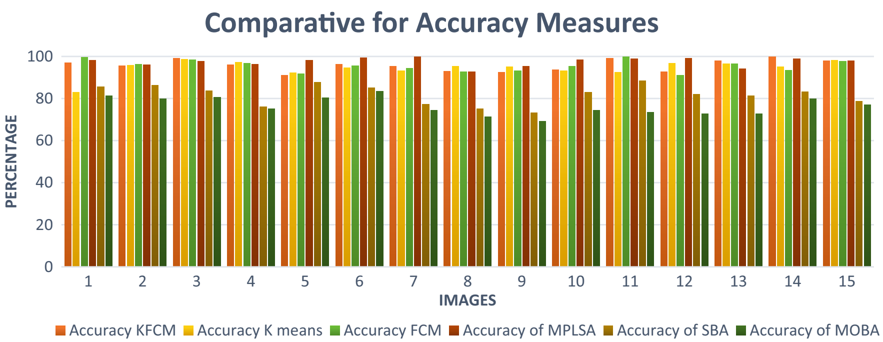

Fig. 7.1 Comparison of accuracy among the various proposed approaches

approaches can serve as an add-on help during their pre-diagnostic and post-diagnostic identification and treatment.

The results of the methods were also validated with the practitioners who shared their dental radiograph images and ground truth information. As per interaction with the practitioners, the results obtained are satisfactory and can provide add-on help during their practices. The certificates obtained from these practitioners are attached in the Appendix (A) of the thesis for reference.

7.3 Further Enhancement

Considering technological developments and automation as presented in the thesis and also based on research contributions from the literature, one of the further plans is to develop a machine learning-based computational system and rigorously validate them with more number of practitioners. The involvement of practitioners during this process can improve the chances of successful development and its support.

Investigation and development of hybrid methods or yet novel methods are possible specifically when multiple diseases are present in the same radiographs. Investigations of computer vision-based techniques along with machine learning methods can also play an important role when multiple radiographs (different orientations, scales, etc.) of same cases (patients) are available.

Each dental tooth of a patient contains individual image properties; hence, one of the further enhancements can be to separate individual tooth, compare it with the ground truth and then again investigate the methods as presented in the book.

Bibliography

1. Ahmad, S. A., Taib, M. N., Khalid, N. E. A., & Taib, H. (2012). An analysis of image enhancement techniques for dental X-ray image interpretation. *International Journal of Machine Learning and Computing, 2*(3), 292–297.
2. Yousefi, B., Hakim, H., Motahir, N., Yousefi, P., & Hosseini, M. M. (2012). Visibility enhancement of digital dental X-ray for RCT application using Bayesian classifier and two times wavelet image fusion. *Journal of American Science, 8*(1), 7–13.
3. White, S. C., & Pharoah, M. J. (2004). *Oral radiology, principles and interpretation*. St. Louis, MO: Mosby.
4. Sakurai, T., & Kawamata, R. (2010). Relationship between radiation dose reduction and image quality change in photostimulable phosphor luminescence X-ray imaging systems. *Dentomaxillofacial Radiology, 39*(4), 207–215.
5. Oprea, S., Marinescu, C., Lita, I., Jurianu, M., Visan, D. A., & Cioc, I. B. (2008). Image processing techniques used for dental x-ray image analysis. In *2008 31st international spring seminar on electronics technology*, pp. 125–129.
6. Rad, A. E., Rahim, M. S. M., Rehman, A., & Saba, T. (2016). Digital dental X-ray database for caries screening. *3D Research, 7*(2), 1–5.
7. Fahmy, G. (2004). Towards an automated dental identirication system (ADIS). *Lecture Notes in Computer Science, 3072*, 789–796.
8. Noujeim, M. (2011). Pre-clinical evaluation of a new dental panoramic radiographic system based on tomosynthesis method. *Dentomaxillofacial Radiology, 40*(1), 42–46.
9. Fahmy, G. (2005). Toward an automated dental identification system. *Journal of Electronic Imaging, 14*(4), 43018.
10. Sakuma, A. (2012). Three-dimensional visualization of composite fillings for dental identification using CT images. *Dentomaxillofacial Radiology, 41*(6), 515–519.
11. Kamburoğlu, K., Kolsuz, E., Murat, S., Yüksel, S., & Özen, T. (2012). Proximal caries detection accuracy using intraoral bitewing radiography, extraoral bitewing radiography and panoramic radiography. *Dentomaxillofacial Radiology, 41*(6), 450–459.
12. Shafer, W., & Levy, B. M. (1983). *A textbook of oral pathology*. Philadelphia, PA: Saunders.
13. Ahmad, S. A., Taib, M. N., Khalid, N. E. A., Ahmad, R., & Taib, H. (2011). Performance of compound enhancement algorithms on dental radiograph images. *World Academy of Science, Engineering and Technology, 50*, 658–663.
14. Michel, S., Kolller, S. M., Ruh, M., & Schwaninger, A. (2007). Do 'image enhancement' functions really enhance X-ray image interpretation? In *Proceedings of the 29th annual cognitive science society*, pp. 1301–1306.

K. R. Jain, N. C. Chauhan, *Dental Image Analysis for Disease Diagnosis*,
https://doi.org/10.1007/978-3-030-14136-3

15. Said, E. H., Nassar, D. E. M., Fahmy, G., & Ammar, H. H. (2006). Teeth segmentation in digitized dental x-ray films using mathematical morphology. *IEEE Transactions on Information Forensics and Security, 1*(2), 178–189.
16. Dighe, S. C., & Shriram, R. (2012). Dental biometrics for human identification based on dental work and image properties in Periapical radiographs. In *IEEE region 10 annual international conference, proceedings/TENCON*.
17. Kiattisin, S., Leelasantitham, A., Chamnongthai, K., & Higuchi, K. (2008). A match of X-ray teeth films using image processing based on special features of teeth. In *Proceedings of the SICE annual conference*, pp. 35–39.
18. Prajapati, D. B., Desai, N. P., & Modi, C. K. (2012). A simple and novel CBIR technique for features extraction using AM dental radiographs. In *Proceedings – International conference on communication systems and network technologies, CSNT 2012*, pp. 198–202.
19. Omanovic, M., & Orchard, J. J. (2008). Image registration-based approach to ranking dental x-ray images for human forensic identification. *Canadian Society of Forensic Science Journal, 41*(3), 125–134.
20. Abdullah, S. L. S., Hambali, H., & Jamil, N. (2012). Segmentation of natural images using an improved thresholding-based technique. *Procedia Engineering, 41*(Iris), 938–944.
21. Nomir, O., & Abdel-Mottaleb, M. (2005). A system for human identification from X-ray dental radiographs. *Pattern Recognition, 38*(8), 1295–1305.
22. Tiwari, R. B., Sant, S., Baba, G., & Yardi, P. A. R. (2006). Dental X-ray image enhancement based on human visual system and local image statistics. In *Proceeding of the international conference of image processing, Computer Vision and Pattern Recognition*, pp. 100–106.
23. Zhai, X. M., Lu, H. D., & Zhang, L. Z. (2009). Application of image segmentation technique in tongue diagnosis. In *Proceedings – 2009 international forum on information technology and applications, IFITA 2009*, vol. 2, pp. 768–771.
24. Zhong, X., Fu, H., Yang, J., & Wang, W. (2009). Automatic segmentation in tongue image by mouth location and active appearance model. In *8th IEEE international symposium on dependable, autonomic and secure computing, DASC 2009*, pp. 413–417.
25. Li, W., Hu, S., Wang, S., & Xu, S. (2009). Towards the objectification of tongue diagnosis: Automatic segmentation of tongue image. In *IECON proceedings (industrial electronics conference)*, pp. 2121–2124.
26. Wang, Y. G., Yang, J., Zhou, Y., & Wang, Y. Z. (2007). Region partition and feature matching based color recognition of tongue image. *Pattern Recognition Letters, 28*(1), 11–19.
27. Abesi, F. (2012). Diagnostic accuracy of digital and conventional radiography in the detection of non-cavitated approximal dental caries. *Iranian Journal of Radiology, 9*(1), 249–254.
28. Ehsani Rad, A., Mohd Rahim, M. S., & Norouzi, A. (2013). Digital dental X-ray image segmentation and feature extraction. *TELKOMNIKA Indonesian Journal of Electrical Engineering, 11*(6), 3109–3114.
29. Huang, P. W., Lin, P. L., Kuo, C. H., & Cho, Y. S. (2012). An effective tooth isolation method for bitewing dental X-ray images. In *Proceedings – International conference on machine learning and cybernetics*, vol. 5, pp. 1814–1820.
30. Nomir, O., & Abdel-Mottaleb, M. (2008). Hierarchical contour matching for dental X-ray radiographs. *Pattern Recognition, 41*(1), 130–138.
31. Lira, P. H. M., Giraldi, G. A., & Neves, L. A. P. (2013) .Using the mathematical morphology and shape matching for automatic data extraction in dental X-ray images. In *IX Workshop de Visão Computacional*, p. 6.
32. Alsmadi, M. K. (2018). A hybrid fuzzy C-means and neutrosophic for jaw lesions segmentation. *Ain Shams Engineering Journal, 9*(4), 697–706.
33. Tuan, T. M., Ngan, T. T., & Son, L. H. (2016). A novel semi-supervised fuzzy clustering method based on interactive fuzzy satisficing for dental x-ray image segmentation. *Applied Intelligence, 45*(2), 402–428.
34. Otsu, N. (1979). A threshold selection method from gray-level histograms. *IEEE Transactions on Systems, Man, and Cybernetics, 9*(1), 62–66.

35. Farnell, D. J. J., Popat, H., & Richmond, S. (2016). Multilevel principal component analysis (mPCA) in shape analysis: A feasibility study in medical and dental imaging. *Computer Methods and Programs in Biomedicine, 129*, 149–159.
36. Khan, W. (2014). Image segmentation techniques: A survey. *Journal of Image and Graphics, 1* (4), 166–170.
37. Sezgin, M., & Sankur, B. (2004). Survey over image thresholding techniques and quantitative performance evaluation. *Journal of Electronic Imaging, 13*(1), 146–165.
38. Wang, Y., Shen, H., Liang, Y., Lu, X., & Ling, Z. (2015). Adaptive extended piecewise histogram equalisation for dark image enhancement. *IET Image Processing, 9*(11), 1012–1019.
39. Harandi, A. A., & Pourghassem, H. (2011). A semi automatic algorithm based on morphology features for measuring of root canal length. In *2011 IEEE 3rd international conference on communication software and networks, ICCSN 2011*, pp. 260–264.
40. Harandi, A. A., Pourghassem, H., & Mahmoodian, H. (2011). Upper and lower jaw segmentation in dental X-ray image using modified active contour. In *2011 international conference on intelligent computation and bio-medical instrumentation*, pp. 124–127.
41. Bai, X., & Zhou, F. (2013). A unified form of multi-scale top-hat transform based algorithms for image processing. *Optik (Stuttg), 124*(13), 1614–1619.
42. Zhu, R., & Wang, Y. (2012). Application of improved median filter on image processing. *Journal of Computers, 7*(4), 838–841.
43. Jiawei, H., Kamber, M., Han, J., Kamber, M., & Pei, J. (2012). *Data mining: Concepts and techniques*. Waltham, MA: Morgan Kaufmann.
44. Haralick, R. M., & Shapiro, L. G. (1985). Image segmentation techniques. *Computer Vision, Graphics, and Image Processing, 29*(1), 100–132.
45. Arbeláez, P., Maire, M., Fowlkes, C., & Malik, J. (2011). Contour detection and hierarchical image segmentation. *IEEE Transactions on Pattern Analysis and Machine Intelligence, 33*(5), 898–916.
46. Batchelor, B. G. (1994). Edge-region-based segmentation of range images. *IEEE Transactions on Pattern Analysis and Machine Intelligence, 16*(3), 314–319.
47. Kaganami, H. G., & Beiji, Z. (2009). Region-based segmentation versus edge detection. In *IIH-MSP 2009 – 2009 5th international conference on intelligent information hiding and multimedia signal processing*, pp. 1217–1221.
48. Muthukrishnan, R., & Radha, M. (2011). Edge detection techniques for image segmentation. *International Journal of Computer Science, 3*(6), 259–267.
49. Kass, M., Witkin, A., & Terzopoulos, D. (1987). Snakes: Active contour models. *International Journal of Computer Vision, 1*, 321–331.
50. Xu, J., Chutatape, O., & Chew, P. (2007). Automated optic disk boundary detection by modified active contour model. *IEEE Transactions on Biomedical Engineering, 54*(3), 473–482.
51. Bresson, X., Esedoglu, S., Vandergheynst, P., Thiran, J. P., & Osher, S. (2007). Fast global minimization of the active contour/snake model. *Journal of Mathematical Imaging and Vision, 28*(2), 151–167.
52. Derraz, F., Beladgham, M., & Khelif, M. (2004, May). Application of active contour models in medical image segmentation. In *International conference on information technology: Coding and computing, 2004. Proceedings. ITCC 2004*, vol. 2, pp. 675–681.
53. Papandreou, G., & Maragos, P. (2007). Multigrid geometric active contour models. *IEEE Transactions on Image Processing, 16*(1), 229–240.
54. Fischer, B., & Modersitzki, J. (2003). Curvature based image registration. *Journal of Mathematical Imaging and Vision, 18*(1), 81–85.
55. Yezzi, A., Kichenassamy, S., Kumar, A., Olver, P., & Tannenbaum, A. (1997). A geometric snake model for segmentation of medical imagery. *IEEE Transactions on Medical Imaging, 16* (2), 199–209.

56. Wang, G., & Wang, D. (2010). Segmentation of brain MRI image with GVF Snake model. In *Proceedings – 2010 1st international conference on pervasive computing, signal processing and applications, PCSPA 2010*, pp. 711–714.
57. Gonzalez, R. C., Woods, R. E., & Eddins, S. L. (2004). Digital image processing using Matlab – Gonzalez Woods & Eddins.pdf. *Education, 624*(2), 609.
58. Tejaswi, P., & Subhani, S. K. M. (2014). A region based variational method for image segmentation and bias correction with application to MRI. *International Journal of Scientific Engineering and Research, 2*(9), 40–46.
59. Terzopoulos, D., & Fleischer, K. (1988). Deformable models. *The Visual Computer, 4*, 306–331.
60. Zhang, K., Zhang, L., Song, H., & Zhou, W. (2010). Active contours with selective local or global segmentation: A new formulation and level set method. *Image and Vision Computing, 28* (4), 668–676.
61. Osher, S., & Sethian, J. A. (1988). Fronts propagating with curvature-dependent speed: Algorithms based on Hamilton-Jacobi formulations. *Journal of Computational Physics, 79* (1), 12–49.
62. Chen, S., & Radke, R. J. (2009) Level set segmentation with both shape and intensity priors. In *Proceedings of the IEEE international conference on computer vision*, pp. 763–770.
63. Cootes, T. F., Hill, A., Taylor, C. J., & Haslam, J. (1994). Use of active shape models for locating structures in medical images. *Image and Vision Computing, 12*(6), 355–365.
64. Yushkevich, P., Piven, J., Cody, H., & Ho, S. (2006). User-guided level set segmentation of anatomical structures with ITK-SNAP. *NeuroImage, 31*(3), 1116–1128.
65. Pock, T., Cremers, D., Bischof, H., & Chambolle, A. (2009). An algorithm for minimizing the Mumford-Shah functional. In *Proceedings of the IEEE international conference on computer vision*, pp. 1133–1140.
66. Vese, L. A., & Chan, T. F. (2002). A multiphase level set framework for image segmentation using the Mumford and Shah model. *International Journal of Computer Vision, 50*(3), 271–293.
67. Li, B. N., Chui, C. K., Chang, S., & Ong, S. H. (2011). Integrating spatial fuzzy clustering with level set methods for automated medical image segmentation. *Computers in Biology and Medicine, 41*(1), 1–10.
68. Jomier, J., Rault, E., & Aylward, S. R. (2004). Automatic Quantification of Pupil Dilation Under Stress. *International Symposium on Biomedical Imaging (ISBI)*, 249–252.
69. Zhan, T., Zhang, J., Xiao, L., Chen, Y., & Wei, Z. (2013). An improved variational level set method for MR image segmentation and bias field correction. *Magnetic Resonance Imaging, 31* (3), 439–447.
70. Qian Zhao, Y., Hong Wang, X., Fang Wang, X., & Shih, F. Y. (2014). Retinal vessels segmentation based on level set and region growing. *Pattern Recognition, 47*(7), 2437–2446.
71. Naz, S., Majeed, H., & Irshad, H. (2010). Image segmentation using fuzzy clustering: A survey. In *2010 6th international conference on emerging technologies*, no. February 2016, pp. 181–186.
72. Son, L. H., & Tuan, T. M. (2016). A cooperative semi-supervised fuzzy clustering framework for dental X-ray image segmentation. *Expert Systems with Applications, 46*, 380–393.
73. Senthilkumaran, N., & Rajesh, R. (2009). Image segmentation – A survey of soft computing approaches. In *ARTCom 2009 – International conference on advances in recent technologies in communication and computing*, pp. 844–846.
74. Huang, G.-B., Ding, X., & Zhou, H. (2010). Optimization method based extreme learning machine for classification. *Neurocomputing, 74*(1–3), 155–163.
75. Jain, A. K., & Chen, H. (2004). Matching of dental X-ray images for human identification. *Pattern Recognition, 37*(7), 1519–1532.
76. Patel, P. M., Shah, B. N., & Shah, V. (2013). Image segmentation using K-mean clustering for finding tumor in medical application. *International Journal of Computer Trends and Technology, 4*, 1239–1242.

77. Dhanachandra, N., Manglem, K., & Chanu, Y. J. (2015). Image segmentation using K-means clustering algorithm and subtractive clustering algorithm. *Procedia Computer Science, 54*, 764–771.
78. Ahmed, M. N., Yamany, S. M., Mohamed, N., Farag, A. A., & Moriarty, T. (2002). A modified fuzzy C-means algorithm for bias field estimation and segmentation of MRI data. *IEEE Transactions on Medical Imaging, 21*(3), 193–199.
79. Gong, M., Liang, Y., Shi, J., Ma, W., & Ma, J. (2013). Fuzzy C-means clustering with local information and kernel metric for image segmentation. *IEEE Transactions on Image Processing, 22*(2), 573–584.
80. Xiang, D., Tang, T., Hu, C., Li, Y., & Su, Y. (2014). A kernel clustering algorithm with fuzzy factor: Application to SAR image segmentation. *IEEE Geoscience and Remote Sensing Letters, 11*(7), 1290–1294.
81. Chen, L., Chen, C. L. P., & Lu, M. (2011). A multiple-kernel fuzzy C-means algorithm for image segmentation. *IEEE Transactions on Systems, Man, and Cybernetics. Part B, Cybernetics, 41*(5), 1263–1274.

Index

K. R. Jain, N. C. Chauhan, *Dental Image Analysis for Disease Diagnosis*,
https://doi.org/10.1007/978-3-030-14136-3